Graduate School Form 30
Updated 1/15/2015

PURDUE UNIVERSITY
GRADUATE SCHOOL
Thesis/Dissertation Acceptance

This is to certify that the thesis/dissertation prepared

By CAGKAN YILDIZ

Entitled

EFFECT OF GEOMETRIC, MATERIAL AND OPERATIONAL PARAMETERS ON THE STEADY-STATE BELT RESPONSE FOR FLAT BELT-DRIVES

For the degree of Master of Science in Mechanical Engineering

Is approved by the final examining committee:

TAMER WASFY
Chair

ANDRES TOVAR

HAZIM EL-MOUNAYRI

To the best of my knowledge and as understood by the student in the Thesis/Dissertation Agreement, Publication Delay, and Certification Disclaimer (Graduate School Form 32), this thesis/dissertation adheres to the provisions of Purdue University's "Policy of Integrity in Research" and the use of copyright material.

Approved by Major Professor(s): TAMER WASFY

Approved by: SOHEL ANWAR 4/16/2015

Head of the Departmental Graduate Program Date

EFFECT OF GEOMETRIC, MATERIAL AND OPERATIONAL PARAMETERS ON THE STEADY-STATE BELT RESPONSE FOR FLAT BELT-DRIVES

A Thesis

Submitted to the Faculty

of

Purdue University

by

Cagkan Yildiz

In Partial Fulfillment of the

Requirements for the Degree

of

Master of Science

May 2015

Purdue University

Indianapolis, Indiana

This thesis is dedicated to my family who has sacrificed so much for me, supported me and never stopped believing in me.

ACKNOWLEDGMENTS

I'd like to thank my grandfather Mevlut Yildiz sincerely, may he rest in peace. The vision and the will of a poor shepherd grew up in the mountains of Turkey brought his children and grandchildren to where they are today.

I'd like to express my eternal gratitude to my parents, Yilmaz and Emine, who believed in me, supported me and sacrificed so much for me. Things they have done to be there for me goes above and beyond of what anyone could deserve.

I'm so grateful for my best friend, my true wealth in life, my brother. Without him, I'd be nowhere near where I'm. His undoubted faith in me kept me going, and I will be forever indebted of his brotherhood.

I'd like to thank my uncle Ahmet Yildiz, may he rest in peace. The visions he set in my life has been the pillar and the compass of my ventures.

I'd like to express my deepest gratitude to my committee chair, coach and friend Dr. Tamer Wasfy for his encouragement, guidance, teachings and friendship.

I'd like to thank my committee member Dr. Hazim El-Mounayri for his encouragements not just through this thesis but throughout my educational career in IUPUI. Also, I'd like to thank Dr. Andres Tovar for serving on my thesis committee.

I'd like to thank my friend Tolga Yildiz for being there for me through thick and thin and for keeping me inspired and motivated.

I'm very grateful for my supervisors from my company, Ben Guggenbiller and Sudha Dharmavaram for their sincere support throughout my graduate school.

TABLE OF CONTENTS

Page

LIST OF TABLES

LIST OF FIGURES

Figure Page

Figure Page

Figure Page

Figure Page

Figure Page

Figure Page

ABSTRACT

Yildiz, Cagkan. M.S.M.E., Purdue University, May 2015. Effect of Geometric, Material and Operational Parameters on the Steady-State Belt Response for Flat Belt-Drives. Major Professor: Tamer Wasfy.

This thesis presents a comprehensive study of the effects of material, geometric and operational parameters on flat belt-drives steady-state belt stresses, belt slip, and belt-drive efficiency. The belt stresses include: belt rubber shear, normal, axial and lateral stresses; reinforcements tension force; and tangential and normal belt-pulley contact stresses. Belt slip is measured using the driven over driver pulleys' angular velocity ratio. Each parameter was varied over a range to understand its impact on the steady-state belt-drive response. The material parameters studied are belt axial stiffness and damping, belt bending stiffness and damping, and belt-pulley friction coefficient. The geometric parameters studied are pulley center distance, pulleys diameter ratio, and belt thickness. The operational parameters studied are the driver pulley angular velocity and the driven pulley opposing torque (load).

A high-fidelity flexible multibody dynamics parametric model of a two-pulley belt-drive system was created using a commercial multibody dynamics code. In the model the belt's rubber matrix is represented using three-dimensional brick elements and the belt's reinforcements are represented using one dimensional beam elements at the top surface of the belt. An asperity-based Coulomb friction model is used for the friction forces between the pulley and belt. The pulleys are modeled as rigid bodies with a cylindrical contact surface. The equations of motion are integrated using an explicit solution procedure.

Unlike prior models which use one-dimensional truss or beam elements for the belt, the present model uses a three-dimensional belt model which introduces the effect of

the thickness of the belt rubber matrix (modeled using brick elements). This enables a more accurate prediction of the belt stresses and slip than prior models. This thesis resolves in more details the complex stick-slip friction behavior of a axially flexible belt coupled with the shear effects of a flexible rubber cushion and at the same time shows the effect of the main system parameters on this stick-slip behavior. Some of the important conclusions of the thesis include: (1) the driver pulley has two distinct contact zones - a negative traction zone and a positive traction zone - while only one traction zone is present over the driven pulley; (2) the width of the negative traction zone on the driver pulley increases with the belt-pulley coefficient of friction and decreases with the belt axial stiffness; (3) the maximum belt tension and normal contact stress occur on the driver pulley and increase with the belt thickness, belt axial stiffness, and coefficient of friction. The belt-drive modeling methodology presented in this thesis which enables accurate prediction of the belt stresses and slip can in turn be used to more accurately predict the fatigue life, wear life, and energy efficiency of belt-drives.

1. INTRODUCTION

1.1 Introduction and Motivation

Belt-drives find application in mechanical power transmission at nearly every scale. Belts (including poly-V, V and flat) are typically used to transmit mechanical power from a driving motor to one or more driven shafts in machines such as internal combustion engines (in automotive and power generation applications), printing presses, pumps, compressors, mixers; data tape reels; washing machines; dryers; and garden equipment (including lawnmowers, rototillers and snow blowers). They are also used in material/people transport applications such as conveyor belts and elevators. The belt length can vary from a few centimeters in electronic equipment, to 100 kilometers for some mining conveyor belts. Belts transmit mechanical power from the driver pulley to one or more driven pulleys through frictional contact between the belt and pulleys and as an axial load through the belt. Belt-drives have the following advantages over alternative systems (such as gears and chains):

- Lower cost.
- Nearly maintenance free, since they don't require lubrication.
- Easy installation.
- Tolerance to shocks. They can be used to provide tolerance to sudden high loads. in order to prevent damage to other machine components.
- Large distances and large position tolerances between driver and driven shafts.
- Larger tolerance for lateral translation and rotation misalignments between shafts.

- High immunity to contaminants (such as oil, water and small solid debris).

Belt-drive energy efficiency for practical systems typically ranges from 85 to 96%. The efficiency is reduced as the belt ages due to belt elongation (which reduces the belt tension) and reduction of the belt friction as the belt wears. Also, the efficiency is reduced if the belt is either under-tensioned or over-tensioned or in general if the belt-drive is not properly designed. This means that, if belt-drive mechanics/dynamics is better understood such that we can reach an optimum belt-drive design, there is a potential of reducing energy usage. Within the life-time of a machine, belts need to be replaced generally between 5 to 10 times. Better understanding of the factors that lead to belt failure is needed in order to increase belt life and reduce losses due to belt failures. A belt failure almost always causes financial losses and can also result in loss of life. For example, If the serpentine belt in a car or truck breaks or grossly slips, the vehicle will loose power steering, engine cooling and possibly power braking. In manufacturing machines, excessive slip of a worn belt can cause the belt to heat up and ignite causing a fire. In addition, belt breakage or excessive slip can cause product scrapping and manufacturing downtime.

For most belts, the belt cross-section mainly consists of stiff steel, polyester, aramid or kevlar cords along the length of the belt and a rubber (elastomer) matrix in which the cords are embedded (Figure 1.1). The rubber matrix provides the friction interface between the belt and the pulleys through which tangential friction forces are transmitted. The cords reinforce the belt in the axial direction and carry the axial load. The thin cords have high axial stiffness but low bending stiffness, this allows the belt to bend easily around small pulleys, thus reducing belt energy losses, and increasing the belt's fatigue life. Other reinforcing layers are typically used in the cross-section of a belt to increase the bending rigidity along the width of the belt. For special applications other types of belt materials are used. For example, steel conveyor belts are used in automotive test rigs (to simulate a moving road) and in mining, food and chemical industries.

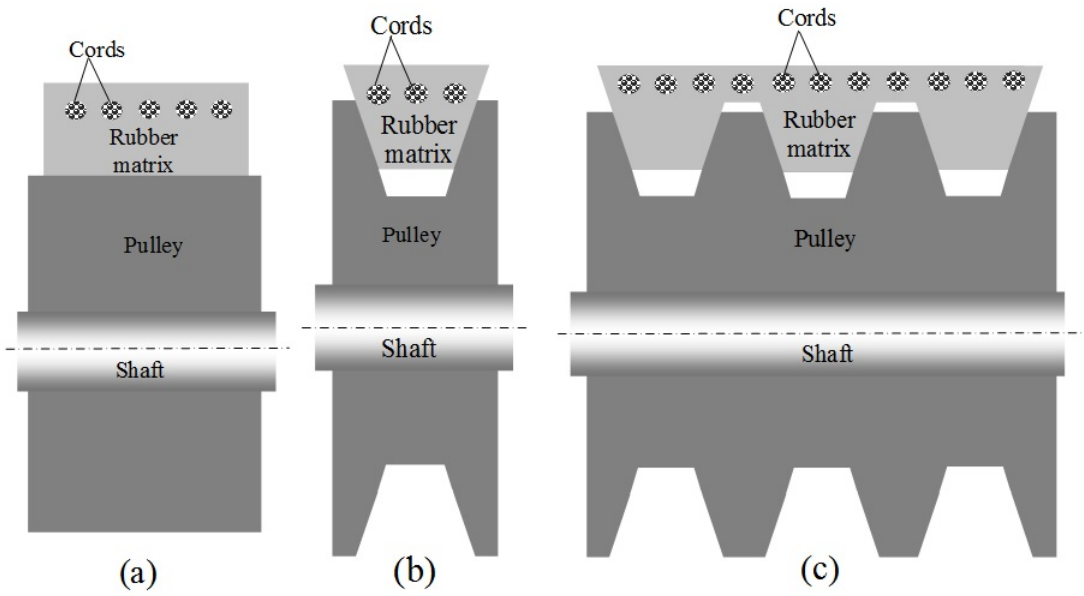

Fig. 1.1. Typical cross-section of (a) flat, (b) V and (c) poly-V ribbed belts.

The Flat belt was the first type of belt to be used in industry. Flat belts have a lower maximum allowable transmitted power than alternative mechanical power transmission systems such as gears and chains. There are three ways to increase the power transmission capacity of a flat belt: increase the belt width, increase the belt tension; or increase the friction coefficient between the belt and the pulleys. The V-belt (Figure 1.1b) was introduced to enable transmitting higher power than a flat belt of the same width and tension because the wedge action between the belt's V-rib and the pulley's groove increases the effective coefficient of friction. However, the V-belt power transmission capacity cannot be increased by increasing the belt width (as in a flat belt) because the wedge angle will change. In order to increase the power transmission capacity of V-belts, multiple belts are installed on the same pulley to share load. The evolution of this concept led to the development of poly-V ribbed belts (Figure 1.1c) which integrate the features of both wide flat belts and V-belts. However, due to the V profile, the thickness of both V and poly-V belts is usually

much larger than that of flat belts. This means that they also have higher bending stiffness and damping than flat belts and therefore are generally less energy efficient than flat belts.

A belt is subjected to a number of cyclic stresses which add a high degree of complexity to the job of a design engineer:

- Axial stress due to tension variations in the belt as its tension transitions from a larger to a smaller tension from the driver pulley to the driven pulleys. The belt tension is carried mainly by the cords.
- Normal contact stress between the belt rubber and the pulleys.
- Shear stress in the belt rubber matrix occurs due to tangential friction on the bottom of the belt and tangential force in the cords.
- Bending stress occurs in the belt's rubber matrix and cords as the belt conforms to the pulleys and then straightens out in the spans. Bending stress is translated into axial stress.

Those cyclic stresses cause the belt rubber and cords to fatigue which can eventually lead to breakage of the belt. The belt is also subjected to sliding wear as the belt creeps against the pulleys during tension transitions. This wear can have a detrimental effect on the belt's friction characteristics as the belt's surface deteriorates, and can lead to gross slip and noisy operation. The belt is also subjected to various steady-state harmonic as well as transient excitations from the drive motor and driven loads. Steady-state harmonic excitations can increase belt wear and fatigue while large transient excitations can lead to gross slip and increased belt wear. The belt-drive is also subjected to vibrations from the drive motor/engine, the driven loads and the supporting structure.

The main motivation of this thesis is to study the effects of the main belt-drive material, geometric and operating parameters on the steady-state belt stresses and

belt slip using a three-dimensional belt model which introduces the effect of the thickness of the belt rubber matrix (modeled using brick elements). Accurate prediction of the belt stresses and creep/slip over the pulleys under various belt-drive operating conditions, can be used to predict and improve the following belt durability and performance measures:

- Belt rubber fatigue life. As mentioned above, the belt rubber can fail due to fatigue loading from the combined cyclic axial, normal, bending and shear stresses. Belt rubber fatigue failure is exhibited as cracks in the rubber matrix. The cracks eventually reach the cords and cause separation between the rubber matrix and the cords. Once full separation occurs the belt can catastrophically break under normal loading conditions since the matrix can no longer hold the reinforcements together. If the rubber material behavior under fatigue loading and the cyclic belt stresses are known, we can calculate the belt rubber fatigue life for a given belt-drive design and then optimize the belt-drive for maximum fatigue life.

- Belt rubber wear life. Excessive belt rubber wear is usually exhibited as excessive belt slip and noise under normal operating conditions. This is due to the fact that a worn belt has a lower coefficient of friction than a new belt such that it can no longer carry the normal operating load without slipping. The belt rubber wear at any point on the belt's surface can be calculated as the integral over time of a function of the normal contact stress and the relative speed between the belt and the pulley (belt slip) at that point. If the rubber material wear behavior, the normal belt stresses and belt slip are known, we can calculate the belt rubber wear life for a given belt-drive design and then optimize the belt-drive for maximum wear life.

- Belt cords fatigue life. The belt cords can fail due to fatigue loading from cyclic axial and bending stresses. Belt cord fatigue failure is exhibited as catastrophic belt breakage under normal operating conditions.

- Energy efficiency. A disadvantage of belt-dives over gears and chains is the fact that they have lower energy efficiency. Typically the mechanical power transmission efficiency of a belt-drive ranges between 85 to 95% compared to gears, lubricated chains and timing-belts which have a typical efficiency range of 95 to 99%. Belt energy losses are converted to heat and noise and are caused by:

  - Bending damping in the rubber and cords as the belt cyclically bends over the pulleys.
  - Friction forces and creep/slip of the belt over the pulleys.
  - Axial damping in the cords and rubber due to belt cyclic stretching.

- Maximum torque capacity. The torque transmitted by a belt-drive is transmitted by the belt as an axial load. Belts are designed to support a maximum axial load. If the axial load is larger than that load, due for example to a large transient load such as sudden deceleration or acceleration of a pulley, then the belt can catastrophically break. Generally the maximum torque that a belt-drive can transmit is much lower than a gear-box or chain-drive of the same size. Increasing belts maximum axial force can lead to the use of belt-drives in applications requiring larger torque capacity. This can lower the operating and maintenance costs in those applications as well as lead to systems which have higher tolerance for position and misalignment errors and harsh environments. Also, belt-drives with higher torque capacity can be used in continuous variable transmission systems to replace gears-boxes with considerable weight, energy efficiency and cost savings.

- Noise. Belt wear can cause the coefficient of friction between the belt and pulleys to be reduced, thus causing belt slip and noise.

- Span vibrations. Belt-span vibrations can be triggered if a harmonic belt excitation frequency is close to a natural frequency of the belt-drive. Excessive

span vibrations can cause high axial, normal and tangential stresses on the belt. In addition, they can cause a belt span to become slack (i.e. have close to zero tension) which may cause the belt to "jump" a pulley.

- Tracking. In some applications where flat belts are used, the belt must remain near the center of the pulley. This is usually achieved by using convex or concave "crowned" pulleys. The tracking performance of belts is important in many belt-drive applications such as elevators.

1.2 Literature Review

1.2.1 Analytical and Computational Belt-Drive Research

Until 1998 there was two different research areas relating to belt-drives: belt-drive mechanics research which considered the mechanics of steady-state belt friction on pulleys, and belt-drive dynamics research which considered vibrations of the pulleys and tensioner. The two research areas had little connection to each other due to the lack of dynamic excitation in the belt-drive mechanics studies, and the lack of true frictional belt-pulley modeling in the belt-drive dynamics studies.

1.2.1.1 Belt-Drive Mechanics Literature

Two of the earliest belt-drive mechanics studies were by Leonard Euler [1] of a belt wrapped around a fixed pulley and Grashof [2] of the frictional mechanics of belt-drives under steady operating conditions. The studies of Euler and Grashof developed the classical belt creep theory, in which a Coulomb law governs the belt-pulley frictional contact, and the belt is treated as a flexible one-dimensional string which adheres to the pulley in an initial adhesion arc, and creeps against the pulley in a subsequent slip arc. Reviews of studies on belt-drive mechanics and belt creep theory are given by Fawcett [3] and Johnson [4]. Belt creep theory was updated with inertial effects by Bechtel et al. [5]. Townsend and Salisbury [6] derived the power loss

expression and the efficiency limit of a belt-drive based on belt creep theory. Leamy and Wasfy [7] used a creep rate dependent law, where the friction force is linearly proportional to the relative tangential velocity, to predict the friction, normal and belt tension distributions over the pulleys. This friction law was shandown to be physically relevant for small sliding velocities [8, 9]. It was shown that, as the slope of the friction law increases, the results approach the belt creep theory results.

Firbank [10] proposed the belt shear theory which considered the mechanics of belt-drives with both Coulomb friction and shear deformation of the rubber. Gerbert [11, 12] included seating unseating and radial compliance effects to the belt shear theory. Alciatore and Traver [13] studied the effect of belt bending stiffness and compared shear and creep theories. Kong and Parker [14] incorporated belt inertia effects in the belt shear theory and compared shear and creep theories friction, normal and belt tension distributions over the pulleys.

1.2.1.2 Belt-Drive Dynamics Literature

Belt dynamics studies considered the rotational response of the pulleys, tensioner motion and/or the transverse response of the axially moving belt due driver motor excitations. The belt-pulley contact was simplified using linear stretching and viscous damping models. Barker [15] studied belt tension resulting from rapid engine acceleration. Hwang et al. [16] studied the periodic rotational response of serpentine belt drives. Beichman et al. [17-19] studied the coupled rotational and transverse response of a three-pulley prototypical serpentine belt drive. Leamy et al. [20, 21] included a Coulomb dry friction damper to the tensioner arm element, and also studied belt-drive's rotational response. Kraver et al. [22] linearized the dry friction in the tensioner arm and developed a complex modal approach to analyze the drive's rotational response.

1.2.1.3 Coupled Belt-Drive Mechanics - Dynamics

Leamy et al. [23, 25] attempted to bridge the gap between belt-drive mechanics and dynamics research by studying simplified dynamic models for small [23] and large [24, 25] rotational speeds. Those studies considered individual pulleys only, and did not calculate the global response of the entire belt drive. Furthermore, the case of medium rotational speeds was not addressed. In Leamy and Wasfy [26, 27] an explicit time integration finite element code was used to model belt-drives. The belt was modeled using truss elements. A penalty formulation was used to model the normal contact constraint between the belt and the pulleys. Friction was modeled using a creep rate dependent friction law, due to its physical relevance [8, 9], its ability to accurately approximate Coulomb friction [7] and its numerically friendliness in the context of explicit time integration. The finite element solution was validated by comparing it to an exact analytical steady-state solution of a two-pulley belt-drive presented in Leamy and Wasfy [7]. The model predictions also agree with the experimental results presented in Pietra and Timpone [28]. This was the first model that bridged the gap between belt mechanics and dynamics. The model could accurately reproduce the steady-state distributions of tangential (friction) and normal contact forces and belt tension over the pulleys and belt slip predicted by the belt creep theory. At the same time it could predict transient rotational motion of the pulleys, belt spans vibrations and tensioner motion [29-35]. In Leamy and Wasfy [29] and Meckstroth et al. [30] the effect of adding one-way clutches and isolator clutches on the belt-drive dynamic response was investigated. In Wasfy and Leamy [31] the effect of the belt bending stiffness was investigated by using beam elements to model the belt instead of truss elements. In Wasfy [30], an asperity-based friction model was developed which consists of the creep rate dependent friction law in parallel with a variable anchor point spring that mimic the behavior of stretching, breaking and reattachment of asperities on the two contact surfaces. The asperity-based friction model can reproduce the belt creep theory results using an explicit time

step that is about 10 times larger than the creep rate dependent law. However, in the studies presented in Refs. [26, 27, 29-35] the effect of shear deformation of the belt rubber was not taken into account. In Kim, Leamy and Ferri [36] an elastic-perfectly plastic friction (EPP) law was used along with an explicit time-integration transient finite element model of a two-pulley belt-drive and one-dimensional truss elements for modeling the belt. The EPP model added a spring in series with the velocity dependent approximate Coulomb friction model developed in [26, 27] in order to account for shear deformation of the rubber. Cepon et al. [37] developed a transient finite element model using beam elements and linear complementarity based Coulomb friction model which also accounts for the belt shear stiffness. In the belt shear theory and in the numerical studies in References [36, 37] one-dimensional truss or beam elements were used to model the belt along with a spring model for the belt shear. In Chen and Shien [38] a steady-state three dimensional finite element model was developed for a two-pulley belt-drive in which truss elements are used to model the belt cords and 8-node Eulerian brick elements are used to model the belt rubber in which the belt material flows through the element. Using that model, the steady-state belt slip and tangential/normal force distribution between the belt and the pulleys for a two-pulley belt-drive were calculated. This model accounts for the belt shear when the belt goes over the pulleys, however due to its steady-state and Eulerian-nature it does not account for the transient stick-slip friction effects.

Wasfy et al. [39] used an explicit time integration finite element code to model the belt using 8-node brick elements for the rubber and 2-node one-dimensional truss elements for the cords at the top of the belt (Figure 1.2). The brick elements add the following effects to the models in References [26, 27, 29-35]: shear deformation of the belt rubber, compression deformation of the belt rubber, and additional belt bending stiffness due to the thickness of the rubber. The model was used to predict the steady-state tangential and normal belt-pulley contact forces and belt-tension for a two-pulley belt-drive. It was also used to predict the average steady-state slip between the belt and the pulleys. However, similar to the models in [26, 27, 29-35],

the model is transient in nature and therefore is capable of predicting those quantities under transient operating conditions. The results in [39] showed that, when the belt thickness is taken into account, there are two distinct traction zones on the driver pulley: a negative traction zone and a positive traction zone, while only one traction zone is present over the driven pulley (Figure 1.3). Those results are different from the results in [36, 37] and the belt shear theory results [10-14] which show only one traction zone for both the driver and driven pulleys (e.g. Figure 1.4). This is most likely due to the following: (1) those are inherently 1-dimensional models so they not account for the 3-dimensional state of stress of the belt; (2) belt bending stiffness due to the rubber layer is not accounted for; (3) and communication of rubber shear and reinforcements tension between pulleys is not accurately modeled. In addition the belt shear theory and the model in [38] are steady-state models so they don't account for the transient stick-slip friction behavior. The results in [39] show that due to the presence of the negative traction zone over the driver pulley, when the belt thickness is taken into account, the maximum belt tension over the driver pulley is 30% higher for the 4 mm thick belt than for the zero-thickness belt (Figure 1.5). This showed that the maximum belt tension could be under-predicted if thin truss, beam or shell element models are used for the belt.

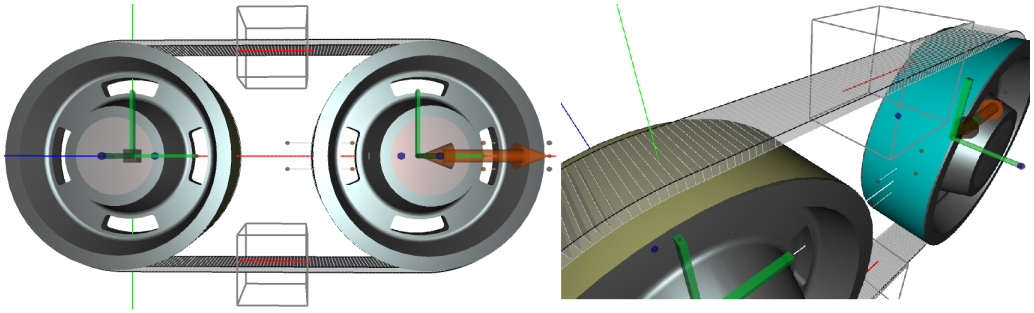

Fig. 1.2. Belt model using in Ref. [39]. Brick elements are used to model the belt rubber and truss elements on the top belt surface (shown as black lines) are used to model the cords.

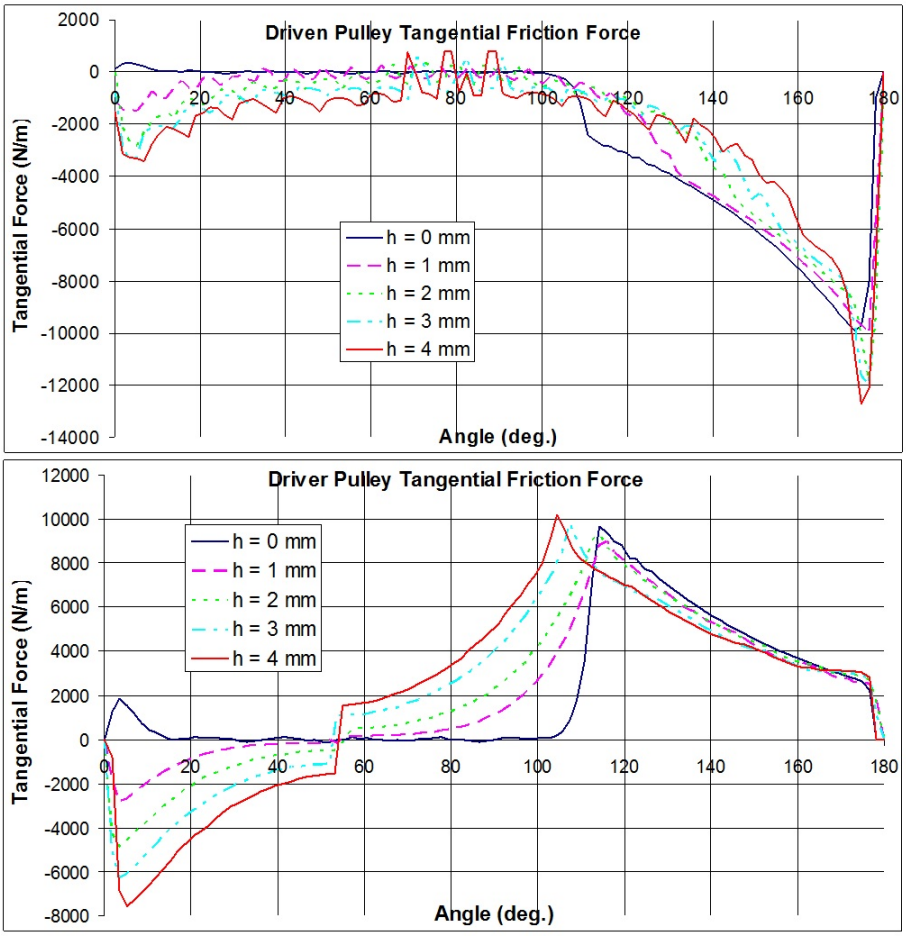

Fig. 1.3. Driver and driven pulleys tangential friction force distributions for belt thicknesses 0, 1, 2, 3 and 4 mm for the two pulley belt-drive model shown in Figure 1.2 in Ref. [39].

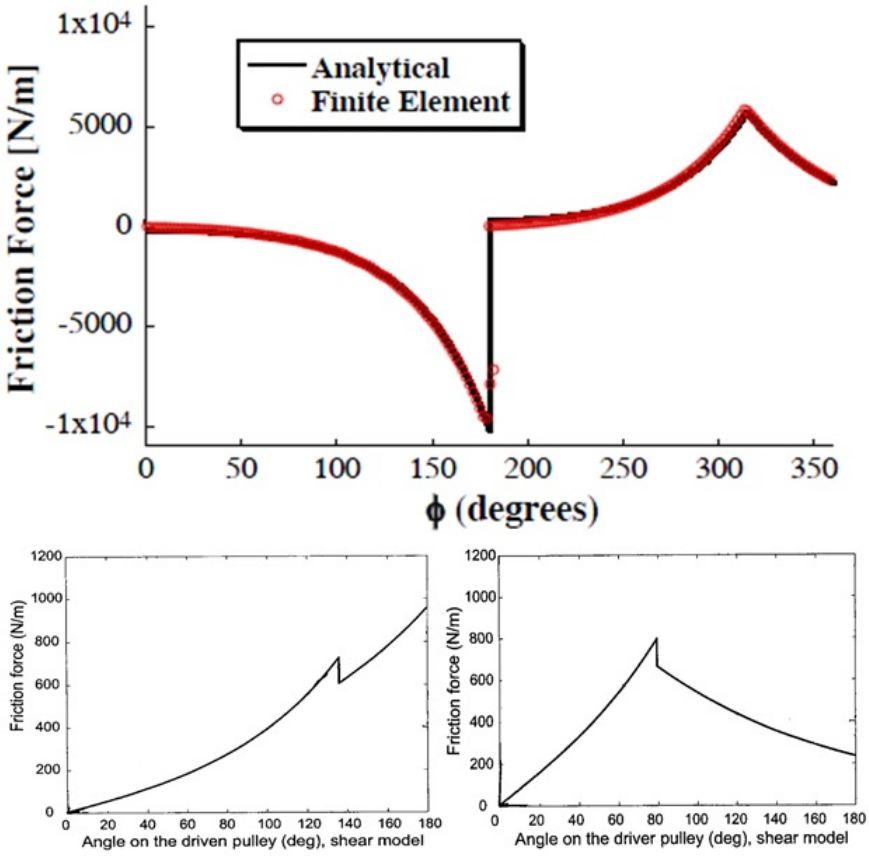

Fig. 1.4. Two pulley belt-drive with a thick belt: (a) Driven (0 to 180) and driver (180 to 360) pulleys tangential friction force distributions in Ref [35] (b) Driven and driver pulleys tangential friction force distributions in Ref [14].

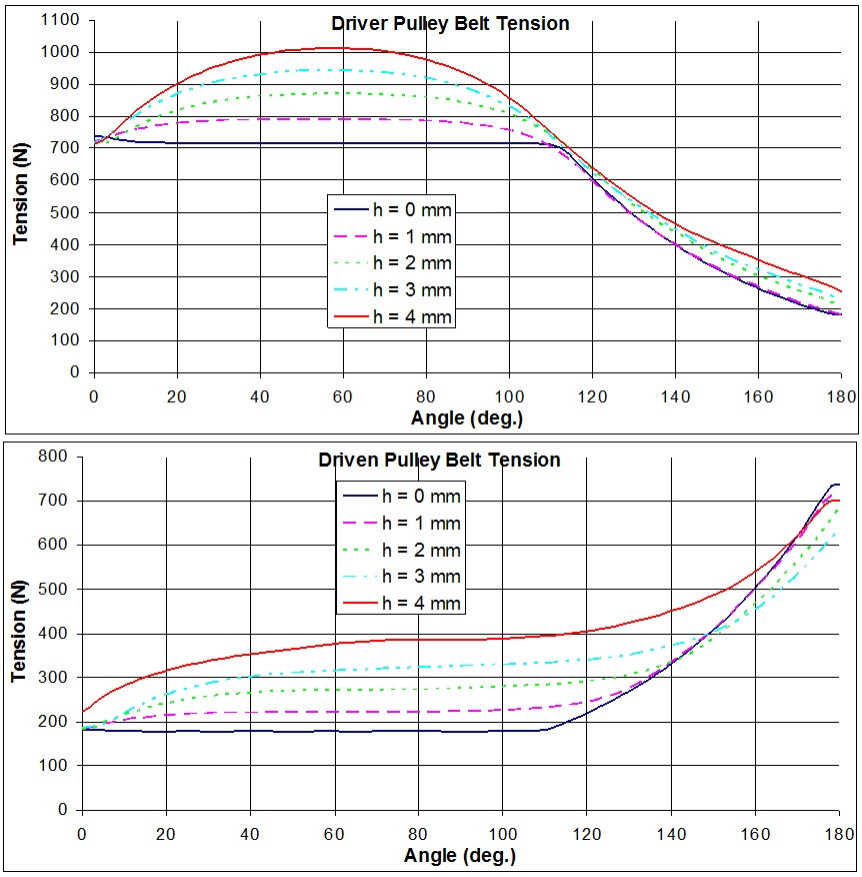

Fig. 1.5. Driver and driven pulleys belt tension distribution for belt thicknesses 0, 1, 2, 3 and 4 mm for the two pulley belt-drive model shown in Figure 2 Ref. [39].

1.2.2 Experimental Belt-Drive Research

There are very few experimental studies on flat, V and poly-V belt-drives. Firbank [40] experimentally measured the total slip (speed loss) between driven and driving pulleys for a two-pulley a 10 mm thick flat belt. Palmer and Jarvis [41] measured the strain in the belt-spans along the surface of a flat belt using a photo-elastic method. A number of studies experimentally measured the tangential and normal belt-pulley contact forces for a two pulley belt-drive using various types of force transducers, including (Firbank [40], Childs [42], Kim et al. [43] and Kim and Marshek [44]). In

those studies the pulleys angular velocities used was less than 20 rpm. In Kim et al. [43] and Kim and Marshek [43] two types of belts are used and the surface of the pulley was modified to mount the force transducers. It was shown that the two belts had different contact force distributions due to the fact they had different construction and friction characteristics. Smith [45] studied thin tape microslip, adhesion and contact normal force over the contact area by capturing an image of the contact area through a transparent pulley using a mirror and a high speed camera.

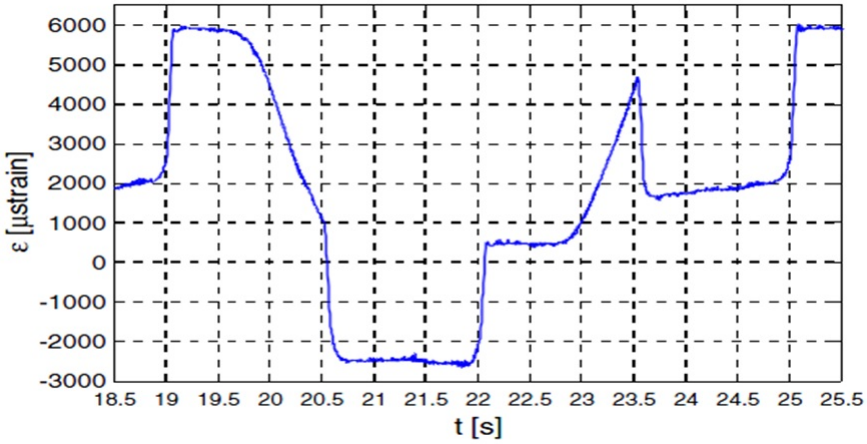

Fig. 1.6. Experimental strain at the top belt surface versus time for a two-pulley belt-drive obtained in Ref. [28].

Recently, Pietra and Timpone [28] measured the belt strain for a two-pulley belt-drive using one strain gage glued to the top surface of the belt. A thin belt (1.35 mm thick) was used. The measured belt strain/tension over the pulleys (Figure 6) agrees well with the belt creep theory and the results of Leamy and Wasfy [26, 27] and the with the 0 mm belt thickness results of Wasfy et al. [39]. This can be seen by comparing Figure 6 and the zero thickness belt results in Figure 5. However, Pietra and Timpone [28] incorrectly assume that the belt strain on the top surface of the belt is directly proportional to the belt tension. This strain rises sharply when the belt bends over the pulleys and drops sharply when the belt straightens out in the belt spans (Figure 6). This strain is not the same as the belt tension, which should

be measured at the neutral axis of the belt cross-section (typically where the cords are located).

1.3 Overview of Belt-Drive Model

The belt-drive model used in this thesis is based on the model presented by Wasfy et al. [39] which extended the finite element model presented in [26, 27, 29-35] to include the effects of the rubber layer on the normal and tangential contact forces and belt tension. The model has the following features:

- The belt rubber matrix is modeled using the 8-node natural-modes brick element developed in Wasfy [46, 47] which is strategically designed to model all the deformation and rigid body modes of a brick element while avoiding locking (including shear, membrane and membrane-warping locking) and spurious modes.

- The belt cords are modeled using 2-node truss elements or 3-node thin beam elements based on the torsional spring formulation presented in Wasfy [48].

- Normal contact constraints are modeled using a penalty technique presented in Leamy and Wasfy [26]. The penalty stiffness and damping parameters can be a function of penetration or penetration speed. This allows the use of an asymmetric penalty damper which prevents the contact surfaces from "sticking" due to damping.

- The penalty technique is also used for modeling joints including spherical, revolute, cylindrical and prismatic joints [49-51].

- Friction is modeled using an asperity-based approximate Coulomb friction model presented in Wasfy [32]. In this model friction is modeled using the creep-rate dependent law used in Leamy and Wasfy [26, 27] in parallel with a variable anchor point spring. The model approximates asperity friction where friction

forces between two rough surfaces in contact arise due to the interaction of the surface asperities.

- Explicit predictor-corrector time-integration solution procedure that uses the trapezoidal integration rule to solve the translational and rotational equations of motion along with joint and contact constraint equations [49-51]. The solution procedure is "embarrassingly" parallel.

- The technique developed by Wasfy [49] is used to model rigid body rotation. In this technique, the rigid bodies' rotational equations of motion are written in a body-fixed frame (thus the inertia tensor is constant). The rotational equations of motion are integrated using the trapezoidal rule to give the incremental rotation angles defined in the body frame. Each time step, the total body rotation matrix with respect to the global reference frame is calculated by multiplying the total body rotation matrix at the previous time step with an incremental rotation matrix corresponding to incremental rotation angles.

- General fast hierarchical bounding box-bounding sphere contact search algorithm for finding the contact penetration between points on master contact surfaces and polygons on slave contact surfaces [50, 51]. The technique can be used to quickly find the contact polygon on a rigid or flexible surface that a finite element node or a point on a rigid body is in contact with. The models described in [29-35, 46-51] are implemented in a commercial explicit time integration finite element code called DIS (Dynamic Interactions Simulator) [52]. This code is used in this thesis to study the effect of the various belt-drive parameters on the steady-state belt stresses, slip and energy efficiency. The DIS code was used in many belt-drive modeling applications including: automotive serpentine belts (Figure 1.7) [29-35, 53], V-belt continuous variable transmission systems (CVTs) (Figure 1.8), elevator belts, conveyor belts (Figure 1.9), and continuous belt-type tracks (Figure 1.10) [51]. In those applications, the belt rubber was modeled using natural-modes brick elements and the cords were

modeled using either truss or thin beam elements. The models were used to predict the following dynamic response quantities: spans-vibrations, belt tension, tensioner motion, friction/normal forces over the pulleys, belt fatigue life, belt wear, belt noise, belt tracking over crowned pulleys and pulley hub loads.

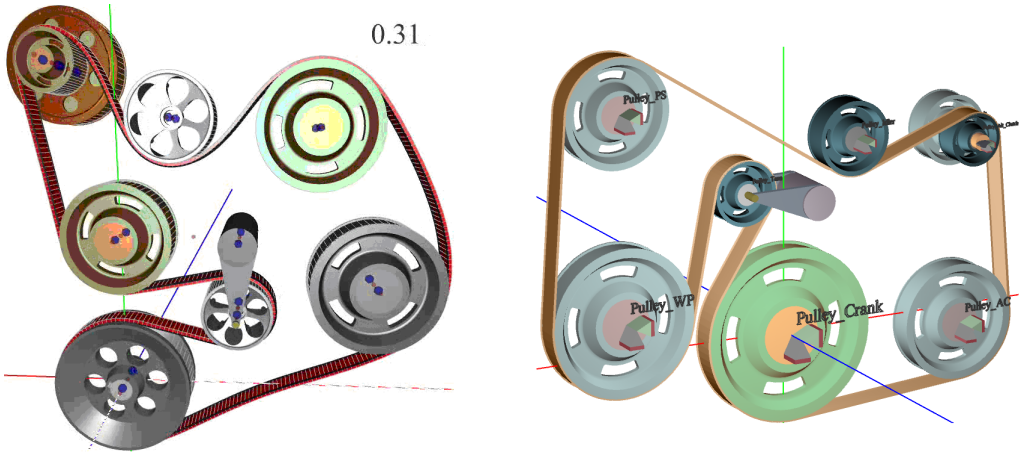

Fig. 1.7. Automotive serpentine belt-drive DIS model [52].

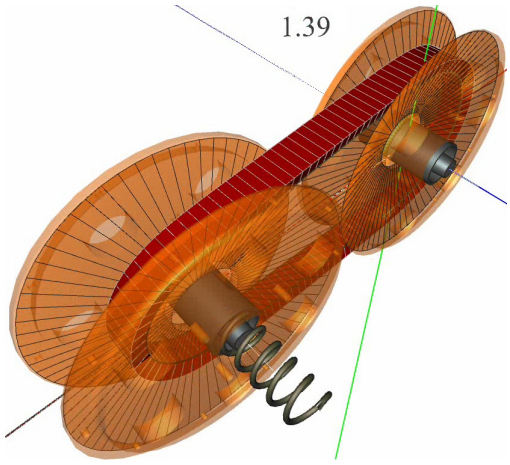

Fig. 1.8. V-belt continuous variable transmission system DIS model [52].

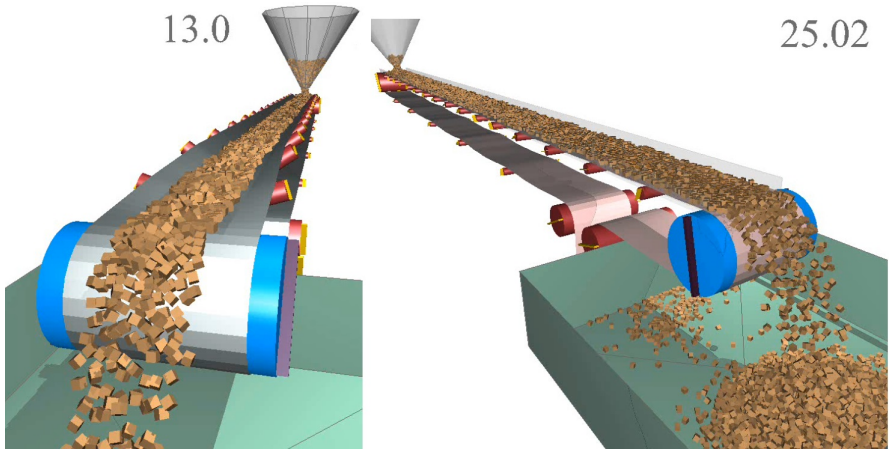

Fig. 1.9. DIS models of troughed (left) and flat (right) mining conveyor belts modeled using shell elements and thin beam elements along the length and width of the belt for modeling the belt cords [52].

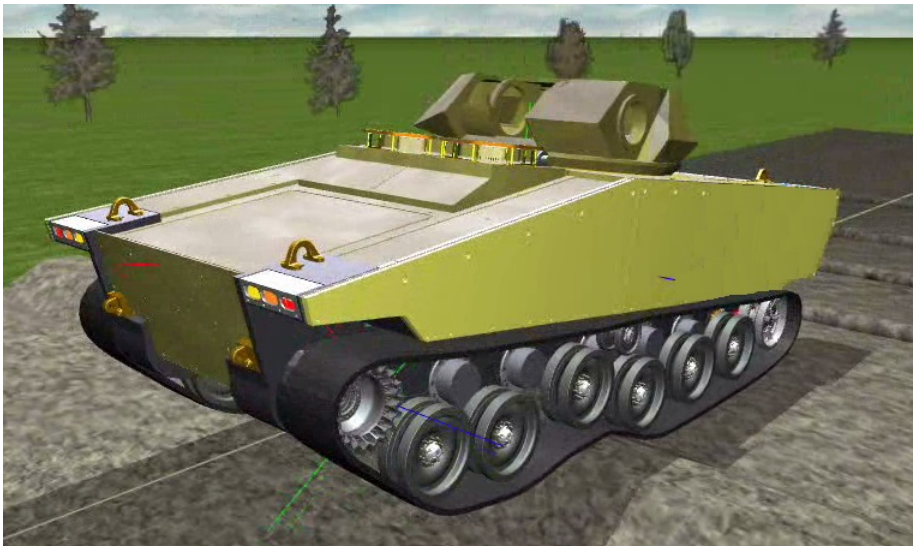

Fig. 1.10. DIS model of a tracked vehicle with a continuous belt-type track [52].

1.4 Objectives

The main objective of this thesis is to present a comprehensive study of the effects of material, geometric and operational parameters on flat belt-drives steady-state belt stresses, belt slip, and belt-drive efficiency using a high-fidelity flexible multibody dynamics parametric model of a two-pulley belt-drive system. The model was created using the DIS multibody dynamics code. In the model the belt's rubber matrix is represented using three-dimensional brick elements and the belt's reinforcements are represented using one dimensional beam elements at the top surface of the belt. An asperity-based Coulomb friction model is used for the friction forces between the pulley and belt. The pulleys are modeled as rigid bodies with a cylindrical contact surface. The equations of motion are integrated using an explicit solution procedure. Unlike prior models which use one-dimensional truss or beam elements for the belt, the present model uses a three-dimensional belt model which introduces the effect of the thickness of the belt rubber matrix (modeled using brick elements). This enables a more accurate prediction of the belt stresses and slip than prior models.

The material parameters studied are belt axial stiffness and damping, belt bending stiffness and damping, and belt-pulley friction coefficient. The geometric parameters studied are pulley center distance, pulleys diameter ratio, and belt thickness. The operational parameters studied are the driver pulley angular velocity and the driven pulley opposing torque (load). Each parameter was varied over a range to understand its impact on the steady-state belt-drive response which includes:

- The belt stresses include: belt rubber shear, normal, axial and lateral stresses; reinforcements tension force; and tangential and normal belt-pulley contact stresses.
- Belt slip measured using the driven over driver pulleys' angular velocity ratio.
- Belt-drive energy efficiency.

1.5 Thesis Contributions

The main contributions of this thesis are:

- Showing the effect of the main belt-drive material, geometric, and operational parameters on the belt-stresses, belt-slip and belt-drive energy efficiency. For the first time in this thesis the belt-stresses including normal and tangential contact and belt rubber stresses are plotted over the pulleys and over the length of the belt. Also, for the first time the effect of the various belt-drive parameters on the belt-slip and belt-drive energy efficiency is studied in details.

- Resolving in more details the complex stick-slip friction behavior of an axially flexible belt coupled with the shear effects of a flexible rubber cushion and the effect of the main system parameters on this stick-slip behavior.

- Reaching important conclusions which can help improve belt fatigue life, wear life and belt-drive energy efficiency (see Chapter 7 for more details). Those include:

  - The driver pulley has two distinct contact zones - a negative traction zone and a positive traction zone - while only one traction zone is present over the driven pulley.

  - The width of the negative traction zone on the driver pulley increases with the belt-pulley coefficient of friction and decreases with the belt axial stiffness.

  - The maximum belt tension and normal contact stress occur on the driver pulley and increase with the belt thickness, belt axial stiffness, and coefficient of friction.

2. MULTIBODY DYNAMICS FORMULATION

2.1 Equations of Motion

The subsequent equations use the following conventions:

- Indicial notation.
- Einstein summation convention for repeated lower case subscript indices, unless otherwise noted.
- Upper case subscript indices denote node numbers.
- Lower case subscript indices denote vector component numbers.
- The superscript denotes time.
- A superposed dot denotes a time derivative.

Two types of finite element nodes are used: point particle nodes and rigid body nodes. Point particle nodes have 3 translational DOFs (Degrees of freedom) while rigid body nodes have 3 translational and 3 rotational DOFS. The algorithm for writing and integrating the equations of motion for spatial rigid bodies using an explicit finite element code was presented in Wasfy [49]. In this algorithm, a rigid body is modeled using a finite element node located at its center of mass. The node has 3 translational DOFs defined with respect to the global inertial reference frame and a rotation matrix defined also with respect to the global inertial frame. The translational equations of motion for the nodes are written with respect to the global inertial reference frame and are obtained by assembling the individual node equations. The equations can be written as:

$$M_K \ddot{x}^t_{Ki} = F\mathrm{s}^t_{Ki} + F\mathrm{a}^t_{Ki} \tag{2.1}$$

where t is time, K is the global node number (no summation over K; $K = 1 \rightarrow N$ where N is the total number of nodes), i is the coordinate number ($i = 1, 2, 3$), MK is the lumped mass of node K, x is the vector of nodal Cartesian coordinates with respect to the global inertial reference frame, and $\ddot{x}$ is the vector of nodal accelerations with respect to the global inertial reference frame, Fs is the vector of internal structural forces, and Fa is the vector of externally applied forces, which include surface forces and body forces.

For each node representing a rigid body, a body-fixed material frame is defined. The origin of the body frame is located at the node that is also the body's center of mass. The mass of the body is concentrated at that node and the inertia of the body is given by the inertia tensor defined with respect to the body frame. The orientation of the body-frame is given by $R^{t_0}_K$ which is the rotation matrix relative to the global inertial frame at time t_0. The rotational equations of motions are written for each node with respect to its' body-fixed material frames as:

$$I_{Kij}\ddot{\Theta}^t_{Kj} = T\mathrm{s}^t_{Ki} + T\mathrm{a}^t_{Ki} - (\dot{\Theta}^t_{Ki} \times (I_{Kij}\dot{\Theta}^t_{Kj}))_{Ki} \tag{2.2}$$

where I_{Kij} is the inertia tensor of rigid body K, $\ddot{\Theta}_{Kj}$ and $\dot{\Theta}_{Kj}$ are the angular acceleration and velocity vectors' components for rigid body K relative to its material frame in direction j ($j = 1, 2, 3$), $T\mathrm{s}_{Ki}$ are the components of the vector of internal torque at node K in direction i, and $T\mathrm{a}_{Ki}$are the components of the vector of applied torque. Since, the rigid body rotational equations of motion are written in a body (material) frame, the inertia tensor I_{Kij} is constant.

The trapezoidal rule along with a predictor-corrector solution method (Section 2.5) is are used for solving Eq. (1) for the global nodal positions x:

$$\min_{a,b,c} \dot{x}^t_{Kj} = \dot{x}^{t-\Delta t}_{Kj} + 0.5\Delta t(\ddot{x}^t_{Kj} + \ddot{x}^{t-\Delta t}_{Kj}) \tag{2.3a}$$

$$x^t_{Kj} = x^{t-\Delta t}_{Kj} + 0.5\Delta t(\dot{x}^t_{Kj} + \dot{x}^{t-\Delta t}_{Kj}) \tag{2.3b}$$

where Δt is the time step. The trapezoidal rule is also used as the time integration formula for the incremental nodal rotation angles $\Delta\Theta_{Kj}$:

$$\dot{\Theta}^t_{Kj} = \dot{\Theta}^{t-\Delta t}_{Kj} + 0.5\Delta t(\ddot{\Theta}^t_{Kj} + \ddot{\Theta}^{t-\Delta t}_{Kj}) \tag{2.4a}$$

$$\Delta\Theta^t_{Kj} = 0.5\Delta t(\dot{\Theta}^t_{Kj} + \dot{\Theta}^{t-\Delta t}_{Kj}) \tag{2.4b}$$

Thus, the rotational equations of motion are integrated to yield the incremental rotation angles. The rotation matrix of body $K(R^t_K)$ is updated using the rotation matrix corresponding to the incremental rotation angles ($R(\Delta\Theta^t_{Ki})$):

$$R^t_K = R^{t-\Delta t}_K R(\Delta\Theta^t_{Ki}) \tag{2.5}$$

The explicit solution procedure used for solving equations (2.1-2.5) along with the constraint equations is presented in Section 2.5. The constraint equations are generally algebraic equations, which describe the position or velocity of some of the nodes. They include: contact/impact constraints (Section 2.3), joint constraints (Section 2.5), and prescribed motion constraints.

2.2 Finite Elements

2.2.1 Truss Element

The truss element connects two nodes. The internal force in a truss element is given by:

$$F = \frac{EA}{l_0}(l - l_0) + \frac{CA}{l_0}i \tag{2.6}$$

where E is the Young's modulus, C is the damping modulus, A is the cross-sectional area, l is the current length of the truss, $I - 0$ is the un-stretched length of the truss.

2.2.2 Torsional Spring Beam Element

The torsional-spring beam element developed in Wasfy [48] is used for modeling the belt reinforcements as thin beams. The element has 3 point mass type nodes (nodes which have only translational DOFs). A beam element is shown in Fig. 2.1a The beam element connects the point p_1 (mid-point of $\overline{12}$) to point p_2 (mid-point of $\overline{23}$). The slope of the beam at p_1 is tangent to $\overline{12}$ and the slope of the beam at p_2 is tangent to $\overline{23}$. The beam element consists of two truss sub-elements ($\overline{p_1 2}$ and $\overline{2p_2}$) and a torsional -spring bending sub-element $\overline{p_1 \hat{2} p_2}$. The internal force in a sub-truss element is given by Eq. (2.7). The internal moment in the bending sub-element is given by:

$$M = \frac{EI}{L_0}\Delta\alpha + \frac{CI}{L_0}\dot{\alpha} \tag{2.7}$$

where I is the cross-sectional effective moment of inertia, L_0 is the total unstretched length of the bending element which is equal to the length of $\overline{p_1 2}$ plus $\overline{2p_2}$, and $\Delta\alpha$ is the change in angle between $\overline{p_1 2}$ and $\overline{2p_2}$ from the unstressed configuration. Figure 1b shows how a beam is discretized using the 3-noded beam element. This thin beam element does not have a torsional response along the axis of the beam. In addition, it assumes that the bending moments of inertia of the cross-section around two perpendicular cross-section axes are the same.

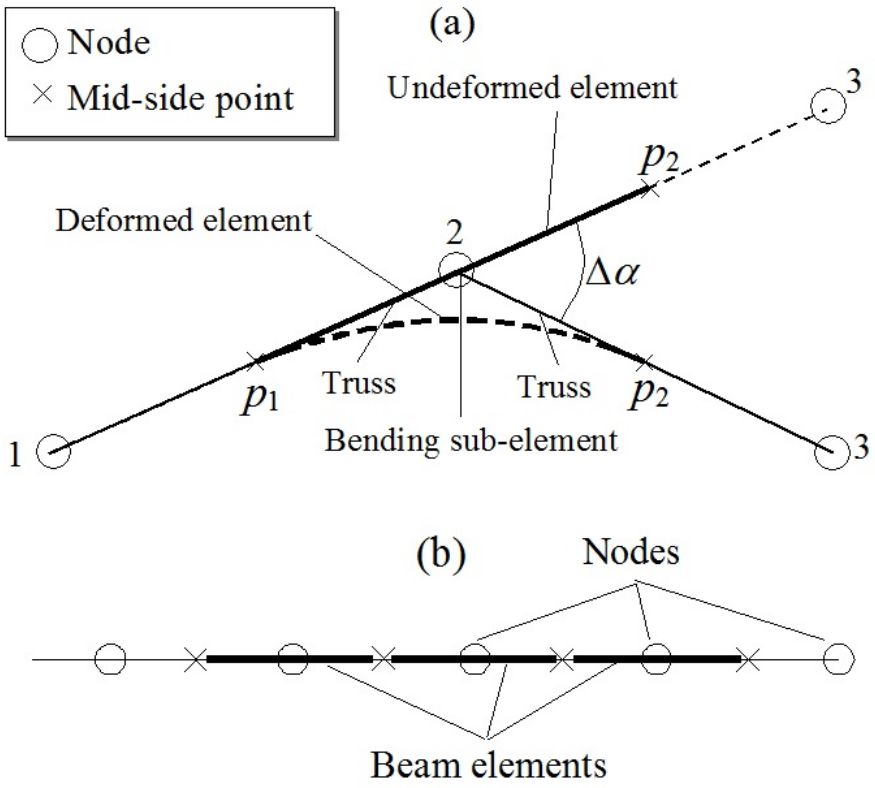

Fig. 2.1. (a) 3-noded beam element [48]; (b) finite element discretization of a beam using the 3-noded beam element.

Similar to the natural-mode brick element presented in the next Section, the torsional-spring beam elements only need edge lengths and angles for evaluation of the element internal forces. Thus, they have nearly zero computational cost when used in conjunction with the natural-mode brick element.

2.2.3 Natural-Modes Brick Element

The 8-node natural-modes brick element presented in Wasfy [46, 47] is strategically designed to model all the deformation and rigid body modes of a brick element (Figure

2.2) while avoiding locking and spurious modes. All the element nodes are point mass type nodes with only translational DOFs.

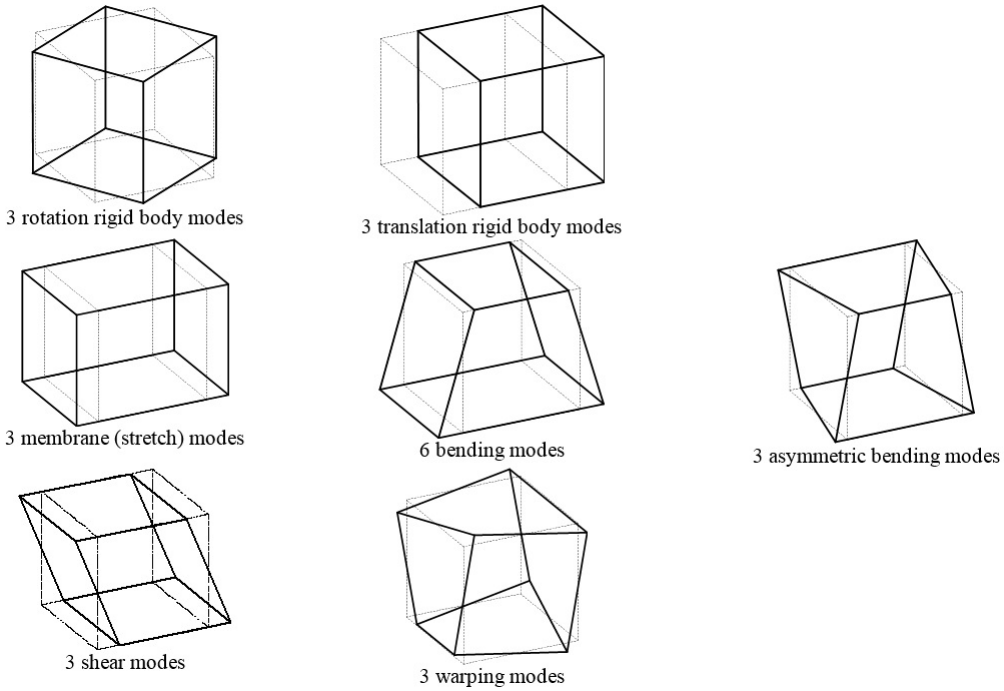

Fig. 2.2. Twenty four rigid body and deformation modes of a spatial 8-node brick element [46].

Two types of sub-elements are used to model the brick: two-node truss element and four-node surface shear element. Twelve truss elements along the twelve edges of the element are used to model the membrane and bending modes of the element. Six surface shear elements are introduced at each of the six element surfaces to model the shear and warping modes of the element (Figure 2.3). The derivations of the stiffness characteristics and structural forces generated by the truss and the surface shear elements are given in [46]. The brick element has the following characteristics:

- All the deformation modes, including, membrane, bending, shear, and warping are accurately modeled. Thus the element does not have any spurious modes.

- The shear stresses are evaluated as the average stresses over each of the element faces, thus the element does not exhibit shear locking.
- All element structural forces are aligned with the element edges, thus the element does not exhibit membrane or membrane-warping locking.

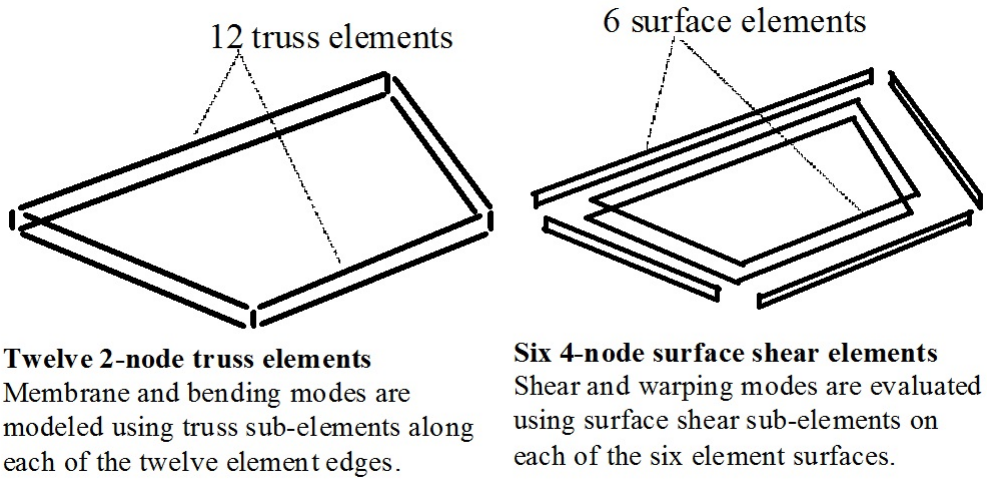

Fig. 2.3. Sub-elements of the 8-node lumped-parameters brick element [46].

The element has the following advantages:

- It accurately models shear and bending with only one element through the belt's thickness.
- The internal element forces require calculation of the length of the 12 element edges and angles between those edges. Those edges and angles are in common between neighboring brick elements, thus they only need to be calculated once for 2 to 4 elements. This, makes the element more computationally efficient that other brick elements.

2.3 Contact Model

The penalty technique is used to impose the normal contact constraints between finite element nodes or points on a rigid body and finite element surfaces or quadrilateral surfaces of rigid bodies Wasfy et al. [50]. The first step is to find the position and velocity of the contact nodes and points. For finite element nodes the global position x_{Gp} and velocity $\dot{x}_{\text{Gp}}$ of a contact node relative to the global inertial frame are readily available:

$$x_{\text{Gp}i} = x_{Ki} \tag{2.8a}$$

$$\dot{x}_{\text{Gp}i} = \dot{x}_{Ki} \tag{2.8b}$$

where x_{Ki} and $\dot{x}_{Ki}$ are the position velocity vectors of contact node K. For rigid bodies the global position x_{Gp} and velocity $\dot{x}_{\text{Gp}}$ of a contact point are given by:

$$x_{\text{Gp}i} = X_{\text{BF}i} + R_{\text{BF}ij} x_{\text{Lp}j} \tag{2.9a}$$

$$\dot{x}_{\text{Gp}i} = \dot{X}_{\text{BF}i} + R_{\text{BF}ij} (\omega_{\text{BF}} \times x_{\text{Lp}})_j \tag{2.9b}$$

where X_{BF} and $\dot{X}_{\text{BF}}$ are the global position and velocity vectors of the rigid body's frame, R_{BF} is the rotation matrix of the rigid body relative to the global reference frame, ω_{BF} is the rigid body's angular velocity vector relative to its local frame, and x_{Lp} is the position of the contact point relative to the rigid body's frame.

The frictional contact force F_{c} at each contact point/node (sum of the normal contact and tangential friction forces) is transferred as a force and a moment to the center of mass of the rigid body (center of the body frame). The negative of this force is transferred to the contact surface element by distributing it to the nodes forming the surface using the element shape function:

$$F_{Ki} = -N_K F_{\text{c}i} \tag{2.10}$$

where N_k are the surface element shape functions at the contact point and F_{Ki} are the contact forces on node K of the surface element. In case the contact body is a rigid body, then this force can also be transferred to the center of mass of the contacting rigid body as a force and moment:

$$F_i = -F_{\mathrm{c}_i} \tag{2.11a}$$

$$T_i = -(x_{\mathrm{Lp}i} \times R_{\mathrm{BF}ji} F_{\mathrm{c}_i}) \tag{2.11b}$$

$$x_{\mathrm{Lp}j} = R_{\mathrm{BF}ji}(x_{\mathrm{Gp}i} - X_{\mathrm{BF}i}) \tag{2.12}$$

where F_i is the contact force at the center of mass of the contact rigid body, T_i in the contact moment on the contact rigid body, x_{Lcp} is the position of the contact point relative to the rigid body's frame and x_{Gcp} is the position of the contact point relative to the global reference farm. Thus, the contact algorithm supports flexible-flexible, rigid-rigid and rigid-flexible body contact.

2.3.1 Penalty Normal Contact Model

The penalty technique is used for imposing the constraints in which a normal reaction force (F_{normal}) is generated when a node penetrates in a contact body whose magnitude is proportional to the penetration distance. In the present formulation, the force is given by Wasfy and O'Kins [51]:

$$F_{\mathrm{normal}} = Ak_p d + A \begin{cases} c_p \dot{d} & \dot{d} \geq 0 \\ s_p c_p \dot{d} & \dot{d} < 0 \end{cases} \tag{2.13}$$

$$\dot{d} = \nu_{\mathrm{n}_i} n_i \tag{2.14}$$

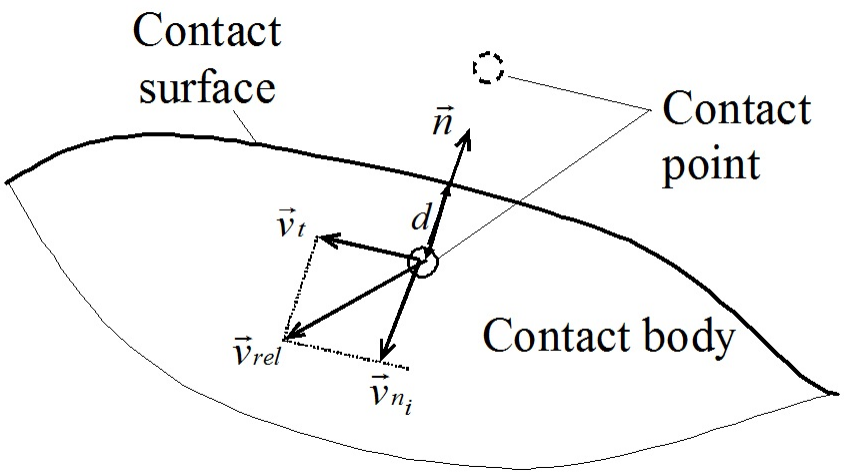

Fig. 2.4. Contact surface and contact node.

where A is the area of the rectangle associated with the contact point, k_p and c_p are the penalty stiffness and damping coefficient per unit area; d is the closest distance between the node and the contact surface (Figure 2.4); $\dot{d}$ is the signed time rate of change of d; s_p is a separation damping factor between 0 and 1 which determines the amount of sticking between the contact node and the contact surface at the node (leaving the body); $\overrightarrow{n}$ is the normal to the surface and $\overrightarrow{v}_{n_i}$ is the velocity vector in the direction of $\overrightarrow{n}$. The normal contact force vector is given by:

$$F_{\mathrm{n}_i} = n_i F_{\mathrm{normal}} \tag{2.15}$$

The total force on the node generated due to the frictional contact between the point and surface is given by:

$$F_{\mathrm{point}_i} = F_{\mathrm{t}_i} + F_{\mathrm{n}_i} \tag{2.16}$$

2.3.2 Asperity Friction Model

The asperity-spring friction model presented in Wasfy [32] is used to model joint and contact friction. In this model friction is modeled using a piece-wise linear velocity-dependent approximate Coulomb friction element in parallel with a variable anchor point spring. The model approximates asperity friction where friction forces between two rough surfaces in contact arise due to the interaction of the surface asperities (Figure 2.5). The tangential friction contact force vector transmitted to the contact body at the contact point (F_{t_i}) is given by:

$$F_{\mathrm{t}_i} = t_i |F_{\mathrm{t}}| \tag{2.17}$$

The asperity friction model is used along with the normal force to calculate the tangential friction force (F_{t}) [32]. When two surfaces are in static (stick) contact, the surface asperities act like tangential springs. When a tangential force is applied, the springs elastically deform and pull the surfaces to their original position. If the tangential force is large enough, the surface asperities yield (i.e. the springs break) allowing sliding to occur between the two surfaces. The breakaway force is proportional to the normal contact pressure. In addition, when the two surfaces are sliding past each other, the asperities provide resistance to the motion that is a function of the sliding velocity and the normal contact pressure. Figure 2.6 shows a schematic diagram of the asperity friction model. It is composed of a simple piece-wise linear velocity-dependent approximate Coulomb friction element in parallel with a variable anchor point spring. Note that in order to connect a node and a rigid body using an asperity spring, the model must keep track of the local position vector of the asperity spring anchor point on the rigid body.

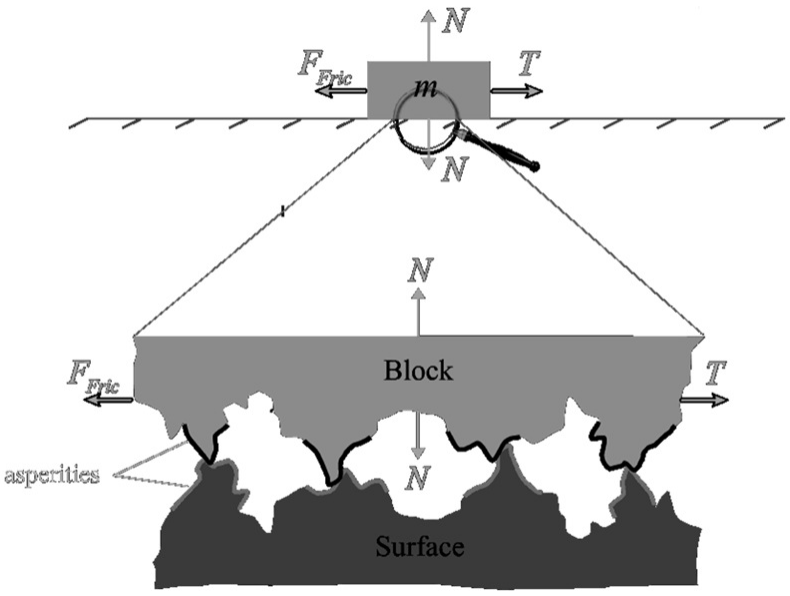

Fig. 2.5. Asperity-based physical interpretation of friction [32].

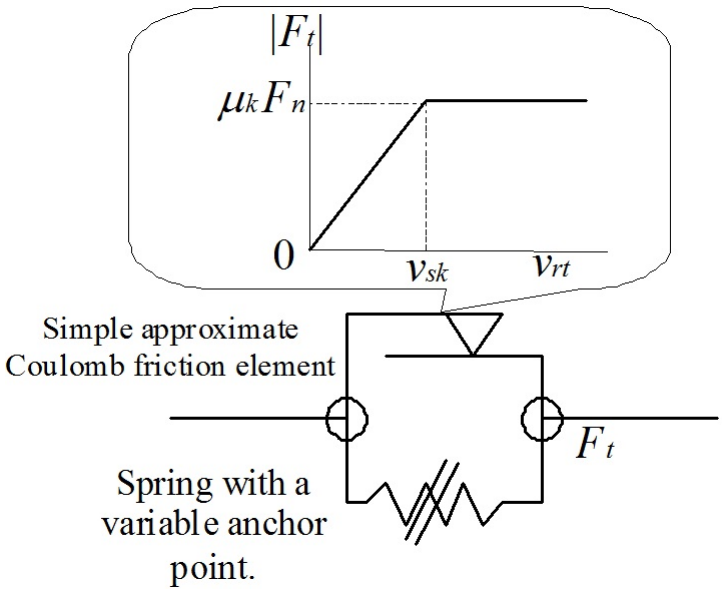

Fig. 2.6. Asperity spring friction model. Ft is the tangential friction force, Fn is the normal force, μ_k is the kinetic friction coefficient, and νrt is the relative tangential velocity between the two points in contact [32].

2.4 Joint Constraints

Each rigid body can have a number of connection points. A connection point is a point on the body where joints can be located. The position and velocity of a connection point are given by Eqs. (2.11a) and (2.11b), respectively, where c_{Lp} is the position of the connection point relative to the body's frame and x_{Gp} and $\dot{x}_{\mathrm{Gp}}$ are the position and velocity of the connection point relative to the global reference frame.

A joint is defined by specifying the relation between connection points. For example, a spherical joint between two connection points is defined as:

$$x_{\mathrm{c1}_{\mathrm{i}}^{\mathrm{t}}} = x_{\mathrm{c2}_{\mathrm{i}}^{\mathrm{t}}} \tag{2.18}$$

where $x_{\mathrm{c1}_{\mathrm{i}}^{\mathrm{t}}}$ is the position of the first point and $x_{\mathrm{c2}_{\mathrm{i}}^{\mathrm{t}}}$ is the position of the second point, both with respect to the global reference frame. This constraint is imposed using the penalty technique as:

$$F_{\mathrm{c}} = k_p|d| + c_p d_i \dot{d}_i \tag{2.19}$$

$$d_i = x_{\mathrm{c1}_{\mathrm{i}}^{\mathrm{t}}} - x_{\mathrm{c2}_{\mathrm{i}}^{\mathrm{t}}} \tag{2.20}$$

$$\dot{d}_i = \dot{x}_{\mathrm{c1}_{\mathrm{i}}^{\mathrm{t}}} - \dot{x}_{\mathrm{c2}_{\mathrm{i}}^{\mathrm{t}}} \tag{2.21}$$

$$F_{\mathrm{c}_{\mathrm{i}}} = F_{\mathrm{c}}\, d_i \tag{2.22}$$

where $F_{\mathrm{c}i}$ is the penalty reaction force on the connection point, k_p is the penalty spring stiffness, and c_p is the penalty damping. The constraint force is applied on the two connection points in opposite directions. Revolute joints can be modeled by placing two spherical joints along a line. Other types of joints such as prismatic, cylindrical, universal, planar, and screw joints can also be modeled by writing the constraint equation, then writing the corresponding penalty forces and moments on the connection points.

The constraint force is transferred to the node at the center of mass of the body as a force and a moment using Eqs. (2.11a) and (2.11b). The constraint forces given by Eq. (2.11a) are assembled into the global structural forces F_{s} in Eq. (2.1). The constraint torques given by Eqs. (2.11b) are assembled into the global structural torques Ts in Eq. (2.2).

2.5 Explicit Solution Procedure

The solution fields for modeling multibody systems are defined at the model nodes. Note that a rigid body modeled as one finite element node. These solutions fields are:

- Translational positions.
- Translational velocities.
- Translational accelerations.
- Rotation matrices.
- Rotational velocities.
- Rotational accelerations.

The explicit time integration solution procedure predicts the time evolution of the above response quantities. An advantage of explicit solution procedures is that they are "embarrassingly" parallel. The procedure described below achieves near linear speed-up with the number of processors on shared memory parallel computers. The procedure is implemented in the DIS [52] (Dynamic Interactions Simulator) code and is outlined below:

1. Prepare the run:
   (a) Set the initial conditions for the solution fields identified above.
   (b) Create a list of all the finite elements (Those also include joints and master contact surfaces which are considered elements).

(c) Create a list of elements that will run on each processor. This is done using an algorithm which tries to make the computational cost on each processor equal.

(d) Create a list of all the prescribed motion constraints.

(e) Calculate the solid masses for each finite element node by looping through the list of finite elements. Note that the masses are fixed in time.

(f) Loop over all the elements and find the minimum time step for the explicit solution procedure.

2. Loop over the solution time and increment the time by Δt each step while doing the following:

(a) Set the nodal values at the last time step to be equal to the current nodal values for all solution fields.

(b) Do 2 iterations (a predictor iteration and a corrector iteration) of the following:

i. Initialize the nodal forces and moments to zero.

ii. Calculate the nodal forces and moments by looping through all the elements (and joints) while calculating and assembling the element nodal forces. This is the most computational intensive step. This step is done in parallel by running each list of elements identified in step 1.c on one processor.

iii. Find the nodal values at the current time step using the semi-discrete equations of motion and the trapezoidal time integration rule (Eqs. 2.1-2.5).

iv. Execute the prescribed motion constraints which set the nodal value(s) to prescribed values.

v. Go to the beginning of step 2.

3. BELT-DRIVE MODEL

The foregoing finite element formulation and solution procedure were incorporated into the DIS [52] flexible multibody dynamics computer code. The two-pulley belt-drive shown in Figure 1.2 is created in DIS and used to study the effect of change in the main material, geometric and operating belt-drive parameters on the steady-state belt drive response (including belt stresses, belt slip and belt-drive energy efficiency). The pulleys' and belt base-line parameters are shown in Tables 3.1 and 3.2, respectively.

The belt rubber matrix is modeled using brick elements with one element for the entire cross-section (i.e. one element through the thickness of the belt) and the belt reinforcements are modeled using 2 cords of truss elements on the top corners of the belt (Figure 1.2). The axial stiffness for each cord for the baseline belt is 40,050 N. Therefore the total belt reinforcements' axial stiffness is $40,050 \times 2 = 80,100N$. The axial stiffness of the belt rubber matrix is 2,250 N. Therefore most of the belt's tension is carried by the reinforcements. Also, the since the reinforcements deformation/strain is very small which means that the belt rubber strain also remains small. Thus the belt rubber can be modeled as a linear elastic material (rather than hyperelastic). The driver and driven pulleys' centers are fixed to ground using revolute joints. The initial conditions of the belt-drive are: zero belt velocity, zero pulleys angular velocity, and the belt tension is set to 500 N (by setting the belt strain to the appropriate value). The total simulation time is 1.6 sec. The explicit time step is about $5 \times 10 - 8sec.$ The belt-drive is assumed to be in a horizontal plane, so gravity is set to 0.

A rotational actuator along with a PD controller is used to control the angular velocity of the driver pulley. The prescribed angular velocity of the driver pulley is shown in Figure 3.1. The angular velocity is ramped up in 0.555 sec to 120 rad/s (1145.915 RPM), then, it is kept constant for the rest of the time. All the subsequent

rubber stress data are measured at the center of the belt cross-section (center of the each element). The baseline model has 388 brick elements and 776 beam elements.

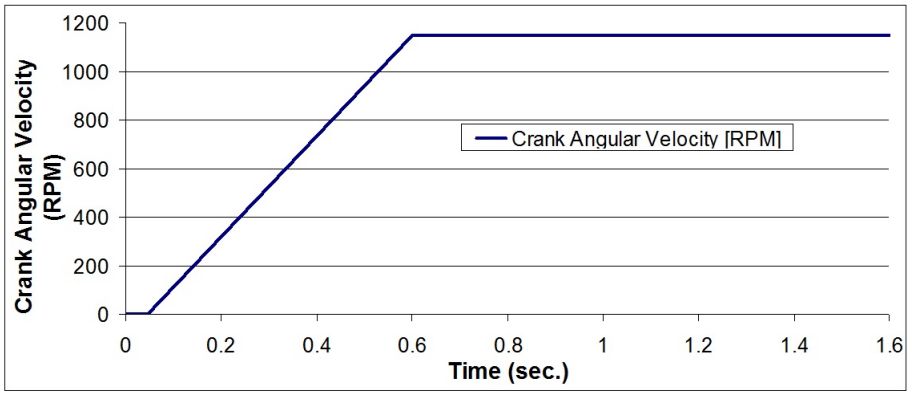

Fig. 3.1. Prescribed angular velocity of the driver pulley.

If the belt rubber thickness is not taken into account (i.e. just the reinforcements are modeled) then the belt-pulley tangential contact stress has two main zones a stick zone where the tangential contact stress is zero and a slip zone where the tangential contact stress is not zero (increases exponentially then decreases to zero when the belt exists the pulley) (Figure 1.3 and 3.2). In the stick zone the relative velocity between the belt and the pulley is nearly zero. In the slip zone the belt is moving (creeping) slower than the pulley on the driver pulley and faster than the pulley on the driven pulley. The stick zone on the driver pulley occurs at the inlet of the driver pulley on the high tension span. The stick zone on the driven pulley occurs at the inlet of the driven pulley on the low tension span (Figure 3.2). Thus when the belt enters a pulley it is moving at the same speed as the pulley and just lays itself on the pulley without developing any friction forces. Friction develop on the exist side of the belt on a pulley. As the opposing torque increases the size of the slip arc increases and the size of the stick arc decreases. Once the slip arc covers the full face of the pulley and the stick arc is zero, then gross slip of the belt on the pulleys start to occur. If the rubber thickness is taken into account this stick-slip behavior becomes

more complicated. The driver pulley develops a positive traction zone (which covers the slip arc and part of the stick arc) and a negative traction zone (on part of the stick arc). The driven pulley develop one traction zone which covers both the slip and stick arcs (Figure 1.3). This behavior will be further investigated in Section 4.1.

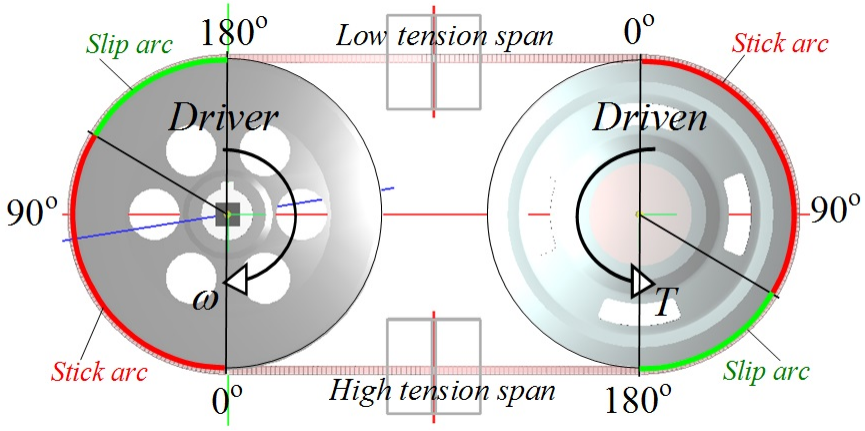

Fig. 3.2. Two-pulley belt drive. Top figure shows the belt brick elements. In the bottom figure ω is the input angular velocity of the driver pulley and T is the applied opposing torque on the driven pulley.

Table 3.1.
Table of the baseline model pulley parameters of the belt-drive.

Parameter	**Driver Pulley**	**Driven Pulley**
X$[mm]$	0	220
Y$[mm]$	162.5	162.5
Pulley Moment of Inertia$[kg.cm^2]$	20000	200
Coefficient of Friction	0.65	0.65
Fixed Opposing Torque$[N.m]$		35
Width$[mm]$	50	50

Table 3.2.
Table of the baseline model belt parameters of the belt-drive.

Parameters	**Values**
Element Length[mm]	2.5
Rubber Mass Density[kg/m^3]	300
Rubber Young's Modulus[Pa]	2.5E+07
Rubber Poisson's Ratio	0.3
Rubber Damping Modulus[$Pa.s$]	0.3
Belt Thickness[mm]	3
Belt Width[mm]	30
Nominal Belt Tension[mm]	500
Contact Friction Spring Stiffness[$N/m/m^2$]	2E+11
Contact Velocity Stiffness[$N.s/m$]	4E+06
Normal Contact Stiffness Per Unit Area[$N/m/m^2$]	8E+09
Normal Contact Damping[$N.s/m/m^2$]	4E+06
Truss Reinforcements Axial Stiffness (EA) [N]	40050
Truss Reinforcements Axial Damping (CA) [$N.s$]	0.1
Truss Reinforcements Bending Stiffness (EI) [$N.m^2$]	0
Truss Reinforcements Bending Damping (CI) [$N.m^2.s$]	0
Truss Reinforcements Mass per Unit Length [kg/m]	0.0286

3.1 Response Calculations

The main belt rubber stresses are:

- Axial stress along the length of the belt: $\sigma_{11} = \sigma_A$
- Lateral stress along the width of the belt: $\sigma_{22} = \sigma_L$

- Normal stress along the height of the belt: $\sigma_{33} = \sigma_N$
- Shear stress due to shearing of the belt rubber along the length of the belt: τ

The belt stresses are calculated from the belt strains using the linear elastic stress-strain relations:

$$\sigma_A = \frac{E}{1+\nu}(\epsilon_A + \frac{\nu}{1-2\nu}(\epsilon_A + \epsilon_L + \epsilon_N)) \tag{3.1}$$

$$\sigma_L = \frac{E}{1+\nu}(\epsilon_L + \frac{\nu}{1-2\nu}(\epsilon_A + \epsilon_L + \epsilon_N)) \tag{3.2}$$

$$\sigma_L = \frac{E}{1+\nu}(\epsilon_N + \frac{\nu}{1-2\nu}(\epsilon_A + \epsilon_L + \epsilon_N)) \tag{3.3}$$

$$\tau = \frac{E}{1+\nu}\,\gamma \tag{3.4}$$

where ϵ_A, ϵ_L, ϵ_N and γ are the axial, lateral, normal and shear strains of the belt rubber. All the belt rubber stresses are calculated at the center of the brick element.

The belt slip is calculated using the angular velocity ratio of the driven pulley over the driver pulley:

$$r = \frac{\overline{\omega}_{driven}}{\overline{\omega}_{driver}} \tag{3.5}$$

where $\overline{\omega}_{driver}$ and $\overline{\omega}_{driven}$ are the average driver and driven pulley angular velocities averaged from time 1 to time 1.6 sec.

The belt energy efficiency is calculated using the power ratio of the driven pulley output power over the driver pulley input power:

$$\eta = \frac{\overline{\omega}_{driven}\, T_{driven}}{\overline{\omega}_{driver}\, T_{driver}} \tag{3.6}$$

where T_{driver} is the average driver pulley applied torque averaged from time 1 to time 1.6 sec and T_{driven} is the input fixed driven pulley opposing torque. Note that the driver angular velocity is controlled using a rotary actuator and a PID controller to

follow the profile in Figure 3.1. The driver rotary actuator applies the torque T_{driver} in order to maintain the driver angular velocity at 120 rad/sec.

4. EFFECT OF GEOMETRIC PARAMETERS

4.1 Belt Thickness

Figures 4.1 to 4.13 show the effect of belt rubber thickness on the steady-state response of the belt-drive. Figures 4.1 and 4.1 show the driver and driven pulleys' tangential contact stress and rubber shear stress. Figure 4.3 shows the belt rubber shear stress over the entire length of the belt. As expected the belt rubber experiences shear only when the belt is over one of the pulleys. Also, the tangential contact stress between the belt and the pulley is nearly equal to the rubber shear stress. The driver pulley has a negative traction zone from 0 to about 42^o and a positive traction zone from 44^o to 180^o. The maximum magnitude of the negative traction increases with the belt thickness; whereas the maximum magnitude of the positive traction only increases slightly with belt thickness. The driven pulley only has a positive traction zone. But the positive traction zone is divided into a stick sub-zone where the belt shear stress is low and a slip sub-zone where the belt shear is large. As the belt thickness increases the magnitude of the belt shear stress in the stick sub-zone increases and decreases in the slip sub-zone. Figure 4.1 also shows that the transition angle (44^o) between the negative traction zone and the positive traction zone on the driver pulley is not a function of the belt thickness. Figures 4.4 and 4.5 show the driver and driven pulleys' normal contact stress and rubber normal stress. As expected the normal contact stress is nearly equal to the rubber normal stress. For the driver pulley the maximum normal stress is 12% higher for the 4 mm thick belt than the 1 mm thick belt. For the driven pulley the maximum normal stress is nearly insensitive to the belt thickness, but the average normal stress is slightly higher for the thicker belt. Figure 4.6 shows the driver and driven pulleys belt tension. Similar to the belt normal stress the maximum belt tension is about 12% higher for the 4 mm

thick belt than the 1 mm thick belt. For the driven pulley the maximum belt tension is nearly insensitive to the belt thickness, but the average tension is higher for the thicker belt. Figures 4.7 and 4.8 show the belt tension and belt rubber axial stress, respectively, over the entire belt length. As expected, the belt rubber axial stress is negative (compression) and is large over the pulleys due to bending of the belt around the pulleys. Figures 4.10 and 4.11 show the time-histories of the steady-state driver and driven pulleys' angular velocities and applied torque, respectively. The driver pulley's angular velocity is fixed at -120 rad/s and the driven pulley's torque is fixed at 35 N.m. At steady state, the driver pulley's torque and driven pulley's angular velocity have small oscillations. The oscillations may be due to the belt polygonal discretization. The driver pulley's torque exhibits pulses, which are characteristic of stick-slip friction. Figure 4.12 shows that the driven over driver pulley's angular velocity ratio decreases as the belt thickness increases. Figure 4.13 shows that the belt-drive energy efficiency decreases as the belt thickness increases.

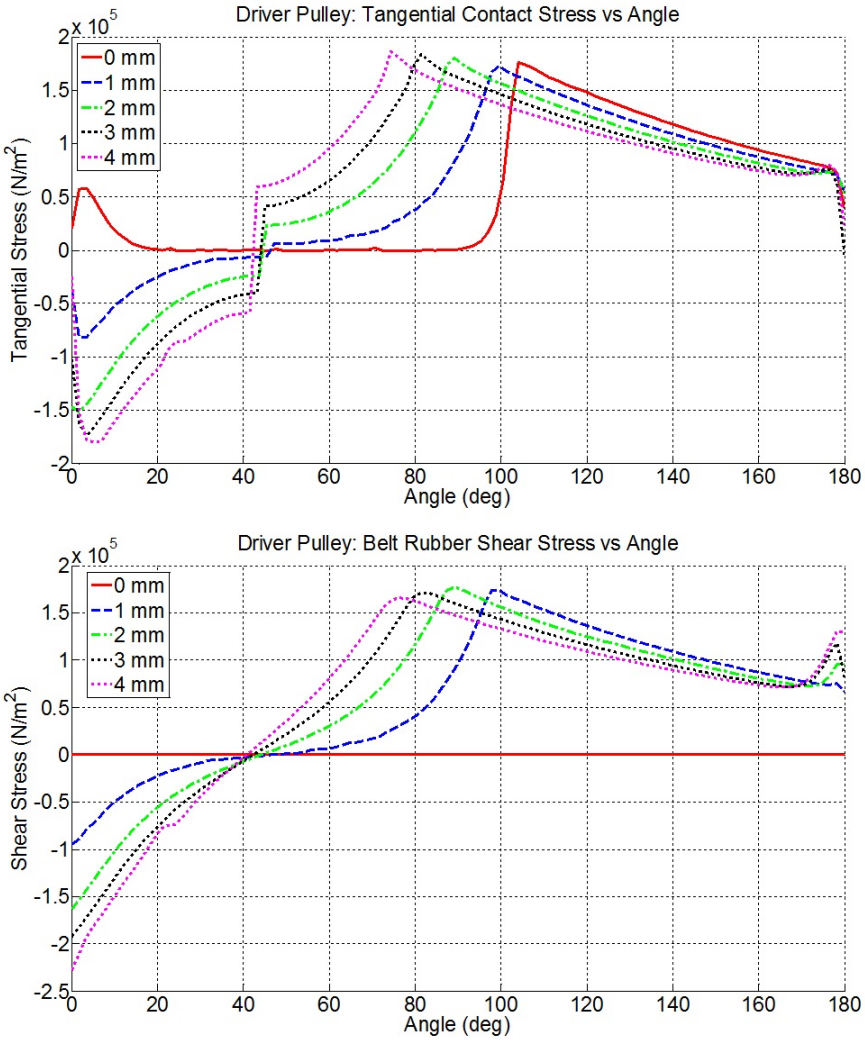

Fig. 4.1. Driver pulley tangential contact stress and rubber shear stress as a function of the belt rubber thickness.

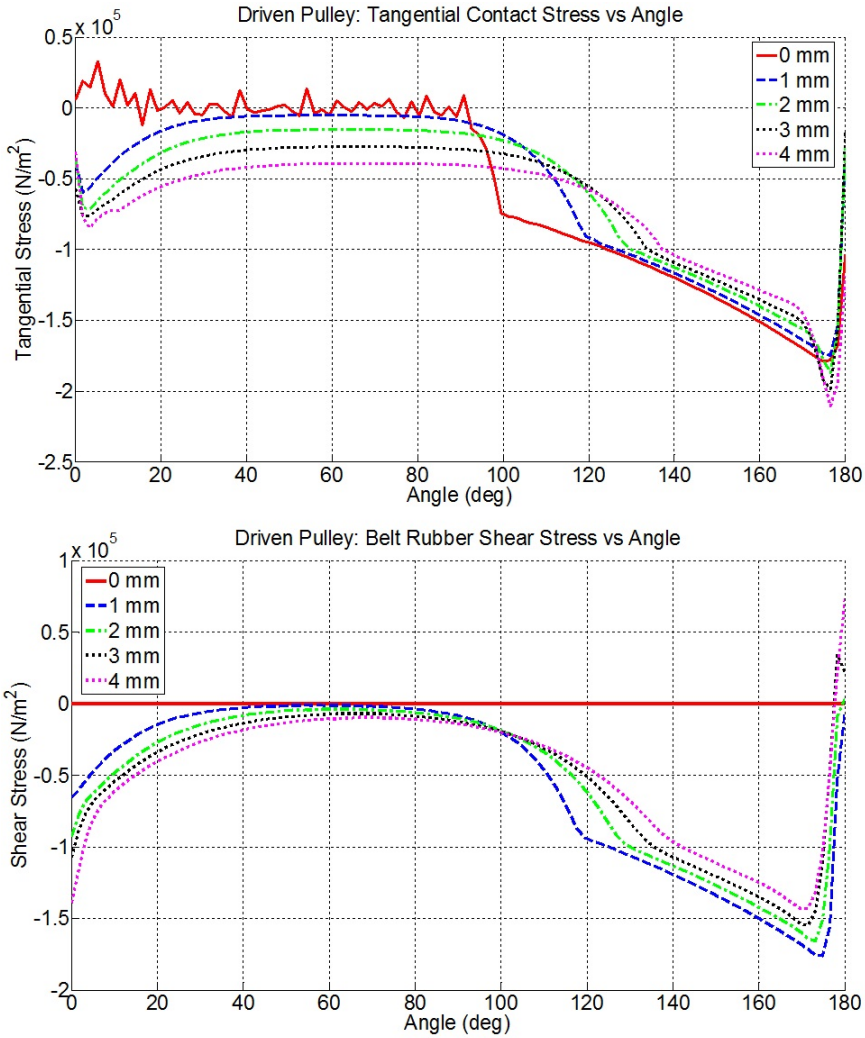

Fig. 4.2. Driven pulley tangential contact stress and rubber shear stress as a function of the belt rubber thickness.

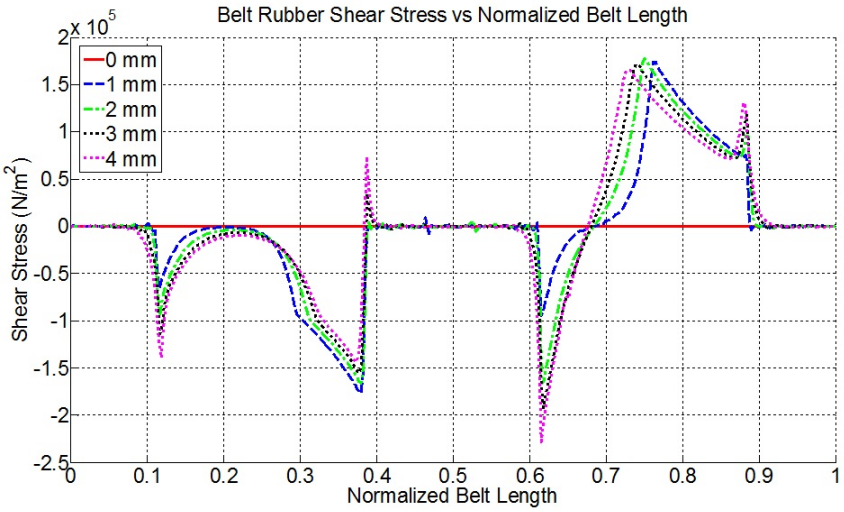

Fig. 4.3. Belt rubber shear stress over the normalized belt length as a function of belt rubber thickness.

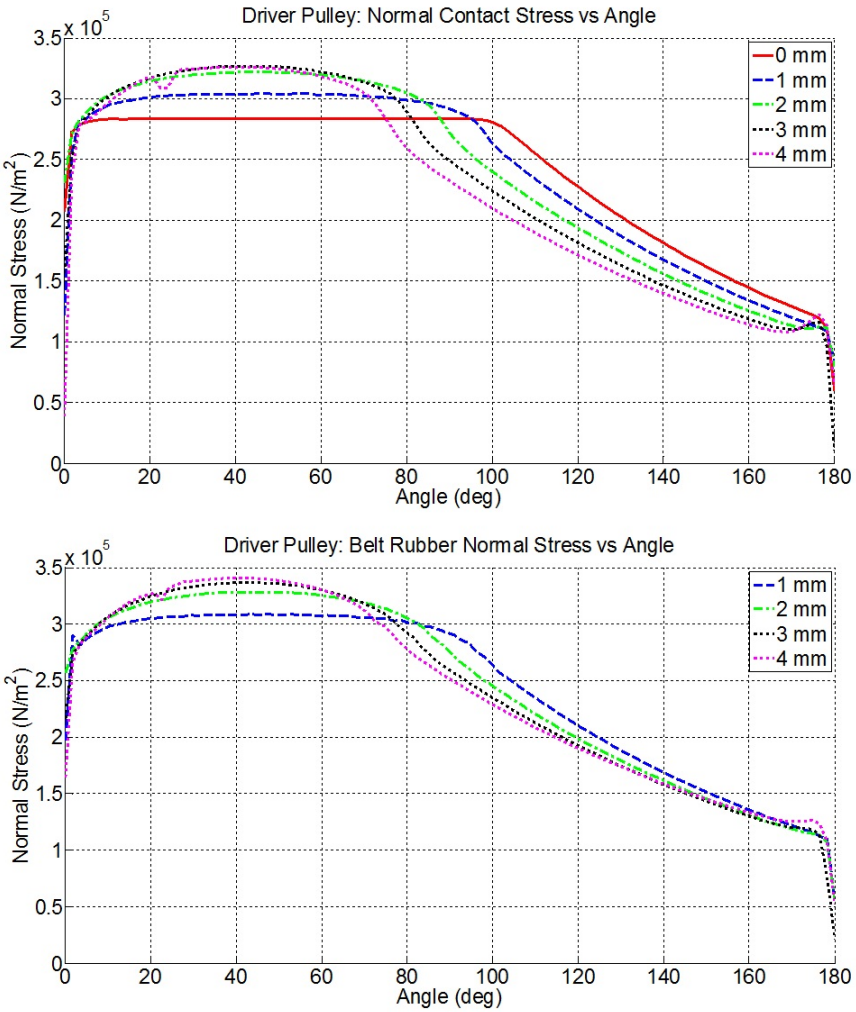

Fig. 4.4. Driver pulley normal contact stress and rubber normal stress as a function of the belt rubber thickness.

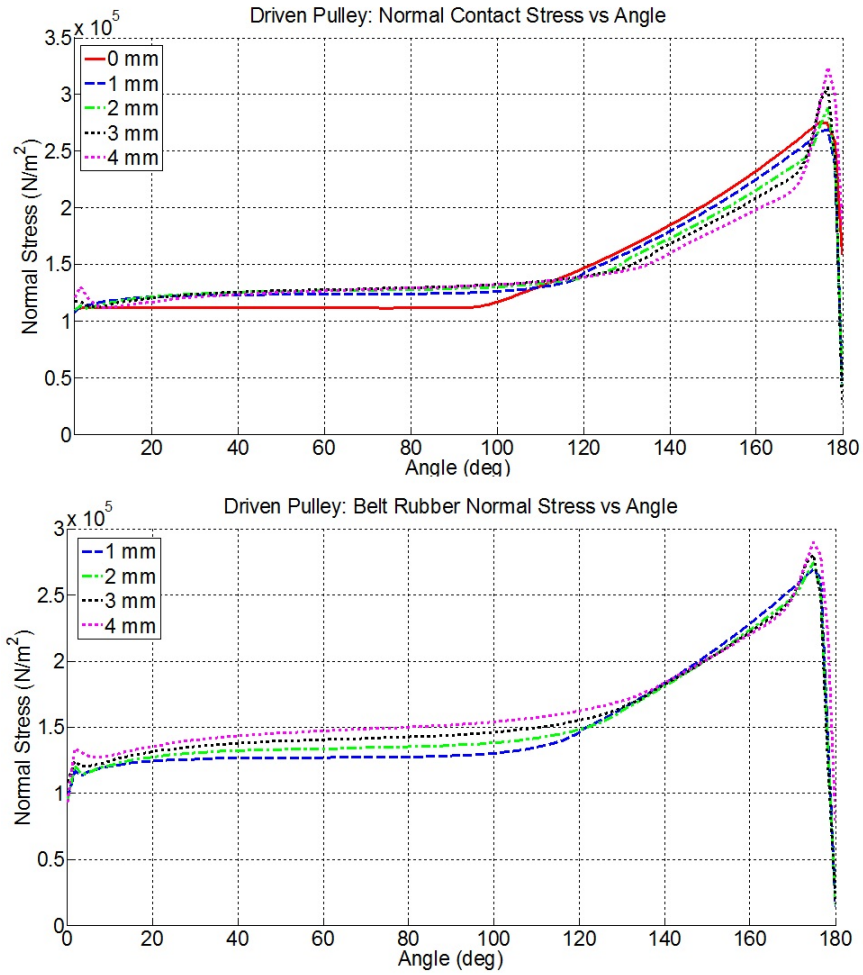

Fig. 4.5. Driven pulley normal contact stress and rubber normal stress as a function of the belt rubber thickness.

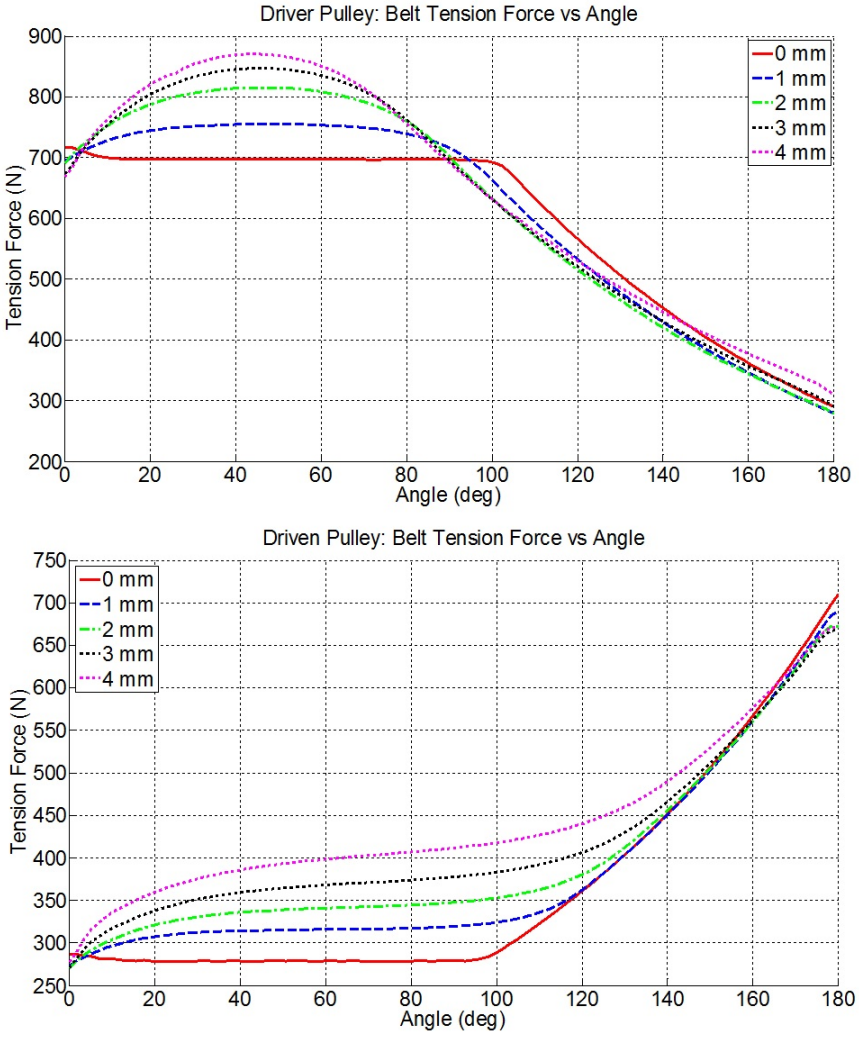

Fig. 4.6. Driver and driven pulleys reinforcements tension force over the pulleys as a function of the belt rubber thickness.

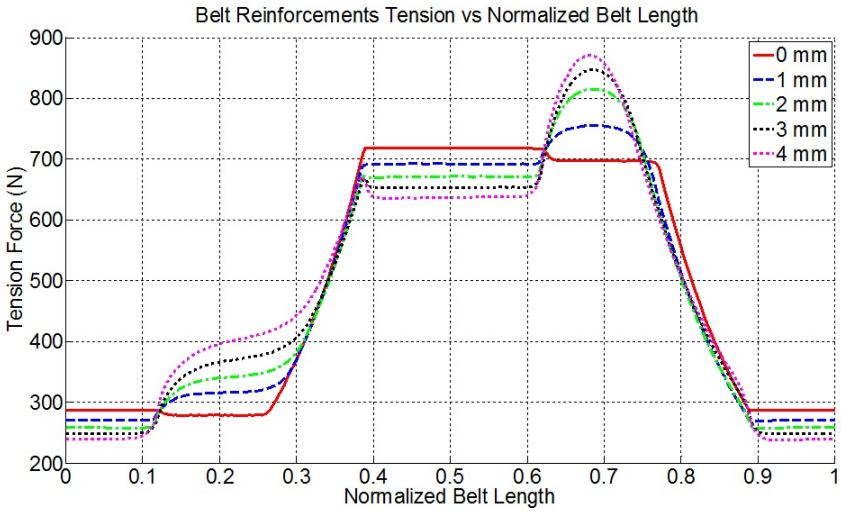

Fig. 4.7. Reinforcements tension force over the belt length as a function of the belt rubber thickness.

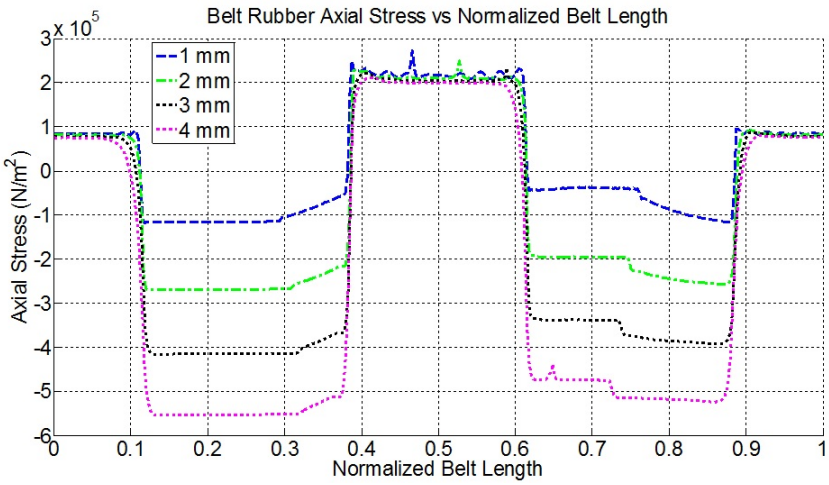

Fig. 4.8. Belt rubber axial stress over the belt length as a function of the belt rubber thickness.

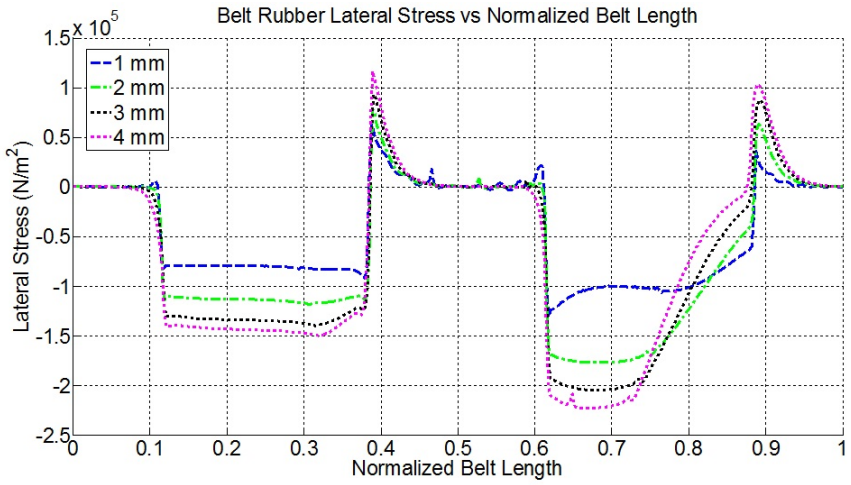

Fig. 4.9. Belt rubber lateral stress over the belt length as a function of the belt rubber thickness.

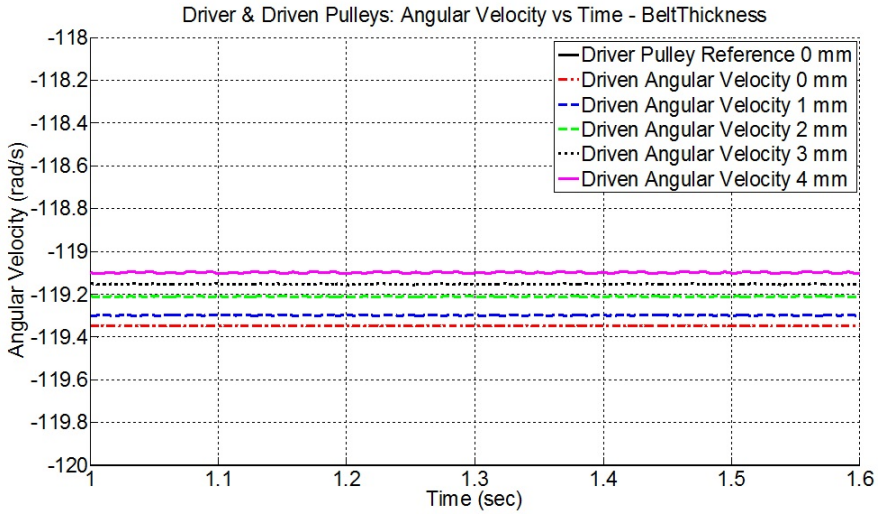

Fig. 4.10. Time-history of the driver and driven pulleys angular velocities as a function of belt thickness.

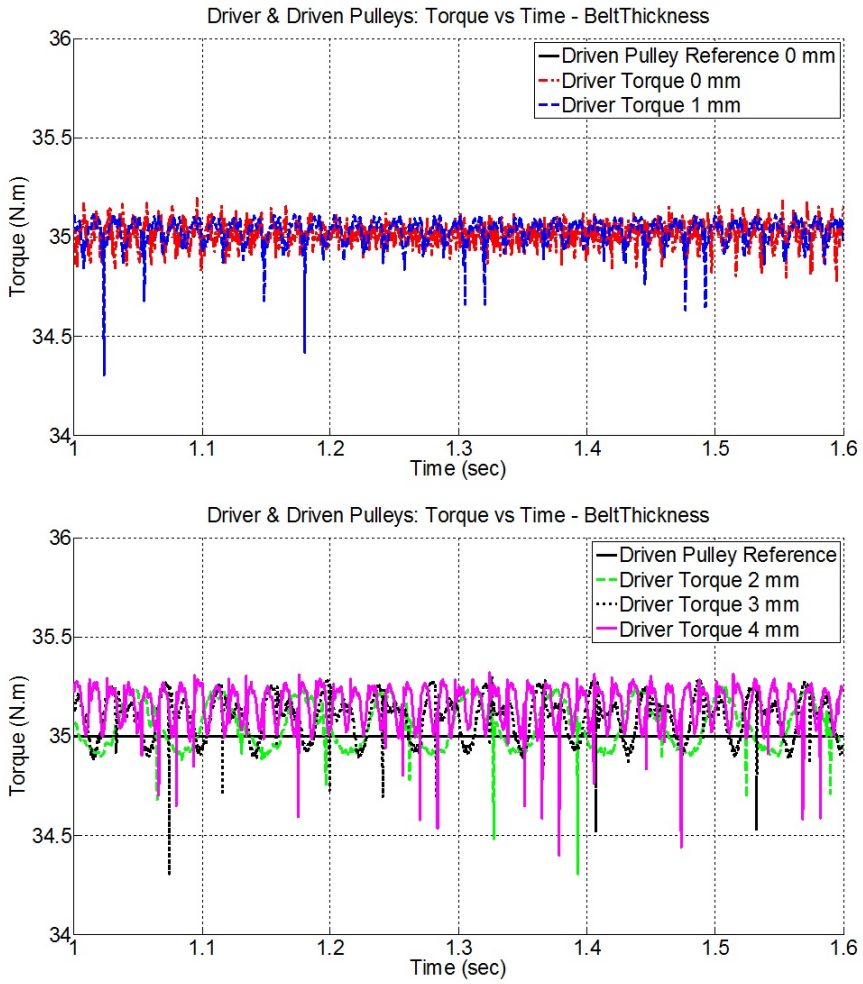

Fig. 4.11. Time-history of the driver applied torque and driven pulley opposing torque as a function of belt thickness.

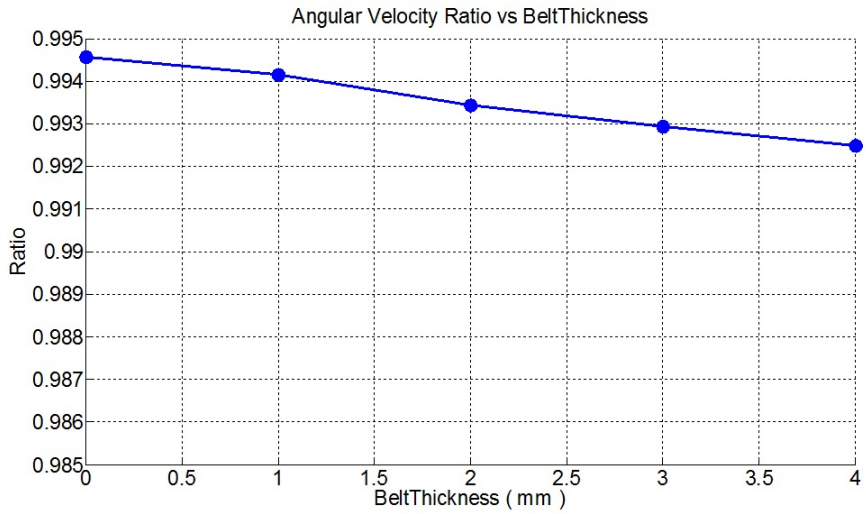

Fig. 4.12. Angular velocity ratio (driven/driver) as a function of the belt thickness.

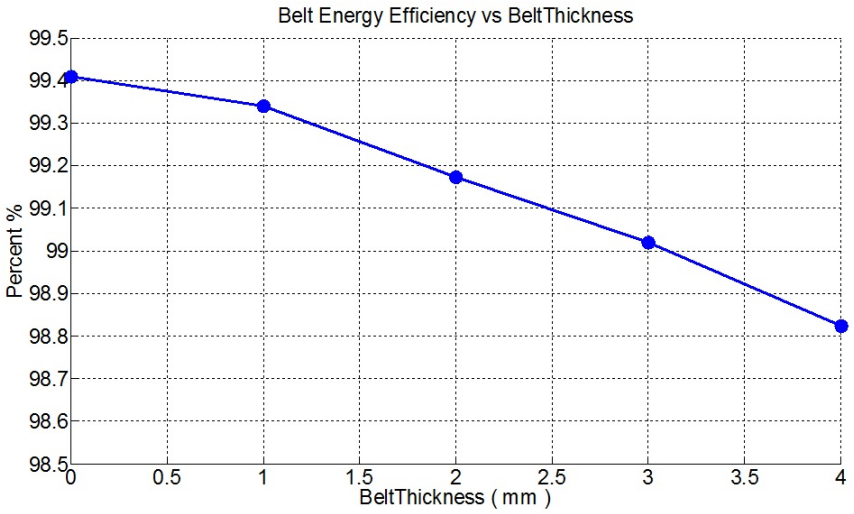

Fig. 4.13. Belt drive energy efficiency as a function of the belt thickness.

4.2 Pulley Center Distance

Figures 4.14 to 4.25 show the effect of the pulleys' center distance (or belt total length) on the steady-state response of the belt-drive. Figure 4.14 shows that the belt-pulley tangential contact stress and the belt rubber shear stress are nearly insensitive to the pulleys' center distance. Figures 4.17 and 4.18 show that the belt-pulley normal contact stress, the belt rubber normal stress, and the belt tension increase slightly with the pulleys' center distance. This is mainly due to the increase in inertia of the belt caused by the increased belt length. Figure 4.21 shows that the belt rubber axial stress is nearly insensitive to the pulleys' center distance. Figure 4.23 shows that the stick-slip friction pulses in the driver's applied torque are unaffected by the pulleys' centers distance. Figure 4.24 and 4.25 show that the driven over driver pulley's angular velocity ratio and the belt-drive energy efficiency are nearly unaffected by the pulleys' center distance.

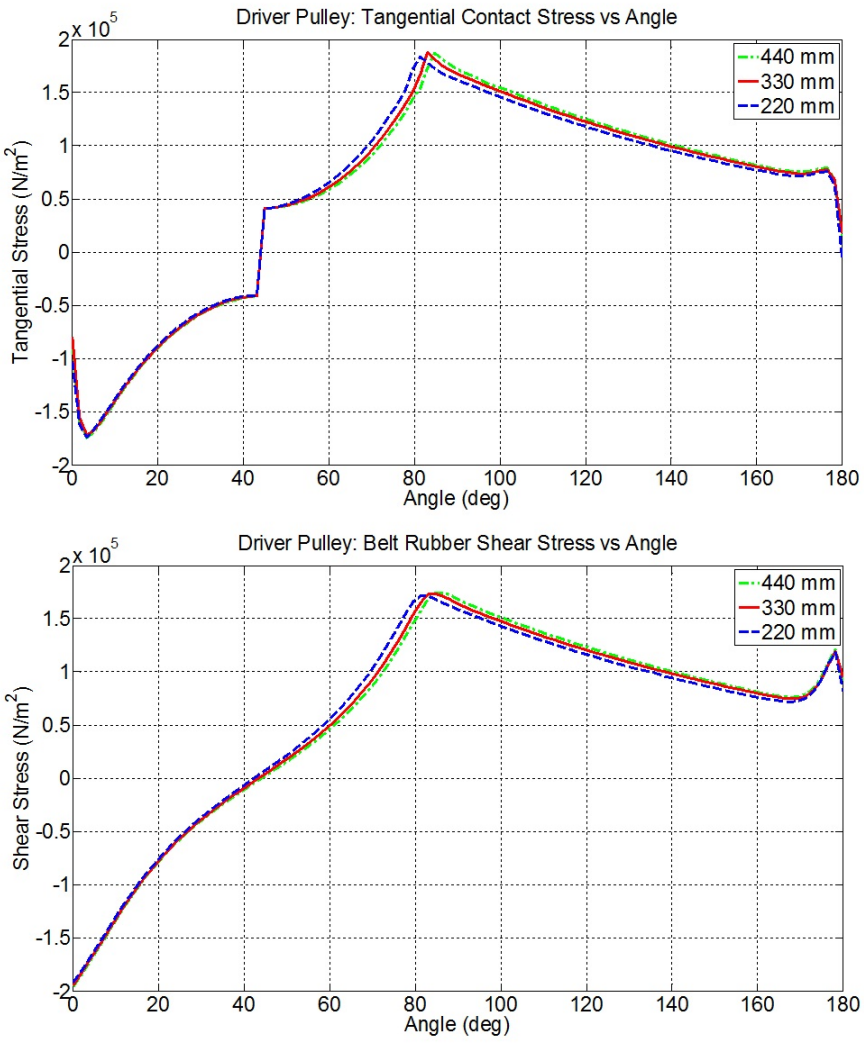

Fig. 4.14. Driver pulley tangential contact stress and rubber shear stress as a function of the pulley center distance.

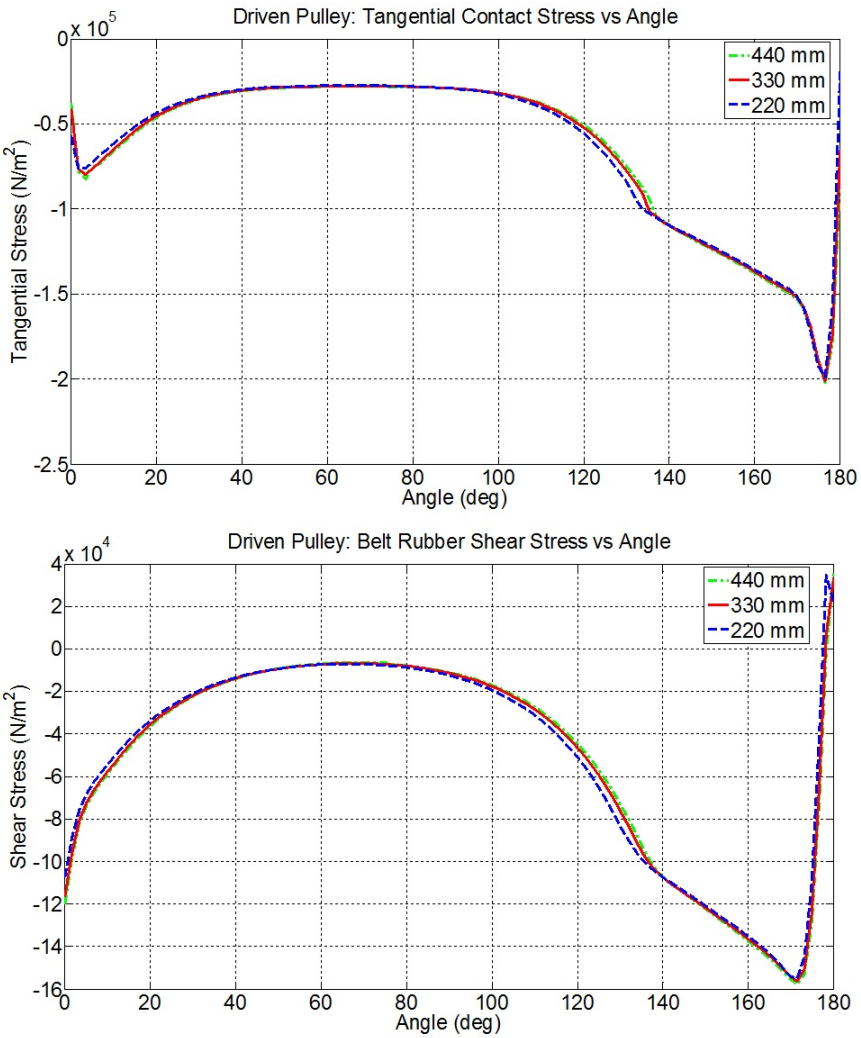

Fig. 4.15. Driven pulley tangential contact stress and rubber shear stress as a function of the pulley center distance.

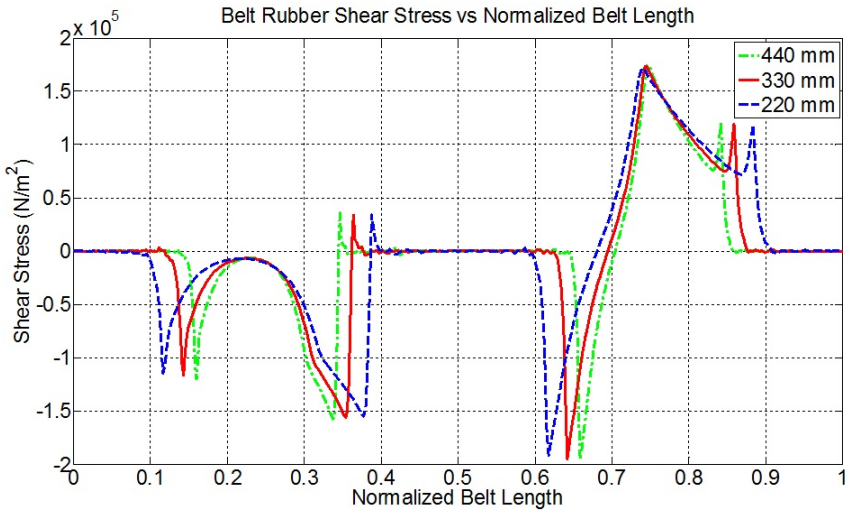

Fig. 4.16. Belt rubber shear stress over the normalized belt length as a function of the pulley center distance.

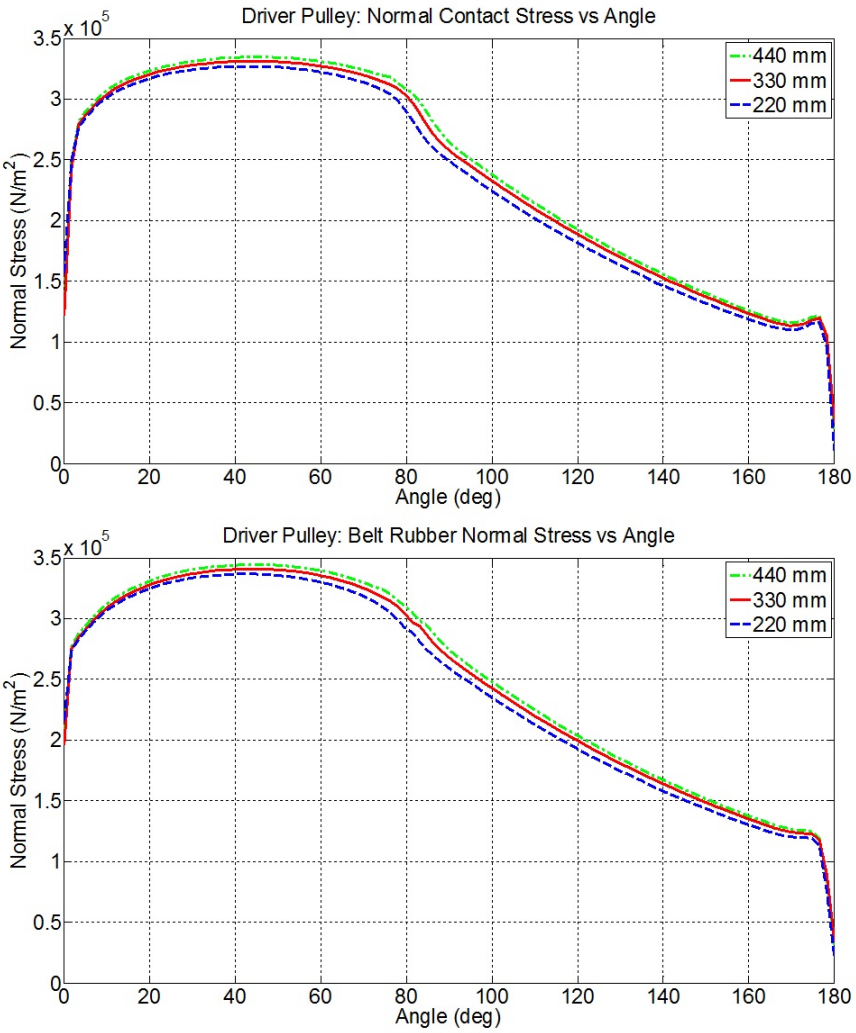

Fig. 4.17. Driver pulley normal contact stress and rubber normal stress as a function of the pulley center distance.

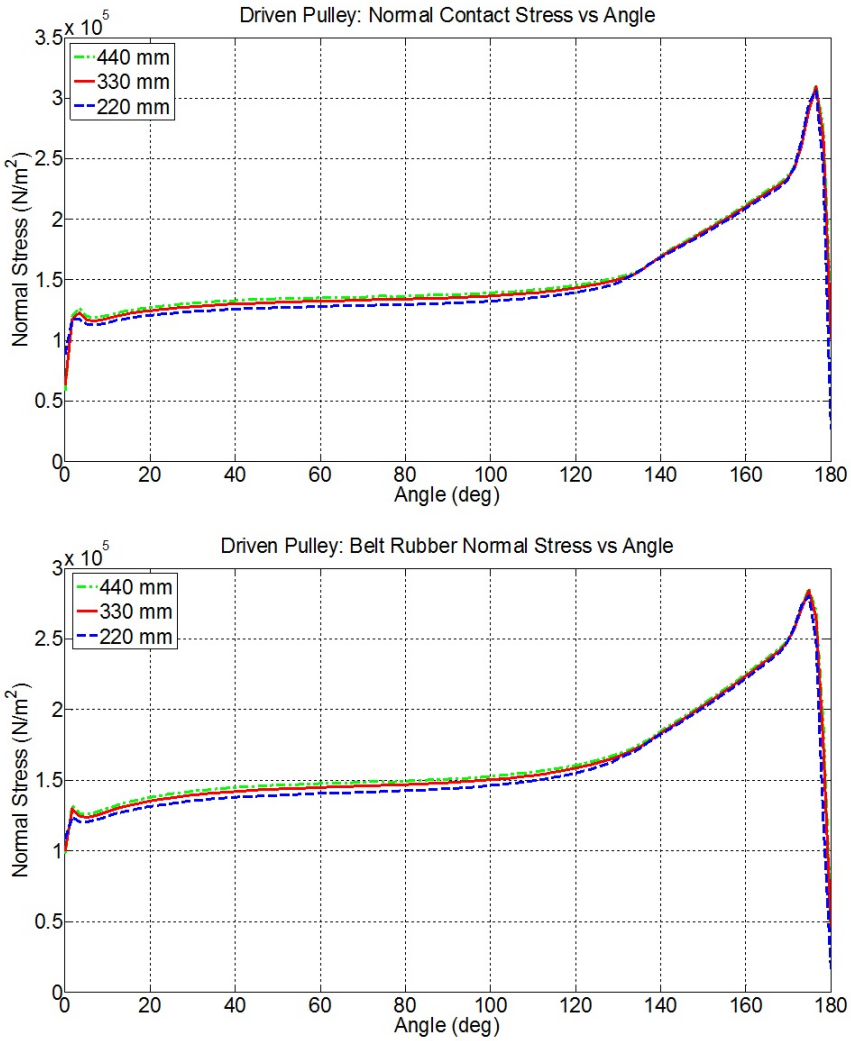

Fig. 4.18. Driven pulley normal contact stress and rubber normal stress as a function of the pulley center distance.

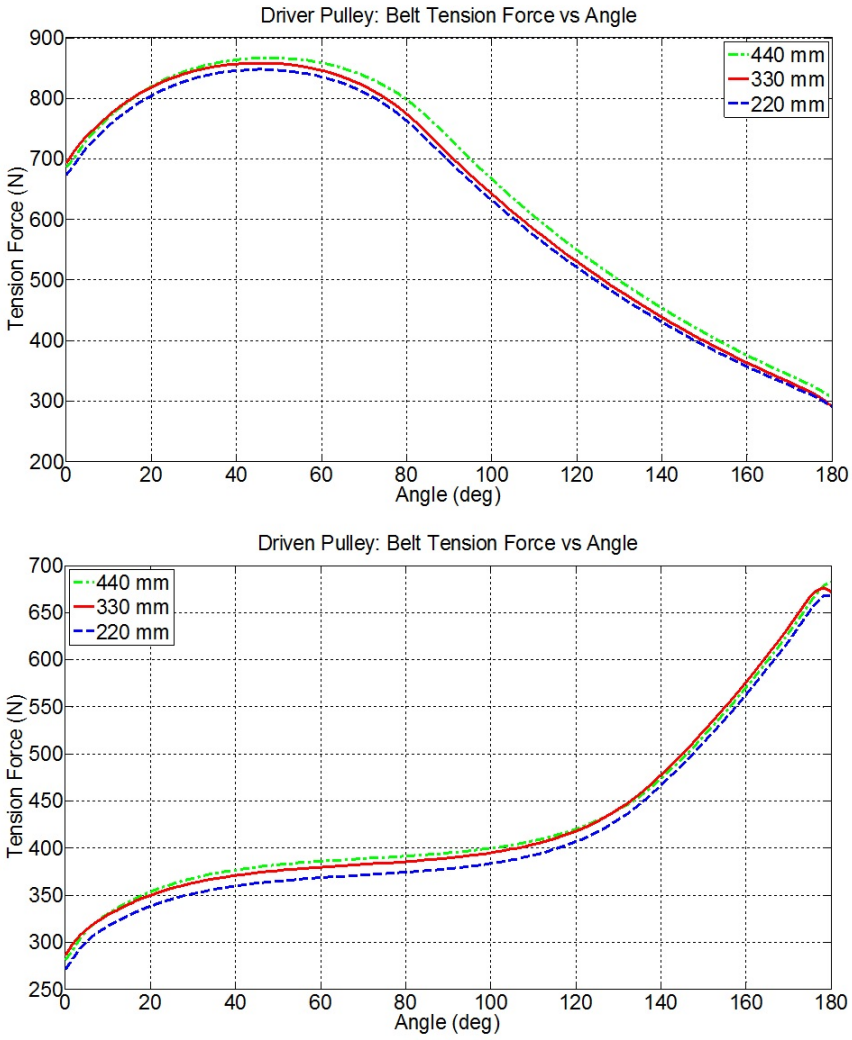

Fig. 4.19. Driver and driven pulleys reinforcements tension force over the pulleys as a function of the pulley center distance.

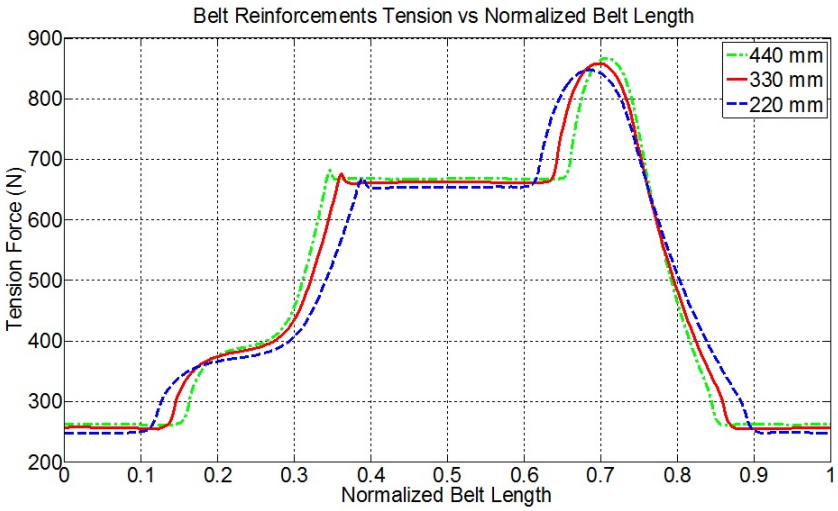

Fig. 4.20. Reinforcements tension force over the belt length as a function of the pulley center distance.

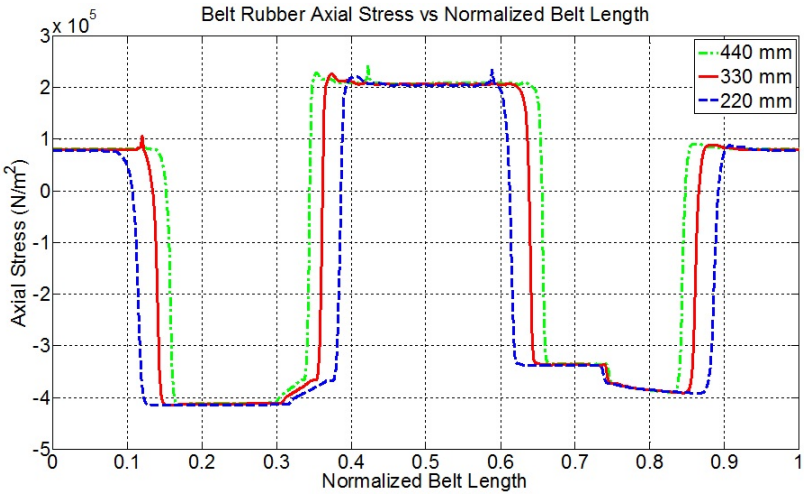

Fig. 4.21. Belt rubber axial stress over the belt length as a function of the pulley center distance.

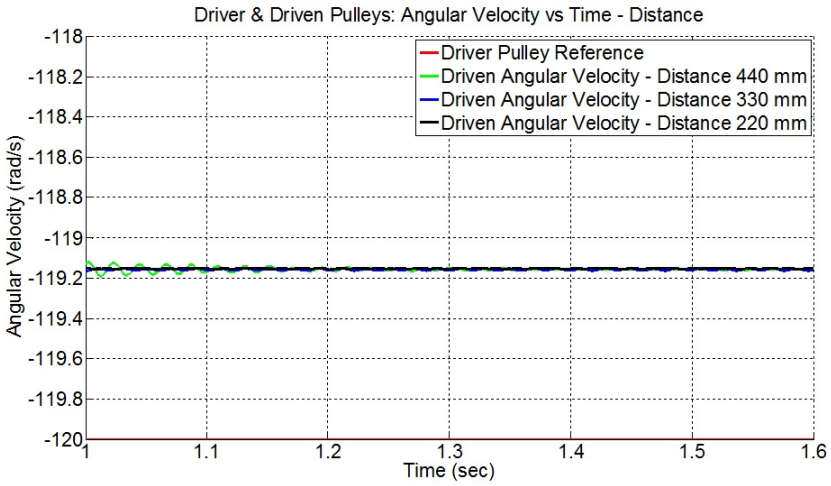

Fig. 4.22. Time-history of the driver and driven pulleys angular velocities as a function of the pulley center distance.

Fig. 4.23. Time-history of the driver applied torque and driven pulley opposing torque as a function of the pulley center distance.

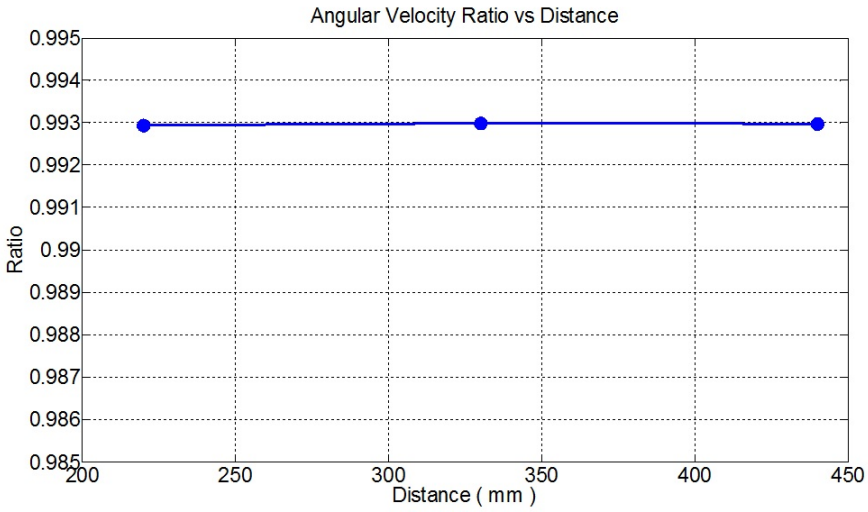

Fig. 4.24. Angular velocity ratio (driven/driver) as a function of the pulley center distance.

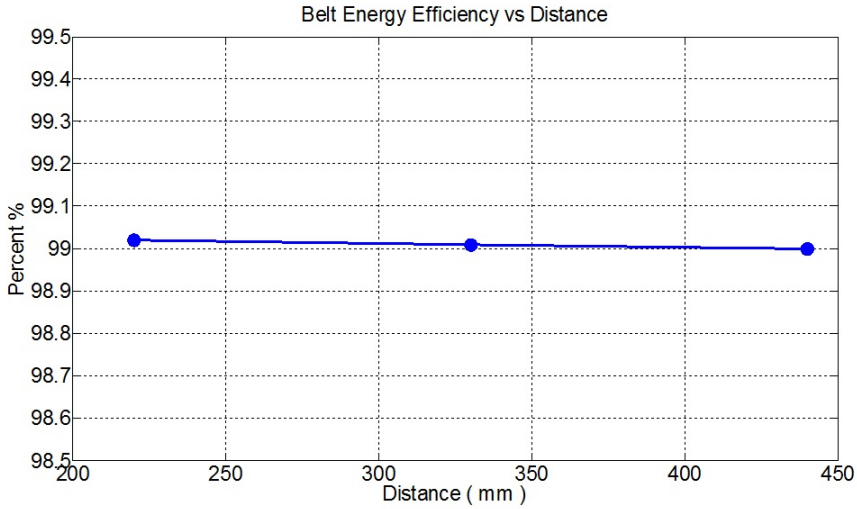

Fig. 4.25. Belt drive energy efficiency as a function of the pulley center distance.

4.3 Pulley Diameter Ratio

The pulley's diameter ratio is calculated as the driven pulley diameter over the driver pulley diameter. A diameter ratio of 2 means that the diameter of the driven pulley is twice that of the driver pulley, and a diameter ratio of 0.5 means that the diameter of the driven pulley is half that of the driver pulley (Figure 4.26). Note that the belt-pulley contact angle or wrap angle is less than 180^o over the smaller pulley and is larger than 180^o over the larger pulley. Also note that the contact area is more than 2 times larger for the large pulley since its diameter is twice as large and its wrap angle is larger. Table 4.1 shows the main parameters of the diameter ratio runs. Note that the ideal power transmitted by the belt-driver is not constant. It is 2100, 4200, and $8400W$ for the 2, 1 and 0.5 diameter ratios, respectively. The nominal pulley diameter is 162.5 mm. The pulley center distance is 440 mm.

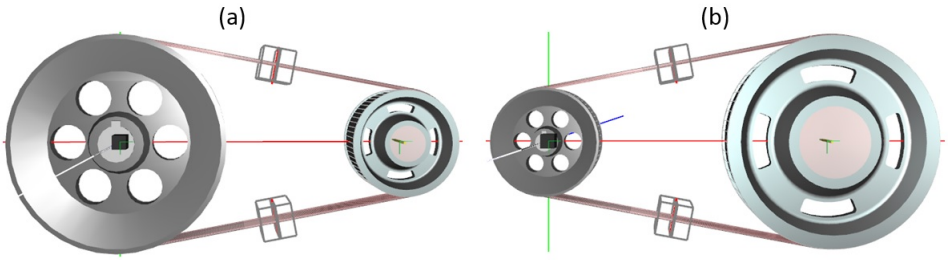

Fig. 4.26. (a) 0.5 and (b) 2 diameter ratios. Driver pulley is on the right and driven pulley is on the left.

Table 4.1.
Parameters for the pulley diameter ratio runs.

Diameter Ratio	**Ratio 2.0**	**Ratio 1.0**	**Ratio 0.5**
Normalized Driver Diameter	1	1	2
Normalized Driven Diameter	2	1	1
Ideal Driver Torque$[N.m]$	17.5	35	35
Applied Driven Torque$[N.m]$	-35	-35	-35
Driver Angular Vel.$[rad/s]$	120	120	120
Ideal Driven Angular Vel.$[rad/s]$	60	120	240
Power$[W]$	2100	4200	8400

Figures 4.27 to 4.38 show the effect of the pulleys' diameter ratio on the steady-state response of the belt-drive. Figure 4.27 shows that the size of the negative traction zone on the driver pulley increases when the pulley diameter ratio increases. Figure 4.28 shows that the size of the stick zone on the driven pulley increases with the diameter ratio. Figure 4.35 and 4.37 show that the driven pulley angular velocity of 2.0 ratio is half of the baseline where it is twice for 0.5 ratio due to diameter variation. Figure 4.36 shows the corresponding variation for driven pulley opposing torque. Figure 4.38 shows that the belt energy efficiency is lowest for the 1:1 diameter ratio belt-drive.

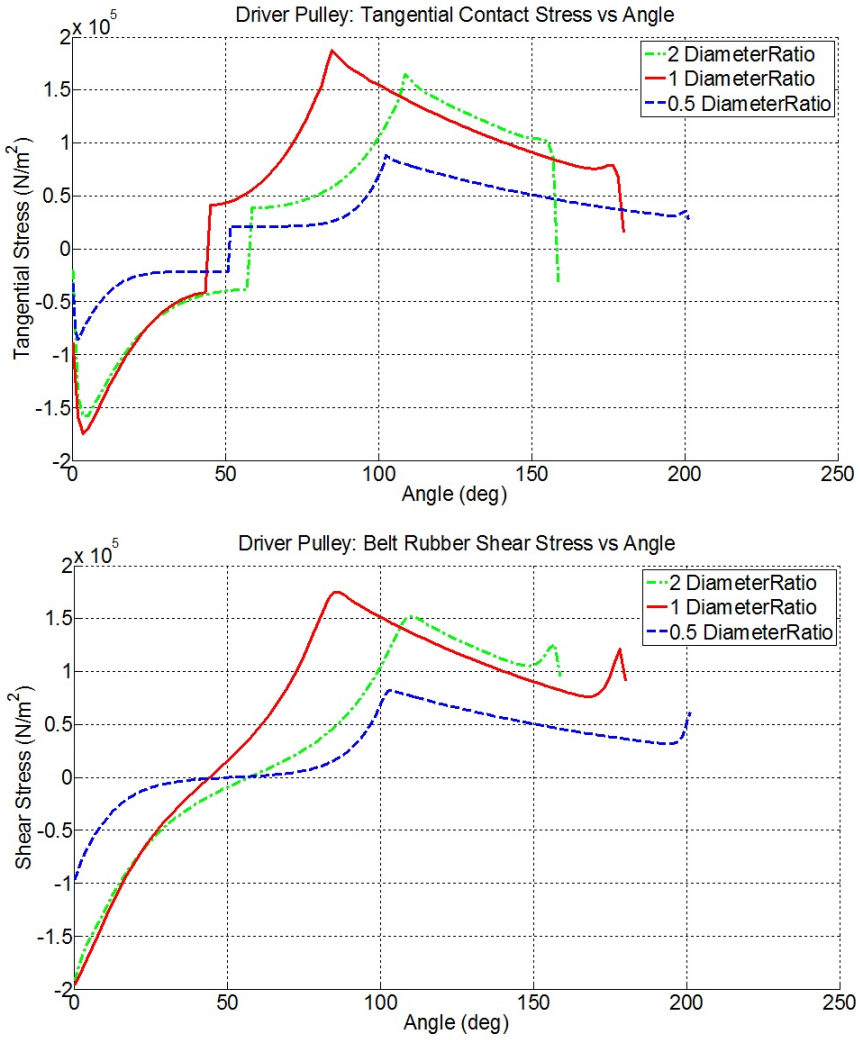

Fig. 4.27. Driver pulley tangential contact stress and rubber shear stress as a function of the pulley diameter ratio.

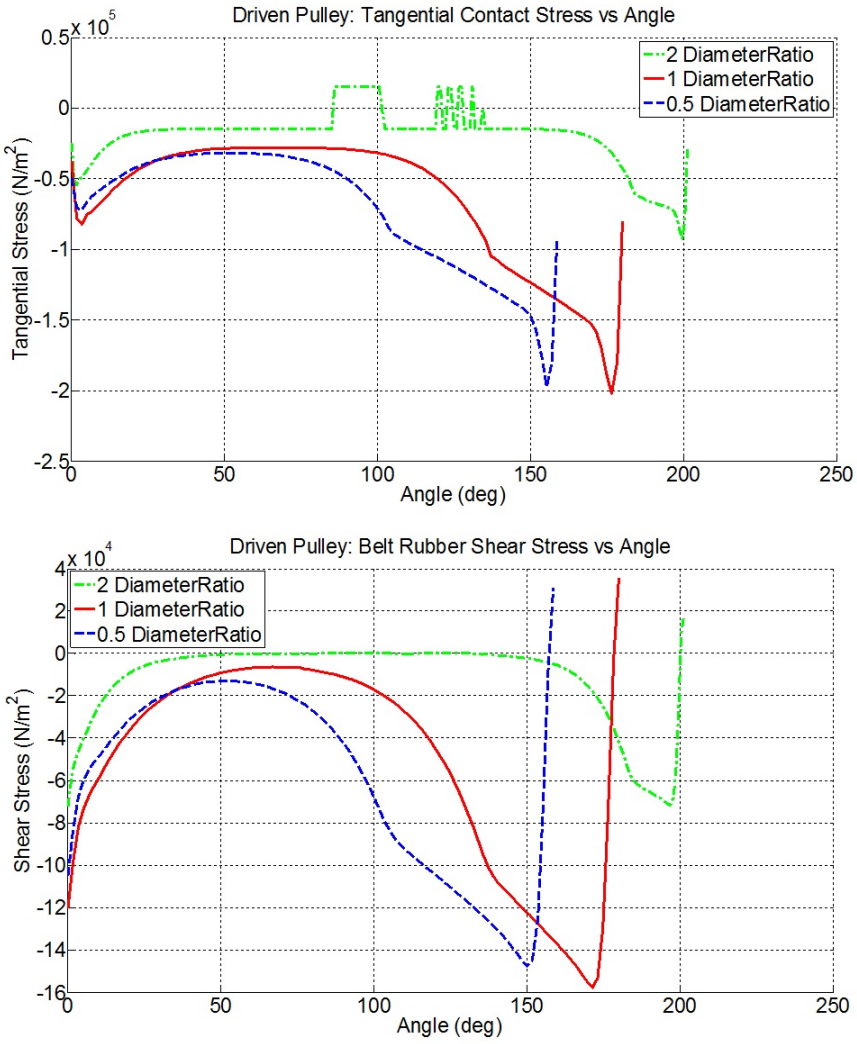

Fig. 4.28. Driven pulley tangential contact stress and rubber shear stress as a function of the pulley diameter ratio.

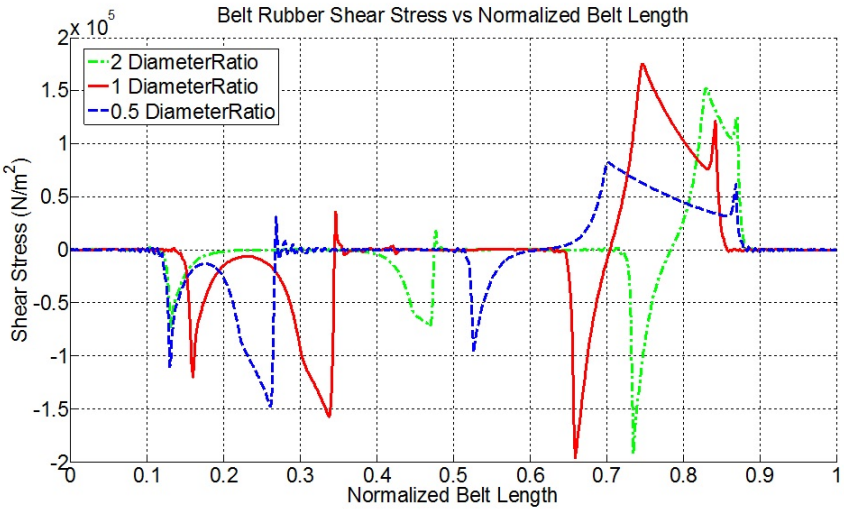

Fig. 4.29. Belt rubber shear stress over the normalized belt length as a function of the pulley diameter ratio.

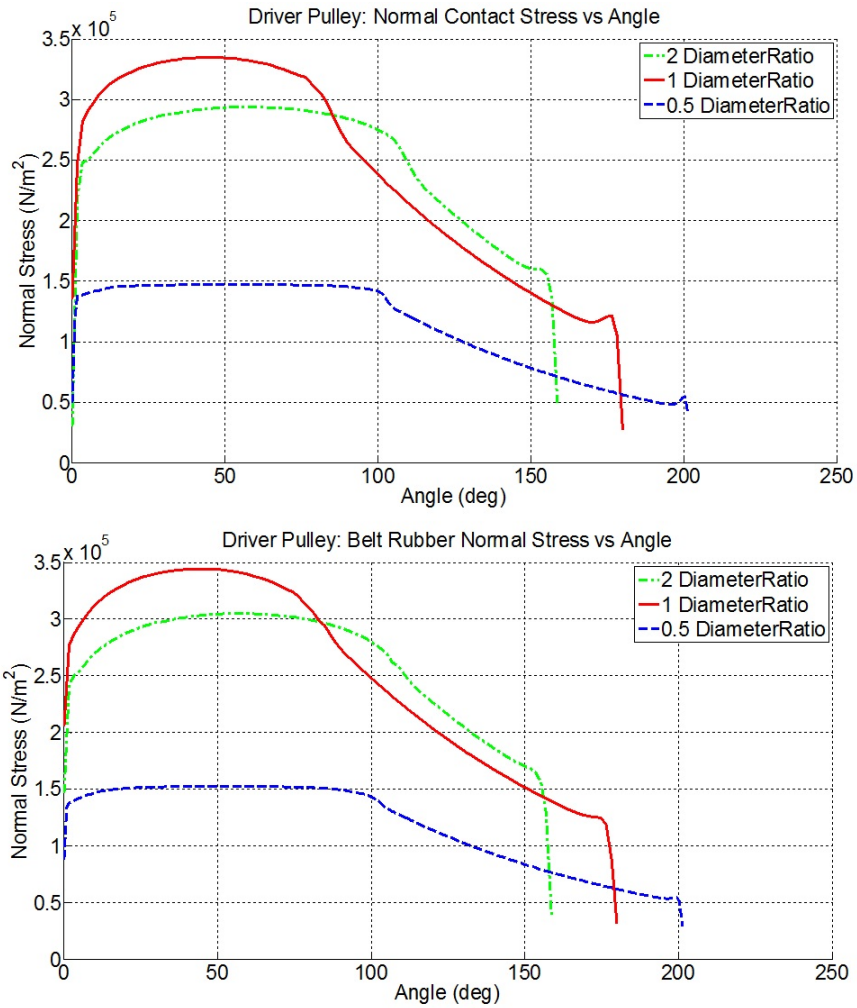

Fig. 4.30. Driver pulley normal contact stress and rubber normal stress as a function of the pulley diameter ratio.

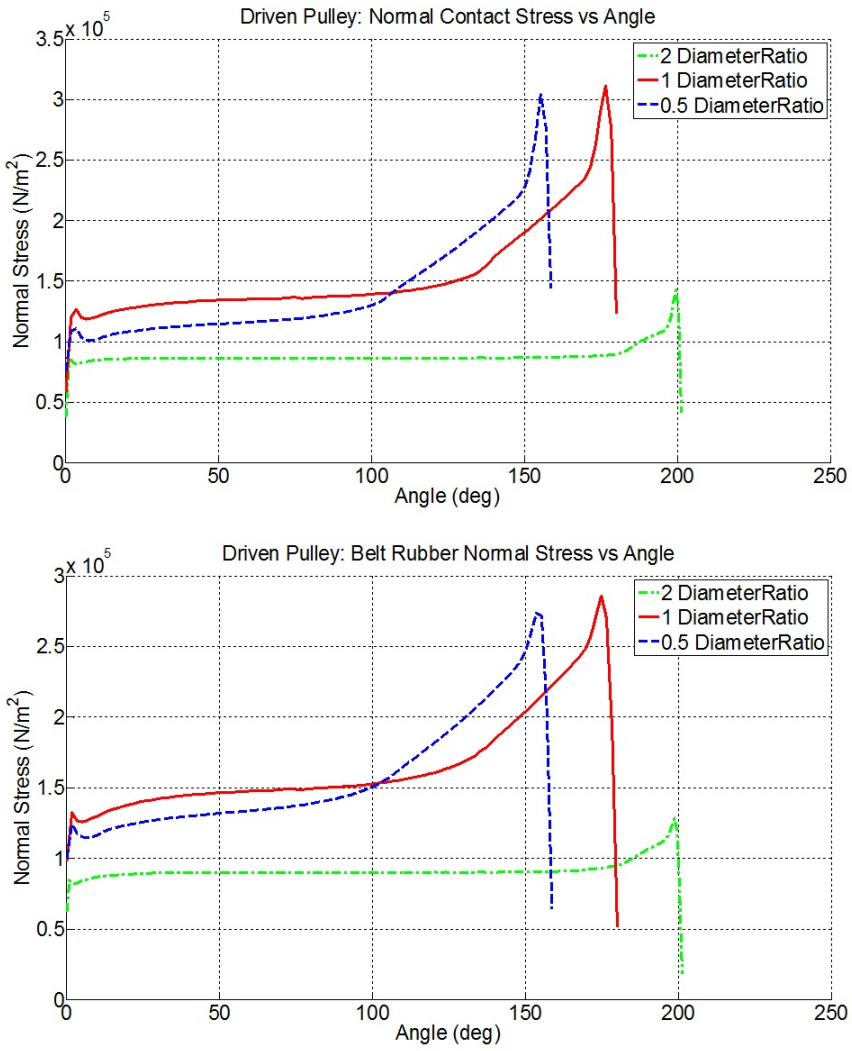

Fig. 4.31. Driven pulley normal contact stress and rubber normal stress as a function of the pulley diameter ratio.

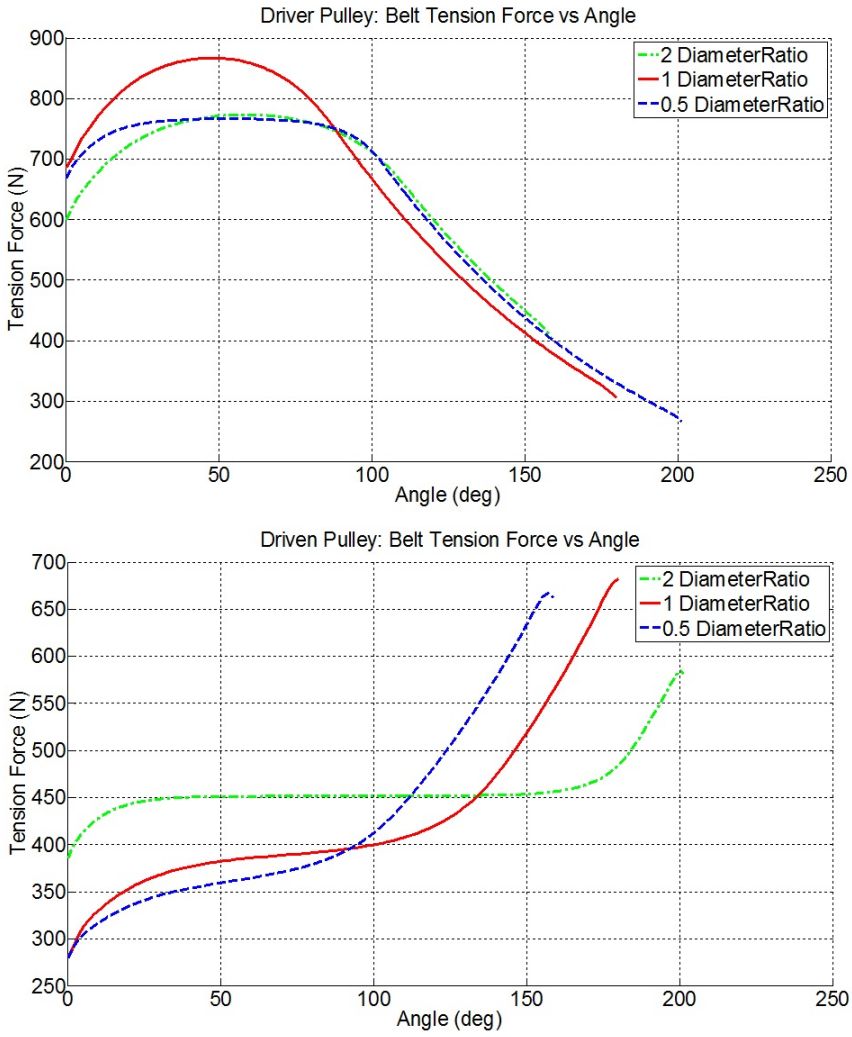

Fig. 4.32. Driver and driven pulleys reinforcements tension force over the pulleys as a function of the pulley diameter ratio.

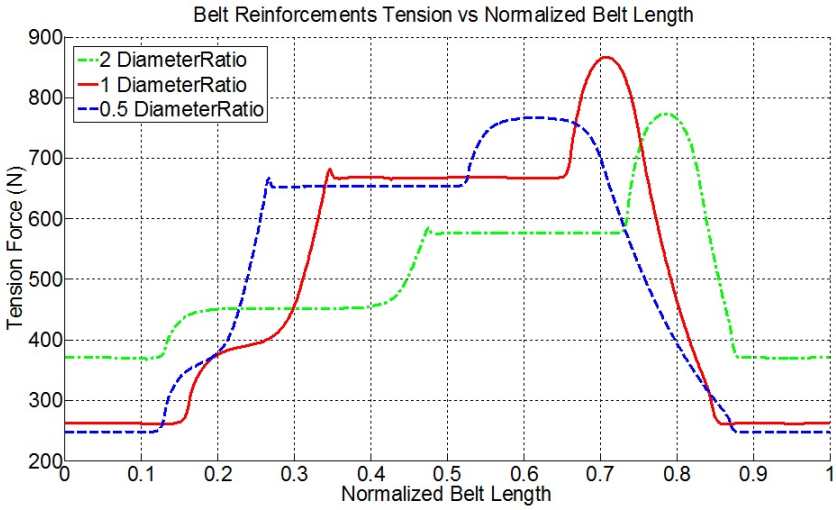

Fig. 4.33. Reinforcements tension force over the belt length as a function of the pulley diameter ratio.

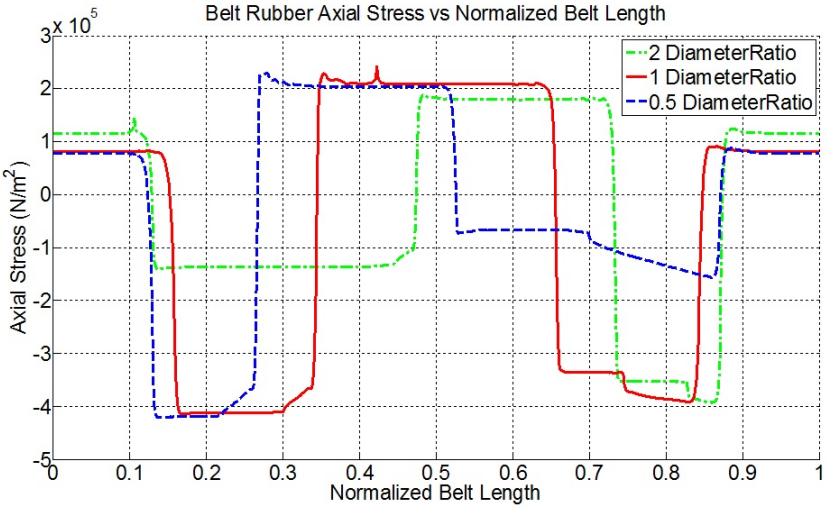

Fig. 4.34. Belt rubber axial stress over the belt length as a function of the pulley diameter ratio.

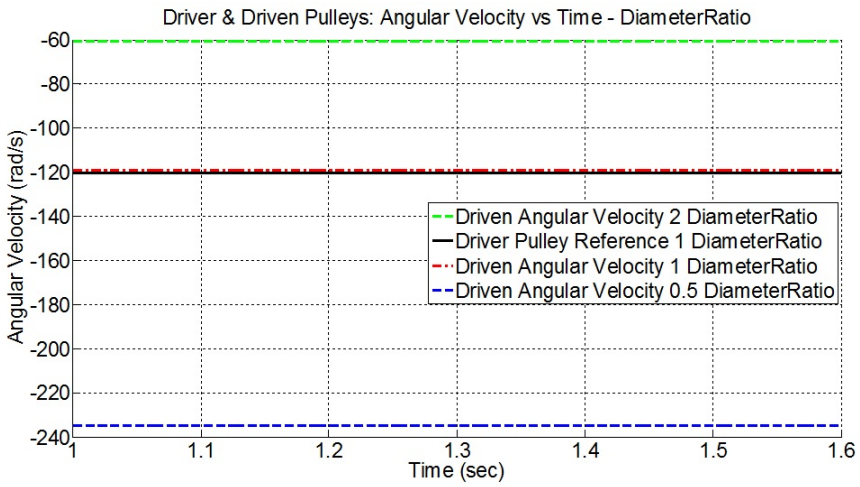

Fig. 4.35. Time-history of the driver and driven pulleys angular velocities as a function of the pulley diameter ratio.

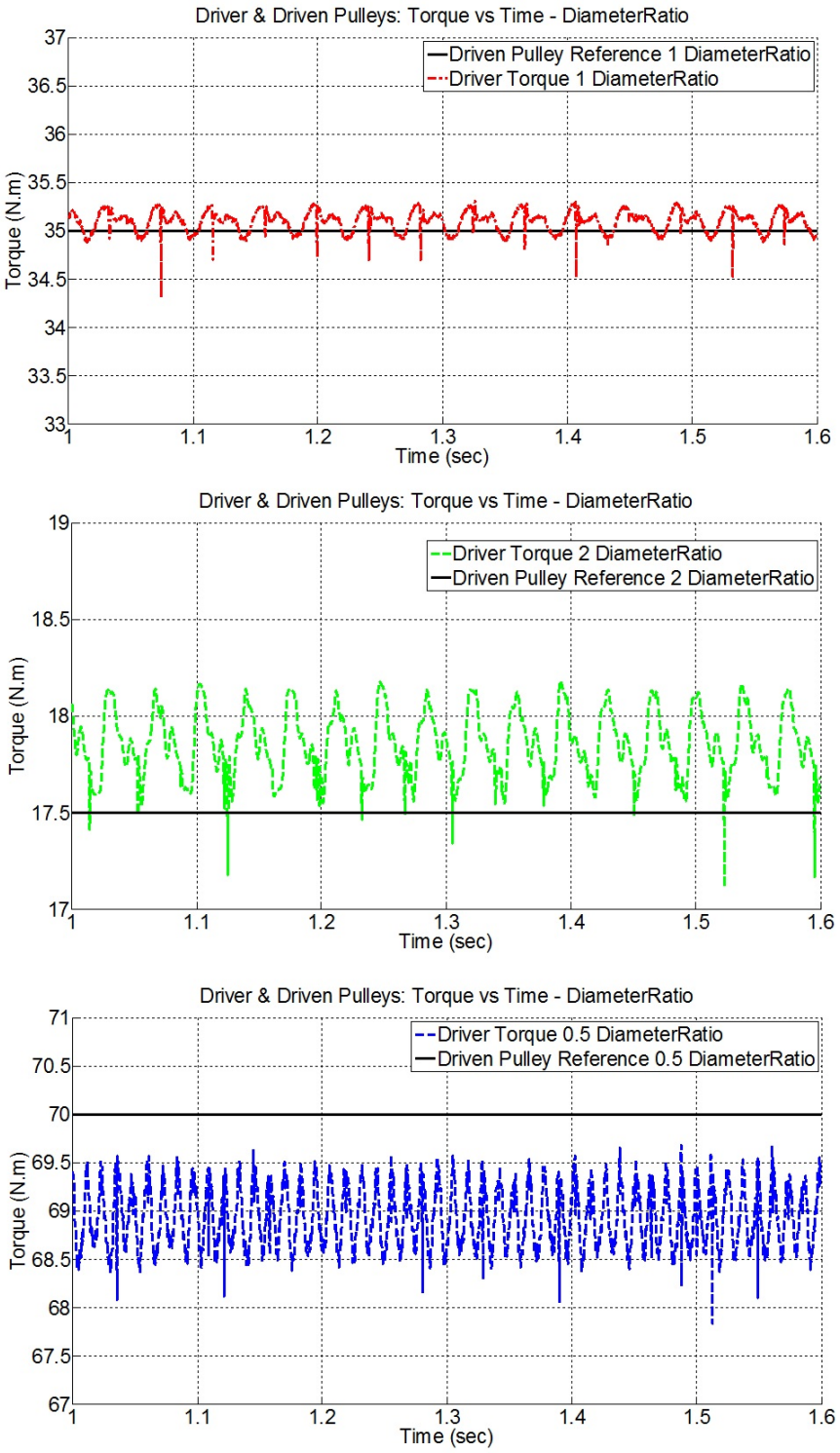

Fig. 4.36. Time-history of the driver applied torque and driven pulley opposing torque as a function of the pulley diameter ratio.

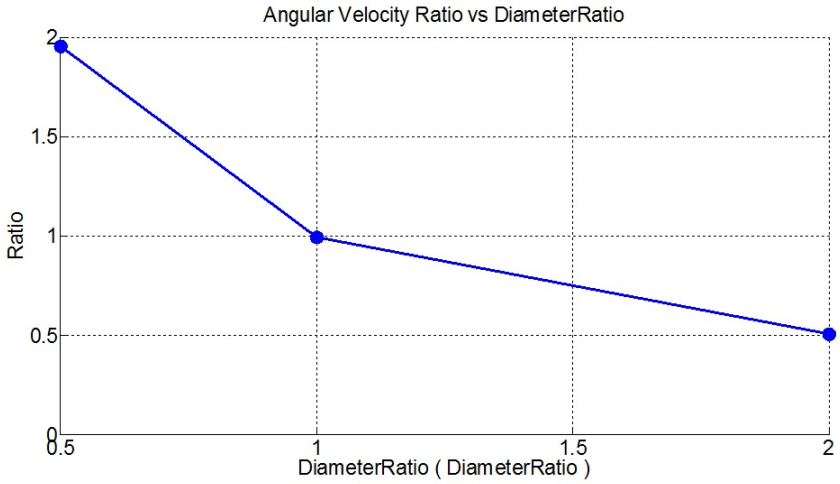

Fig. 4.37. Angular velocity ratio (driven/driver) as a function of the pulley diameter ratio.

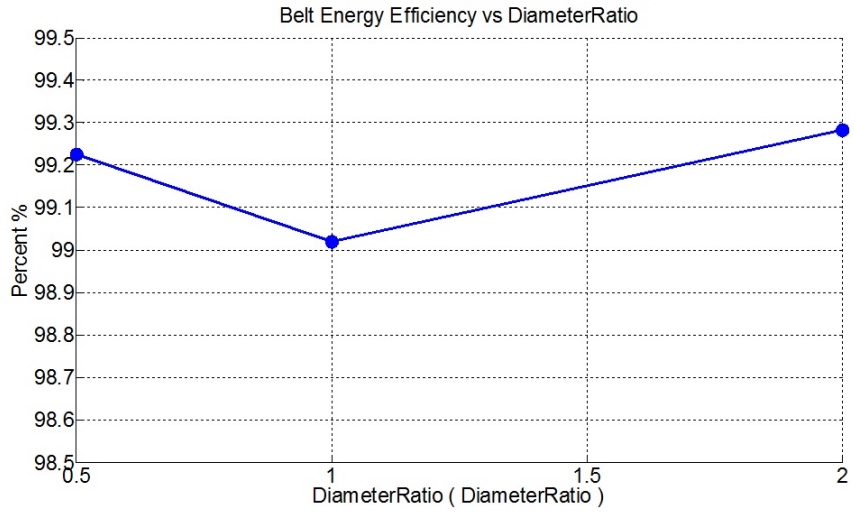

Fig. 4.38. Belt drive energy efficiency as a function of the pulley diameter ratio.

5. EFFECT OF MATERIAL PARAMETERS

5.1 Coefficient of Friction

Figures 5.1 to 5.12 show the effect of the belt-pulley coefficient of friction on the steady-state response of the belt-drive. Figures 5.1 and 5.2 show that the maximum belt-pulley tangential contact stress and the belt rubber shear stress increase with the coefficient of friction. Figure 5.1 shows that the size of the negative traction zone on the driver pulley increases with the coefficient of friction. Figures 5.4 to 5.5 show that the average normal force and belt tension over the driver pulley increase with the coefficient of friction, while the average normal force and belt tension over the driven pulley decrease with the increase of the coefficient of friction. Figure 5.7 shows the belt axial stress over the length of the belt as a function of the coefficient of friction. Figure 5.10 shows the time-history of the driver pulley's applied torque. Figure 5.11 shows that the pulleys' angular velocity ratio decreases with the decrease of the coefficient of friction. Figure 5.12 shows that the belt-drive energy efficiency is nearly unaffected by the coefficient of friction within the range that is tested. Note that this is only true as long as there is no gross slip between the belt and the pulleys.

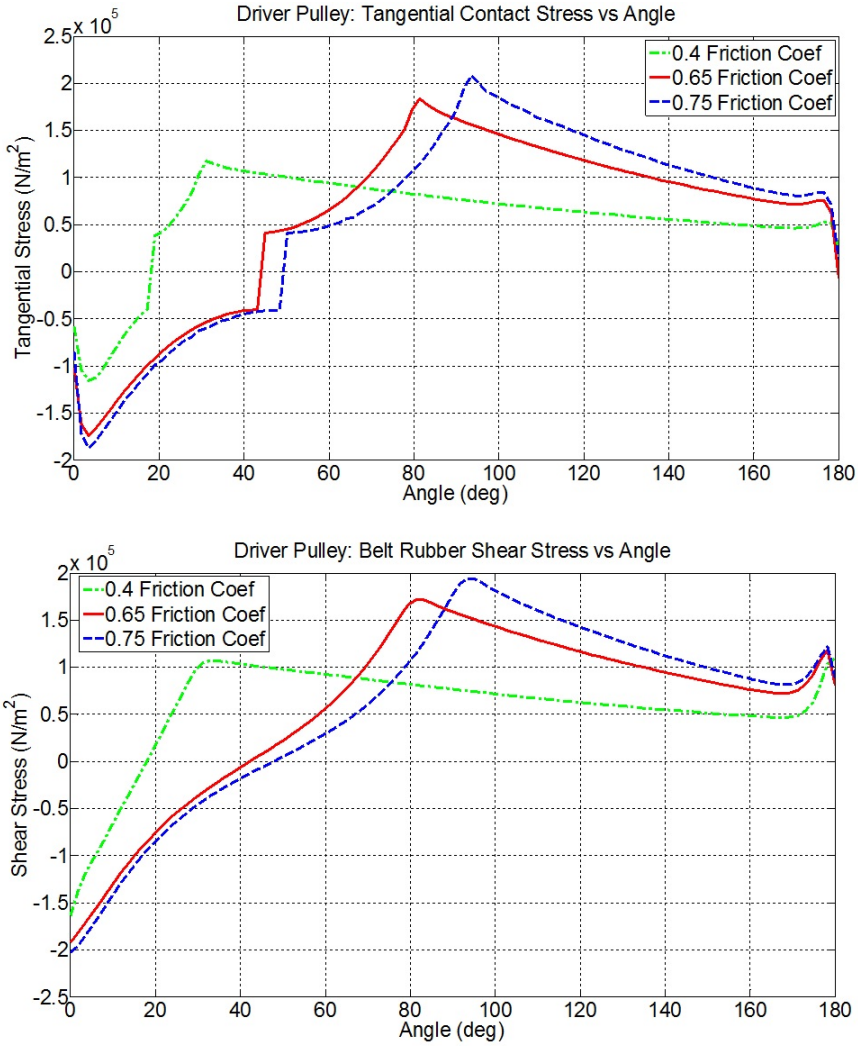

Fig. 5.1. Driver pulley tangential contact stress and rubber shear stress as a function of the coefficient of friction.

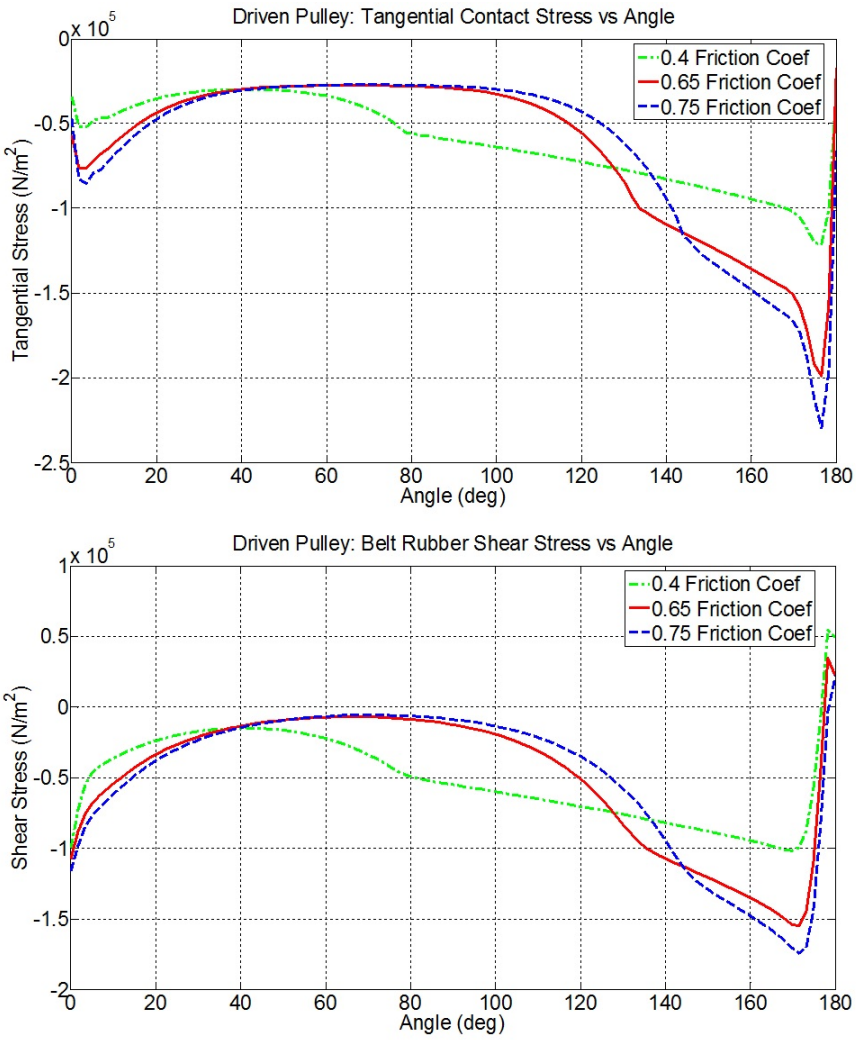

Fig. 5.2. Driven pulley tangential contact stress and rubber shear stress as a function of the coefficient of friction.

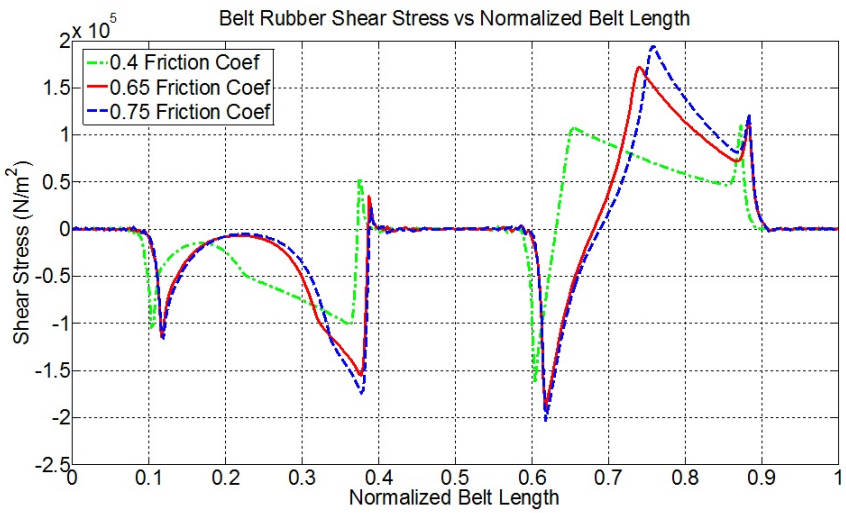

Fig. 5.3. Belt rubber shear stress over the normalized belt length as a function of the coefficient of friction.

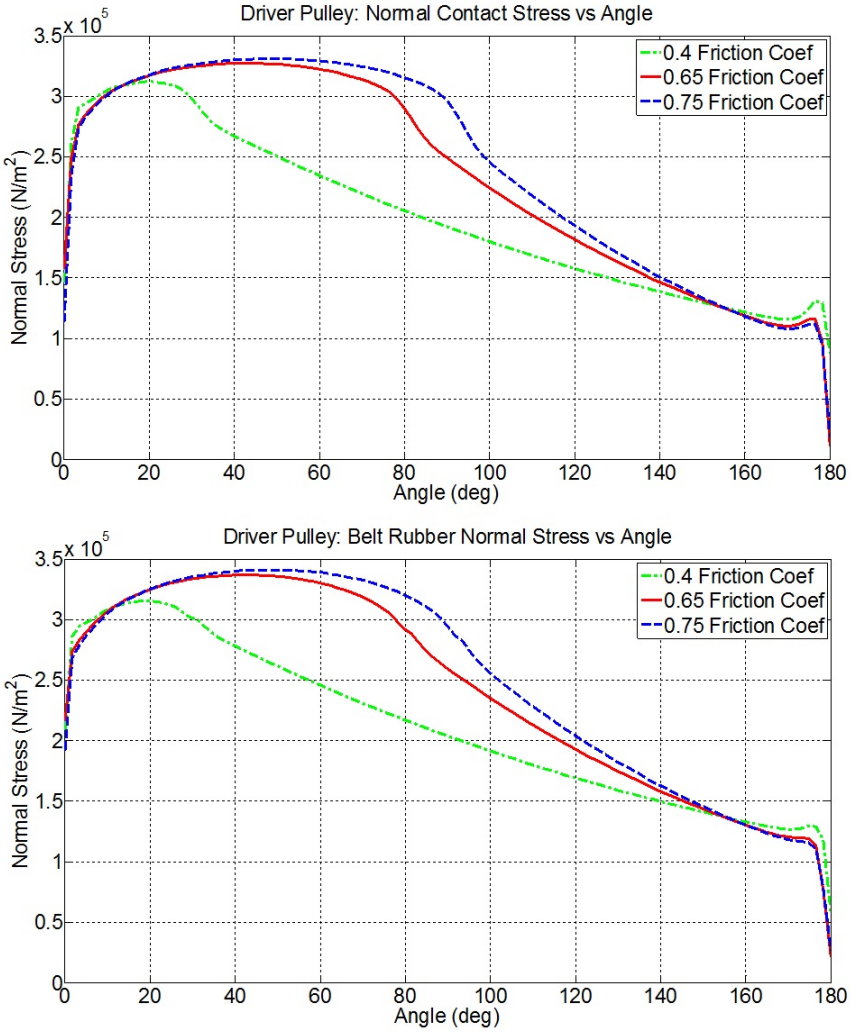

Fig. 5.4. Driver pulley normal contact stress and rubber normal stress as a function of the coefficient of friction.

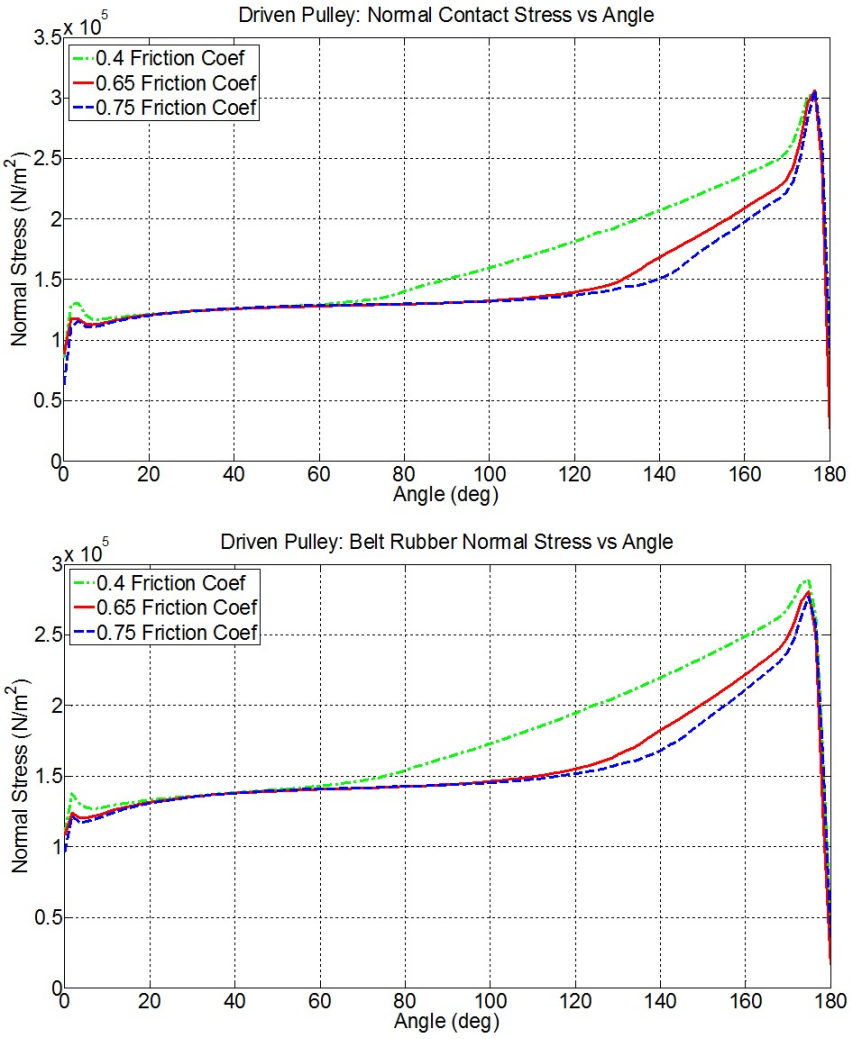

Fig. 5.5. Driven pulley normal contact stress and rubber normal stress as a function of the coefficient of friction.

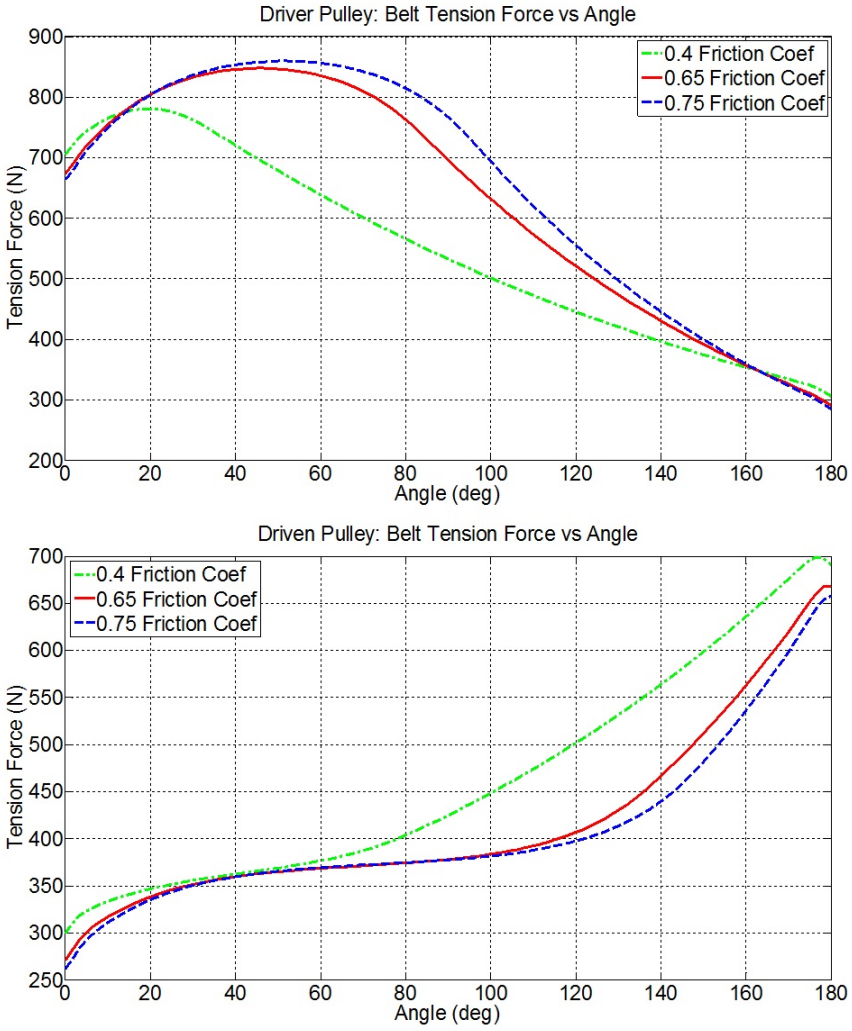

Fig. 5.6. Driver and driven pulleys reinforcements tension force over the pulleys as a function of the coefficient of friction.

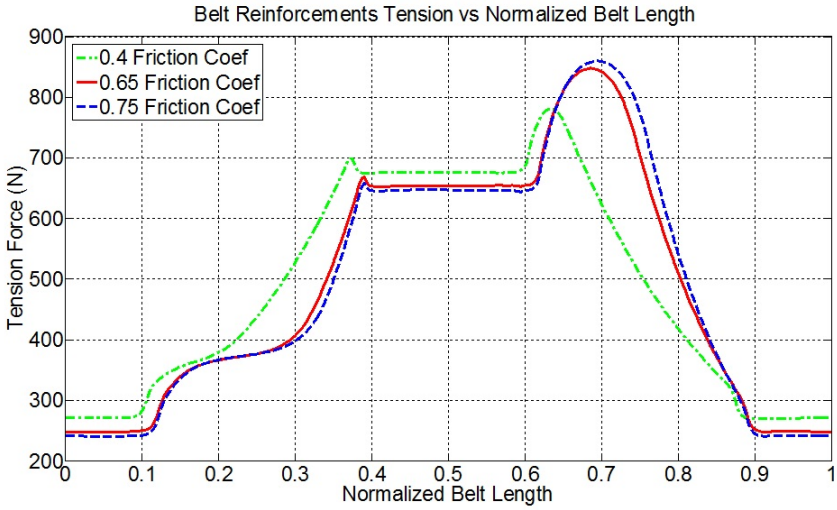

Fig. 5.7. Reinforcements tension force over the belt length as a function of the coefficient of friction.

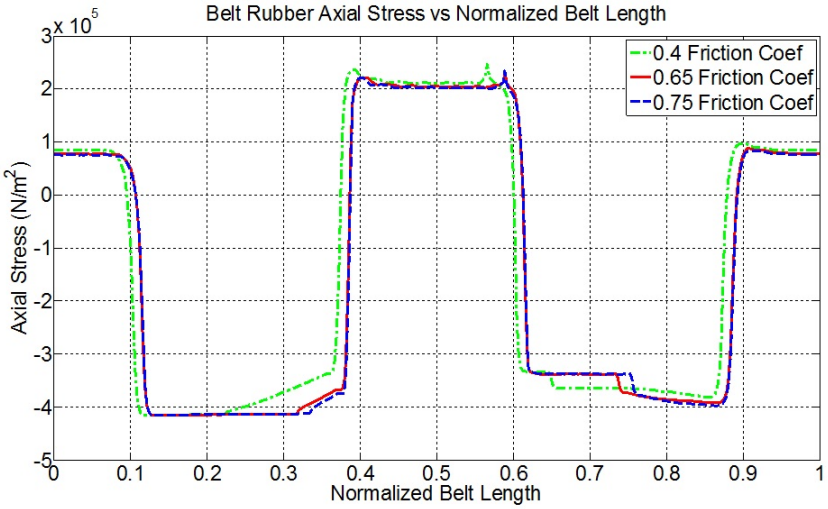

Fig. 5.8. Belt rubber axial stress over the belt length as a function of the coefficient of friction.

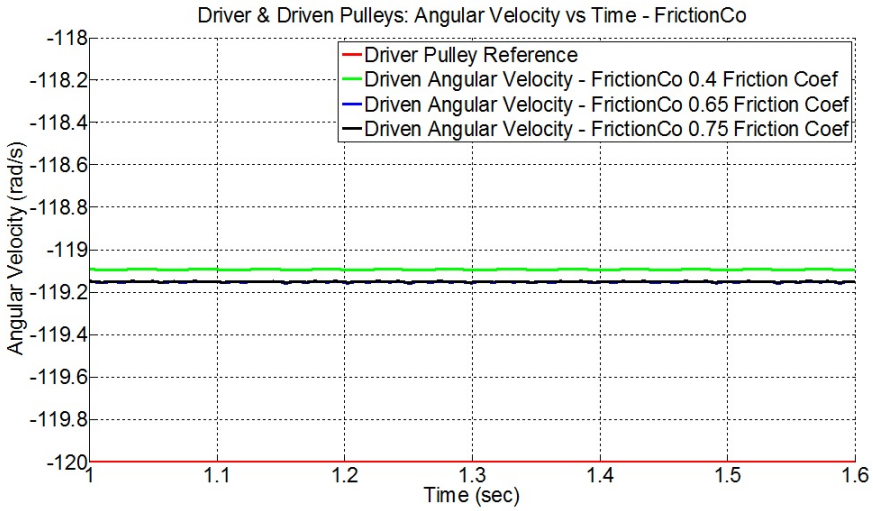

Fig. 5.9. Time-history of the driver and driven pulleys angular velocities as a function of the coefficient of friction.

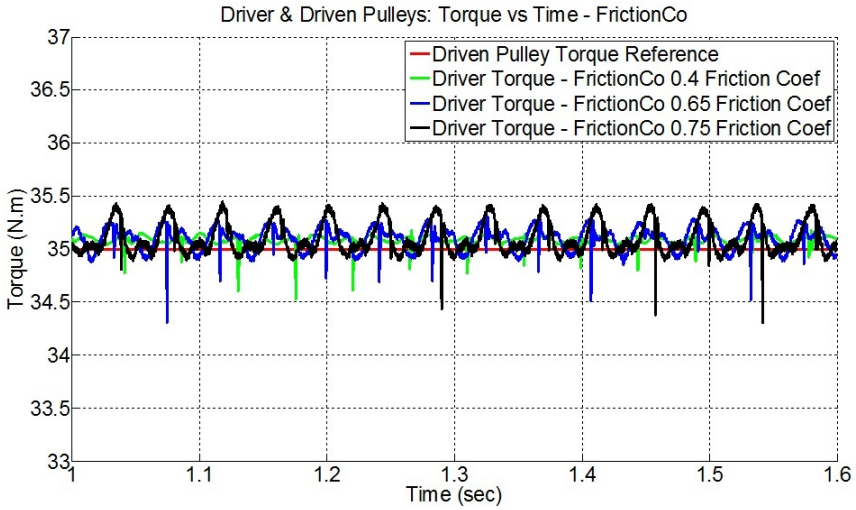

Fig. 5.10. Time-history of the driver applied torque and driven pulley opposiong torque as a function of the coefficient of friction.

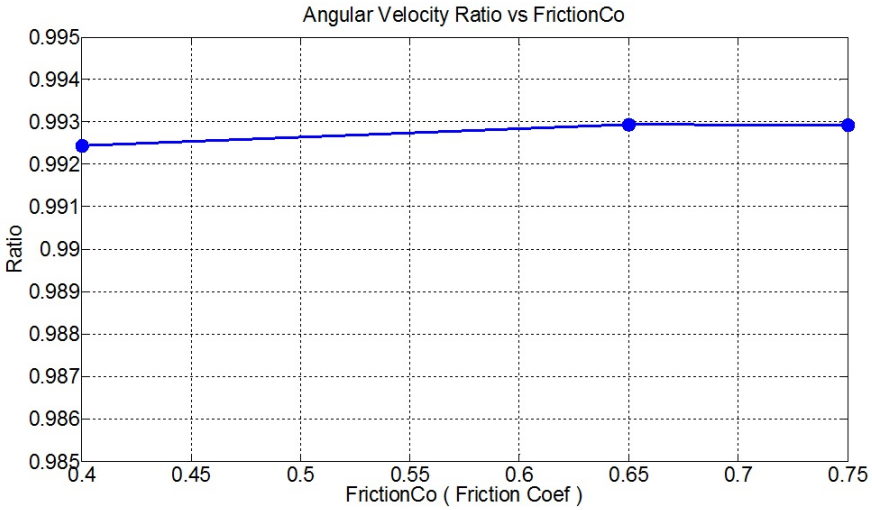

Fig. 5.11. Angular velocity ratio (driven/driver) as a function of the coefficient of friction.

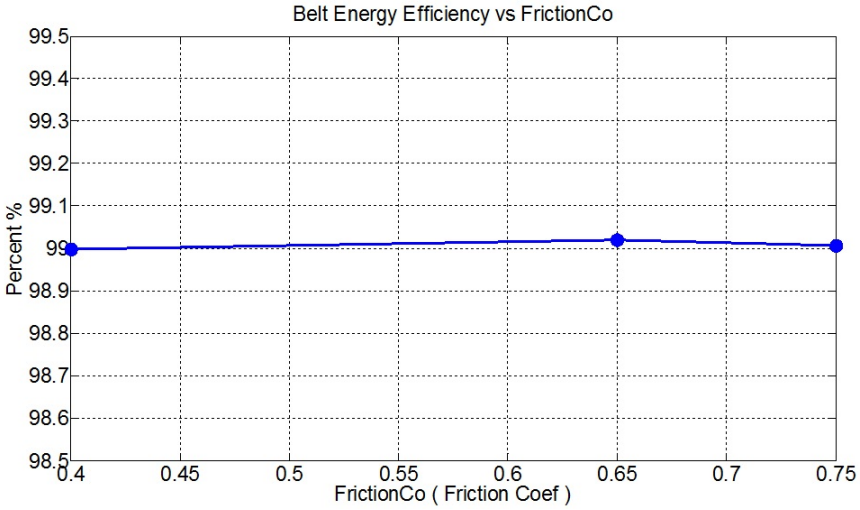

Fig. 5.12. Belt drive energy efficiency as a function of the coefficient of friction.

5.2 Belt Reinforcement Axial Stiffness

Figures 5.13 to 5.24 show the effect of the belt reinforcements' axial stiffness on the steady-state response of the belt-drive. Figures 5.13 shows that the width of the negative traction zone on the driver pulley increases slightly as the belt axial stiffness decreases. Figures 5.16 to 5.18 show that the average normal force and belt tension over the driver pulley increase with the decrease in belt axial stiffness. Also the average normal force and belt tension over the driven pulley increase slightly with the decrease of the belt axial stiffness. Figure 5.20 shows that the belt rubber axial stress decreases over the spans and increases over the pulleys as the belt reinforcements' axial stiffness increases. Figure 5.22 shows that the average magnitude of the stick-slip friction torque pulses increases with the belt's axial stiffness. Figure 5.23 shows that the pulleys' angular velocity ratio increases with the increase of the belt's axial stiffness. Figure 5.24 shows that the belt-drive energy efficiency increases with the belt's axial stiffness.

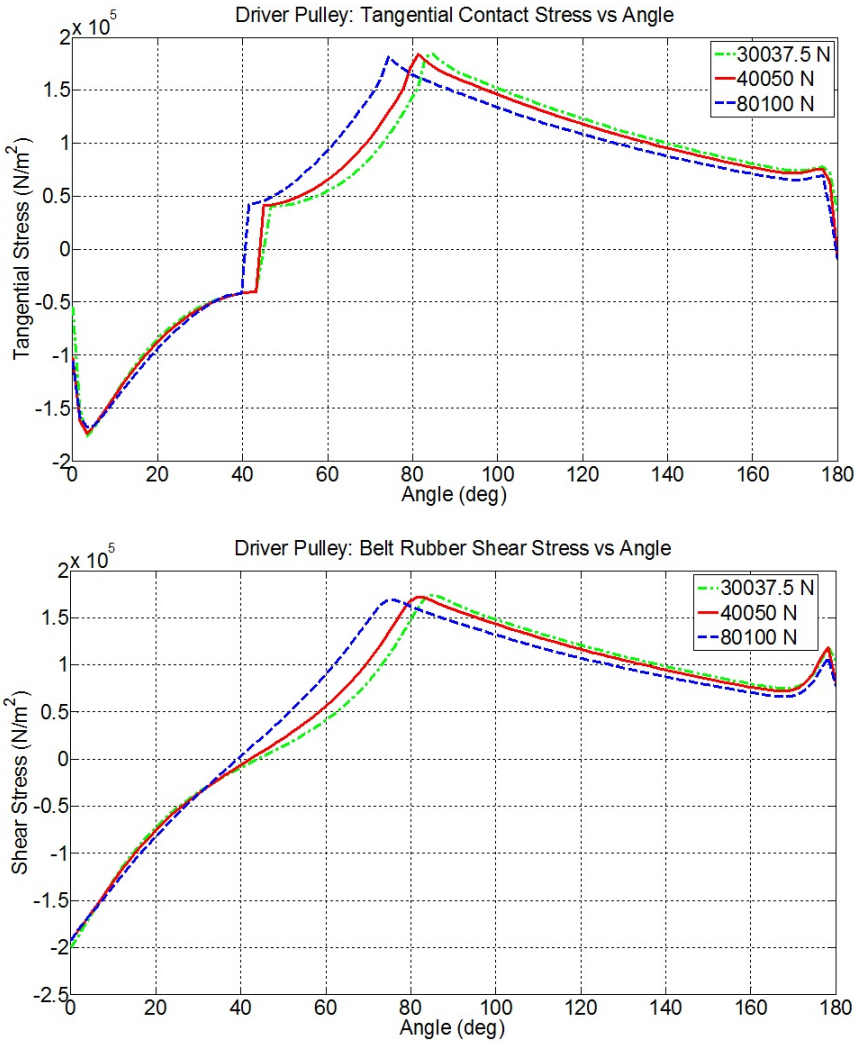

Fig. 5.13. Driver pulley tangential contact stress and rubber shear stress as a function of the belt reinforcements axial stiffness.

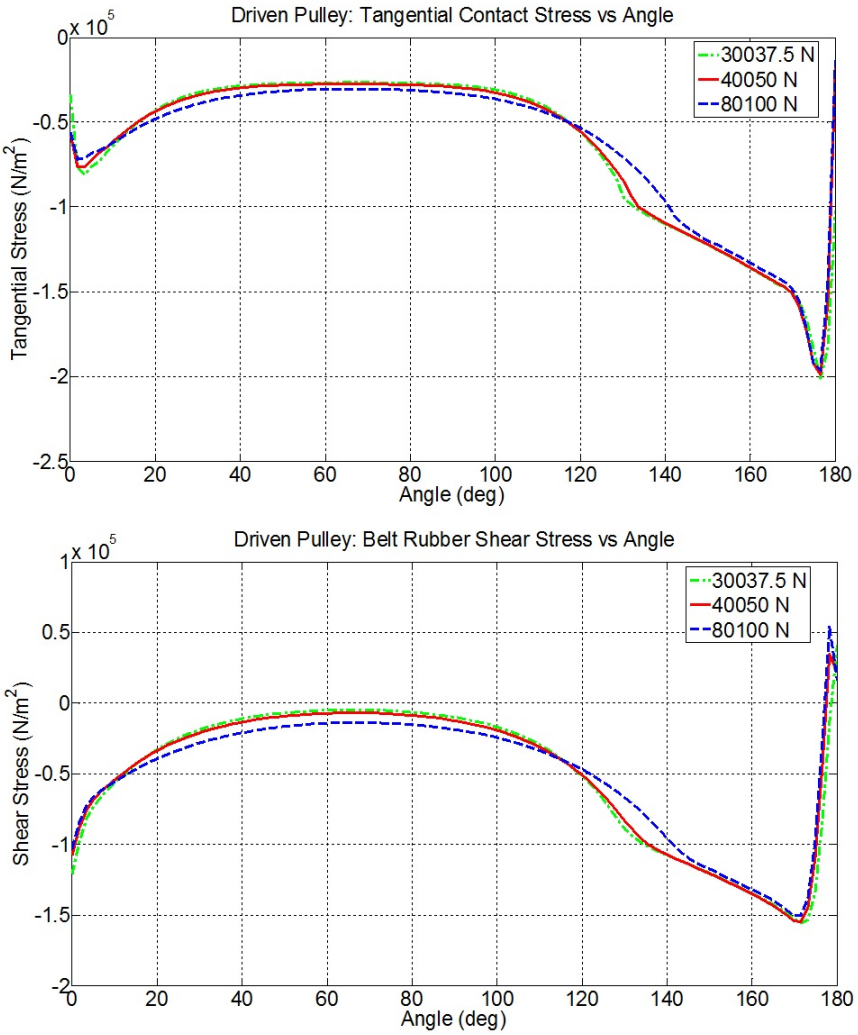

Fig. 5.14. Driven pulley tangential contact stress and rubber shear stress as a function of the belt reinforcements axial stiffness.

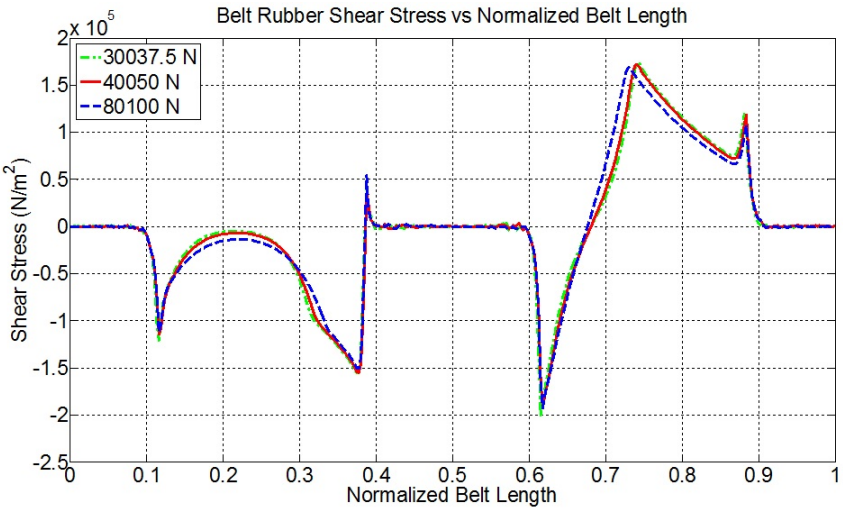

Fig. 5.15. Belt rubber shear stress over the normalized belt length as a function of the belt reinforcements axial stiffness.

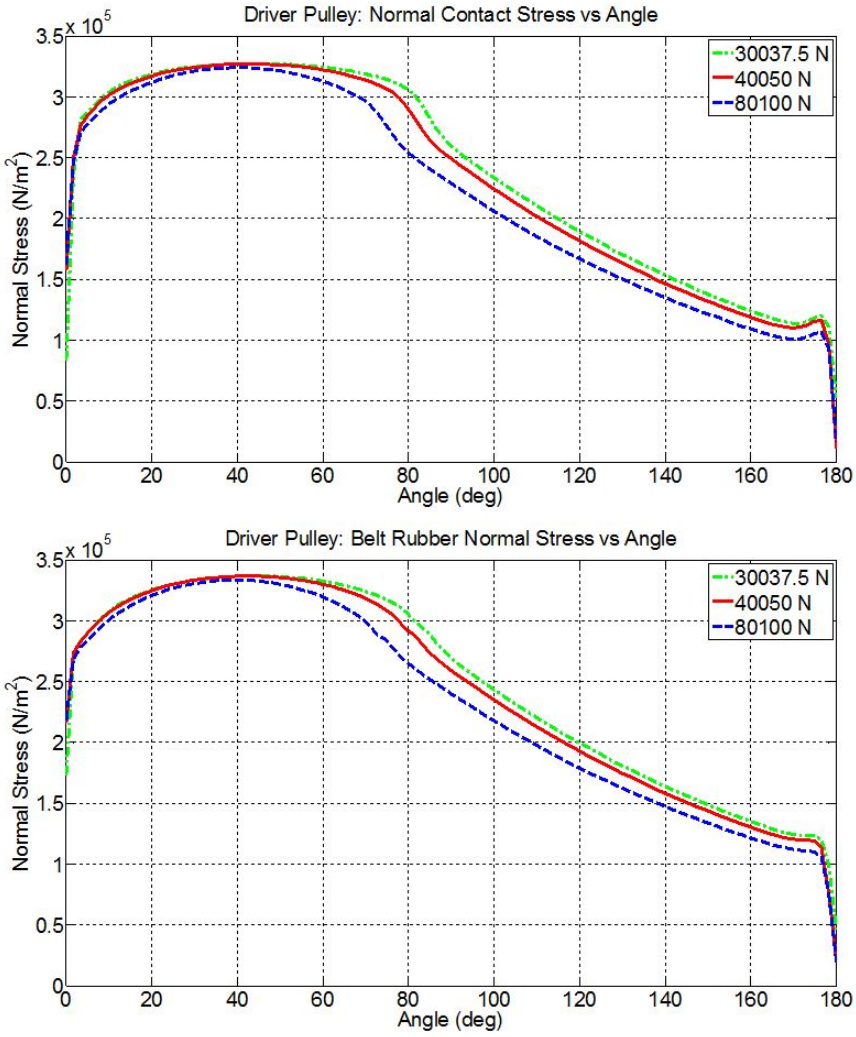

Fig. 5.16. Driver pulley normal contact stress and rubber normal stress as a function of the belt reinforcements axial stiffness.

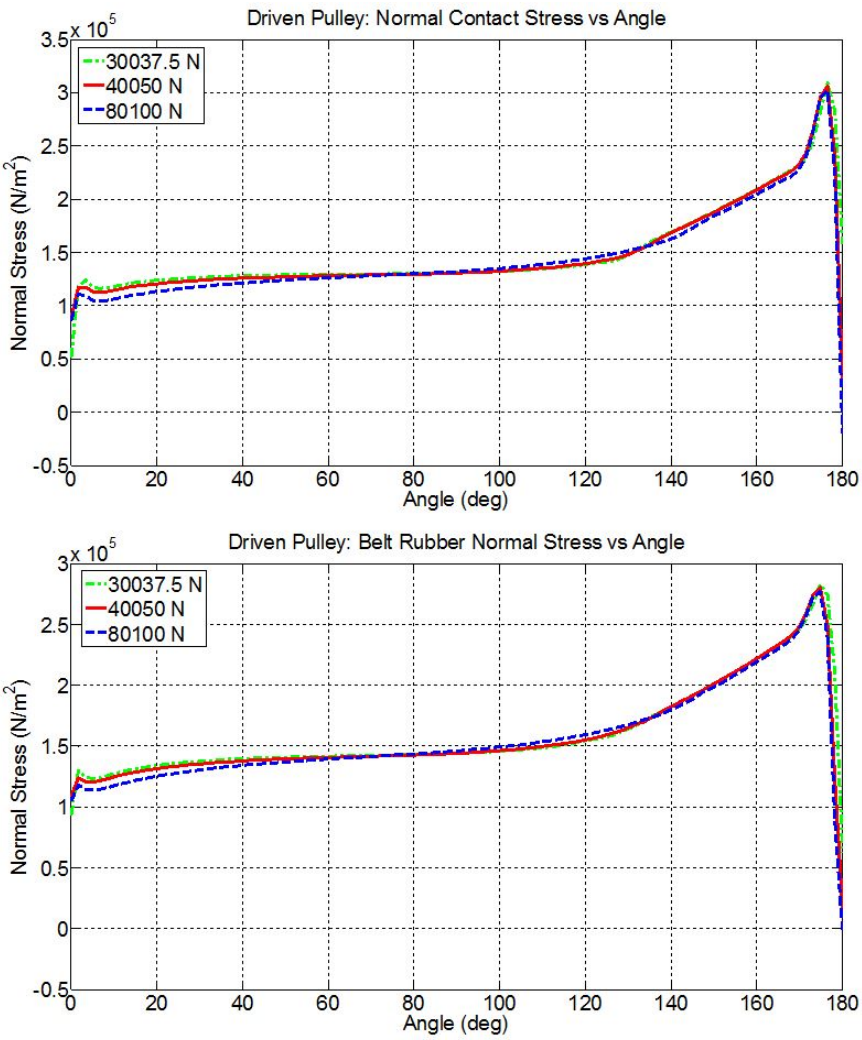

Fig. 5.17. Driven pulley normal contact stress and rubber normal stress as a function of the belt reinforcements axial stiffness.

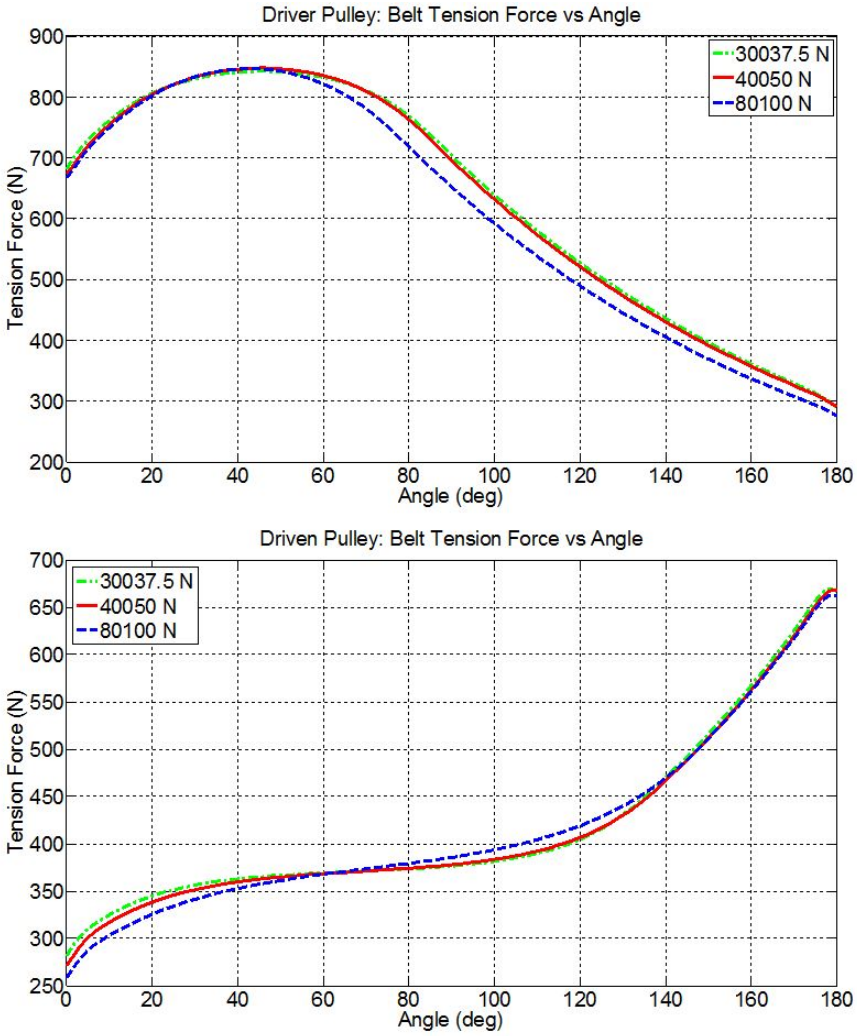

Fig. 5.18. Driver and driven pulleys reinforcements tension force over the pulleys as a function of the belt reinforcements axial stiffness.

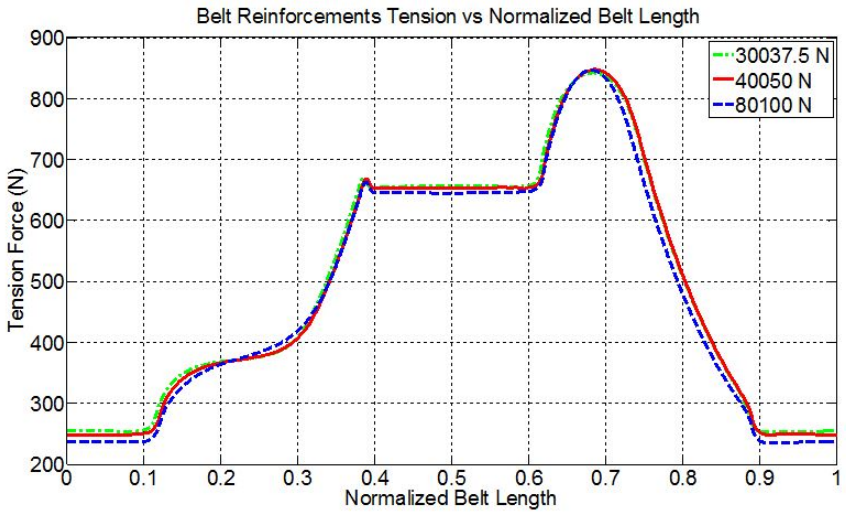

Fig. 5.19. Reinforcements tension force over the belt length as a function of the belt reinforcements axial stiffness.

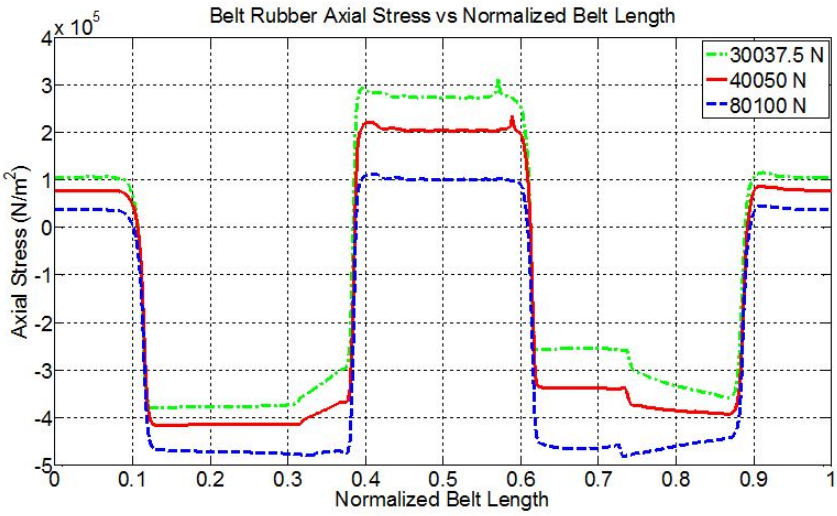

Fig. 5.20. Belt rubber axial stress over the belt length as a function of the belt reinforcements axial stiffness.

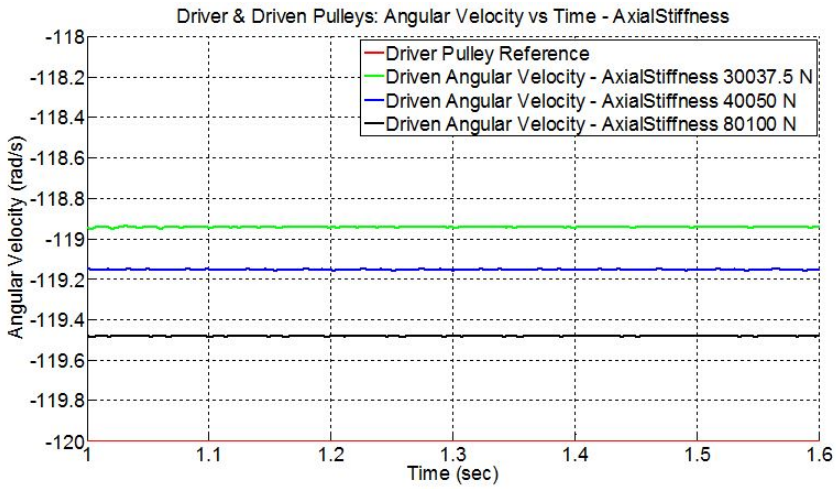

Fig. 5.21. Time-history of the driver and driven pulleys angular velocities as a function of the belt reinforcements axial stiffness.

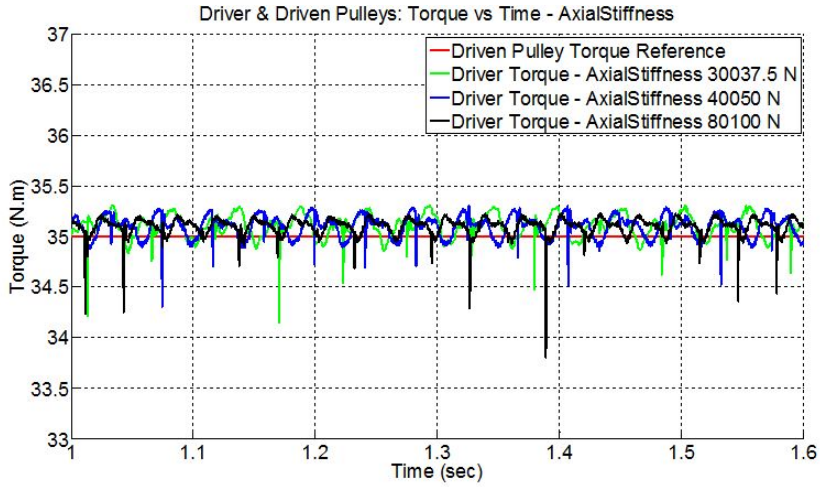

Fig. 5.22. Time-history of the driver applied torque and driven pulley opposing torque as a function of the coefficient of friction.

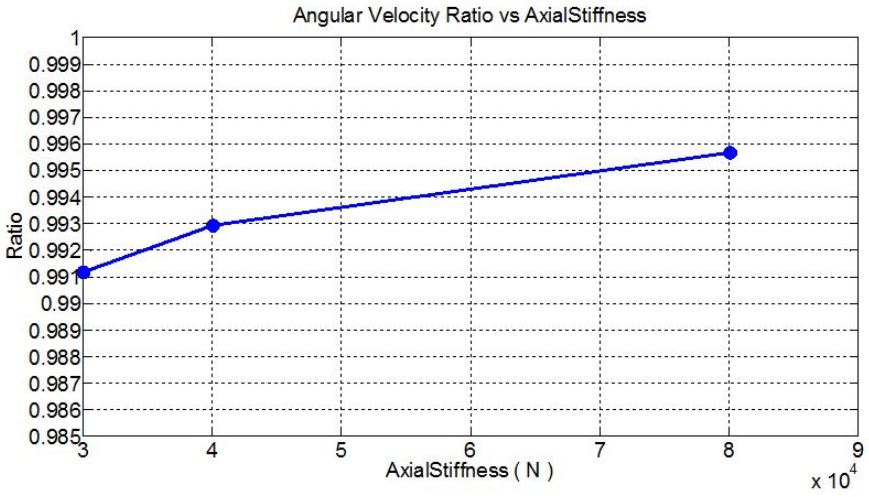

Fig. 5.23. Angular velocity ratio (driven/driver) as a function of the belt reinforcements axial stiffness.

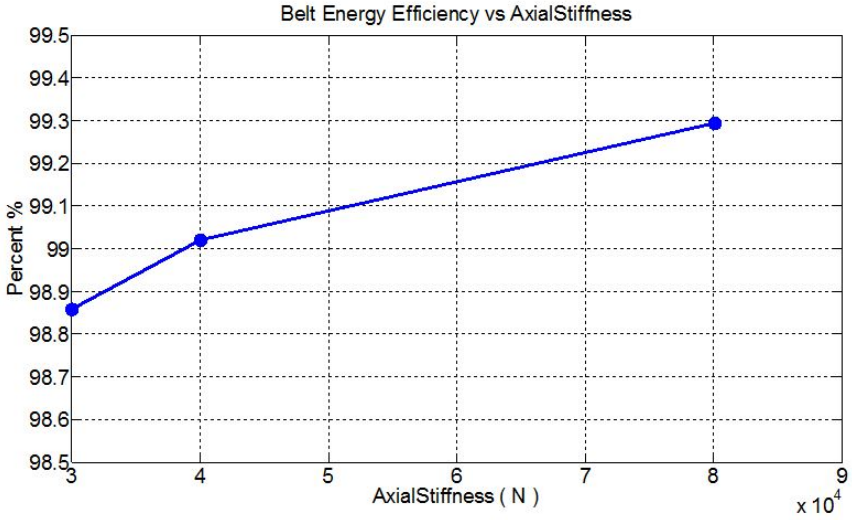

Fig. 5.24. Belt drive energy efficiency as a function of the belt reinforcements axial stiffness.

5.3 Belt Reinforcement Axial Damping

Figures 5.25 to 5.28 show that the belt reinforcements' axial damping has negligible effect on the steady-state response of the belt-drive. This is expected since the change in linear velocity of the belt is small because the belt-drive is operating at a constant speed. The belt's axial damping is expected to be important if there are oscillations in the pulleys' angular velocities.

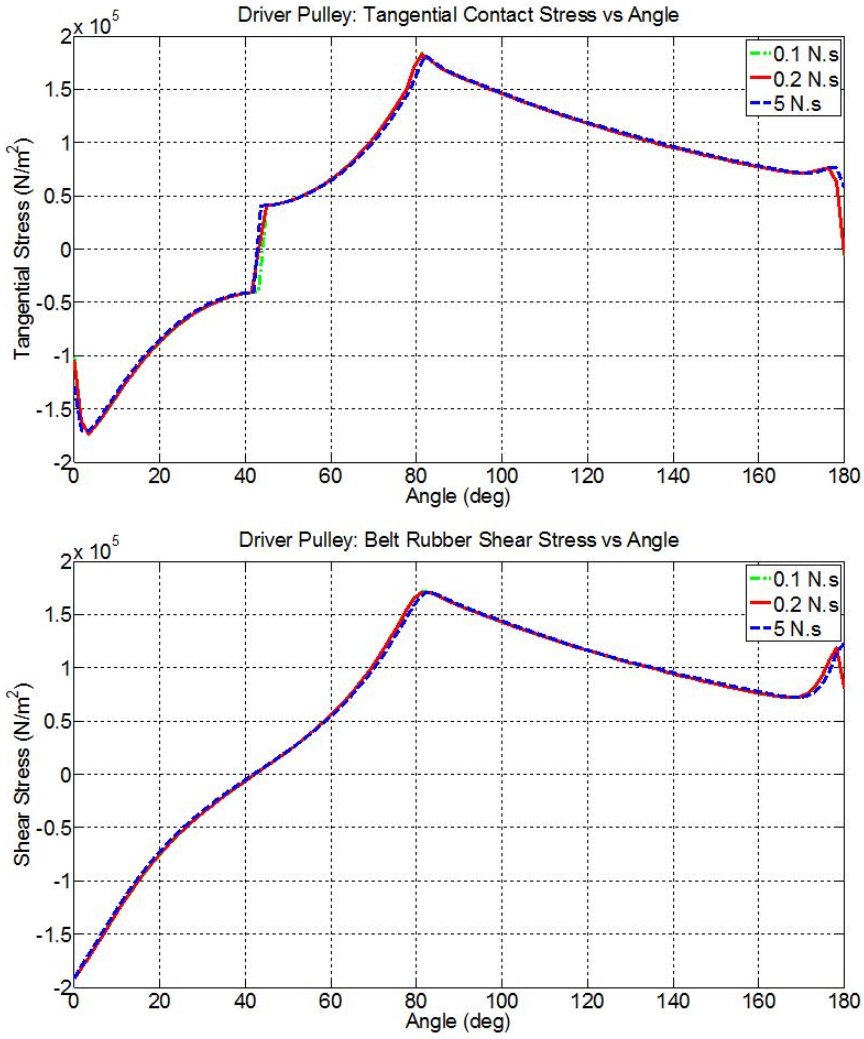

Fig. 5.25. Driver pulley tangential contact stress and rubber shear stress as a function of the belt reinforcements axial damping.

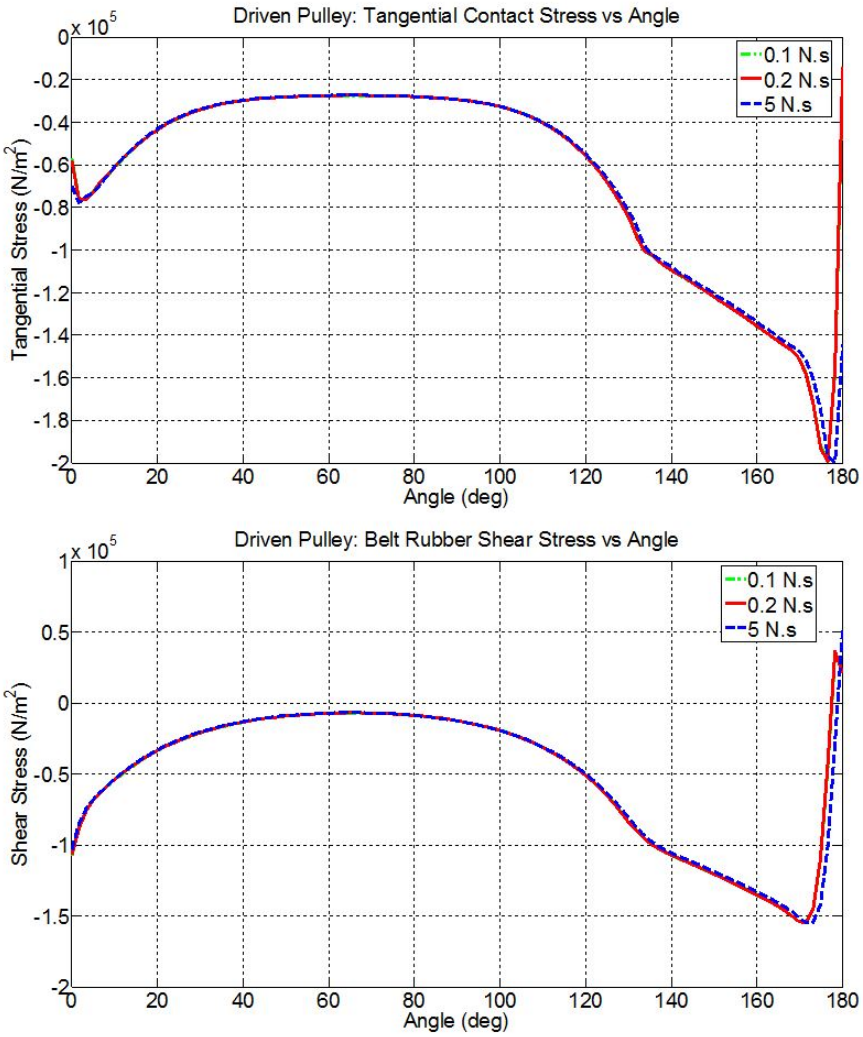

Fig. 5.26. Driven pulley tangential contact stress and rubber shear stress as a function of the belt reinforcements axial damping.

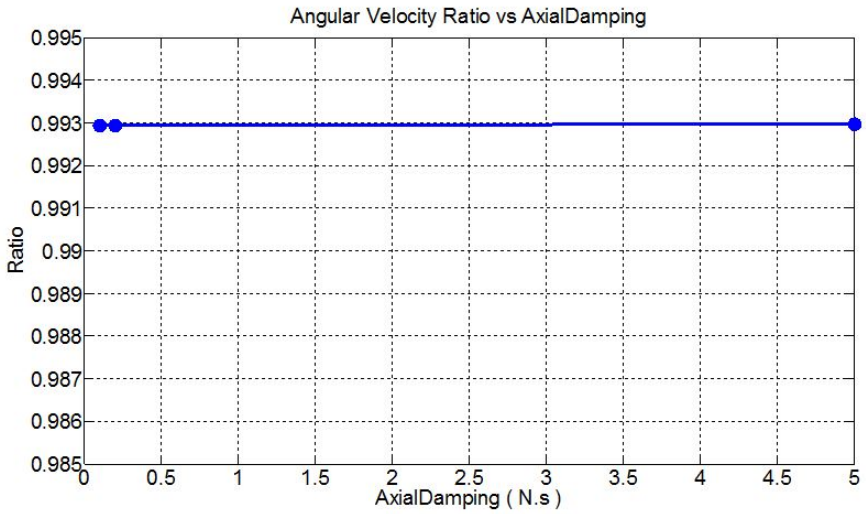

Fig. 5.27. Angular velocity ratio (driven/driver) as a function of the belt reinforcements axial damping.

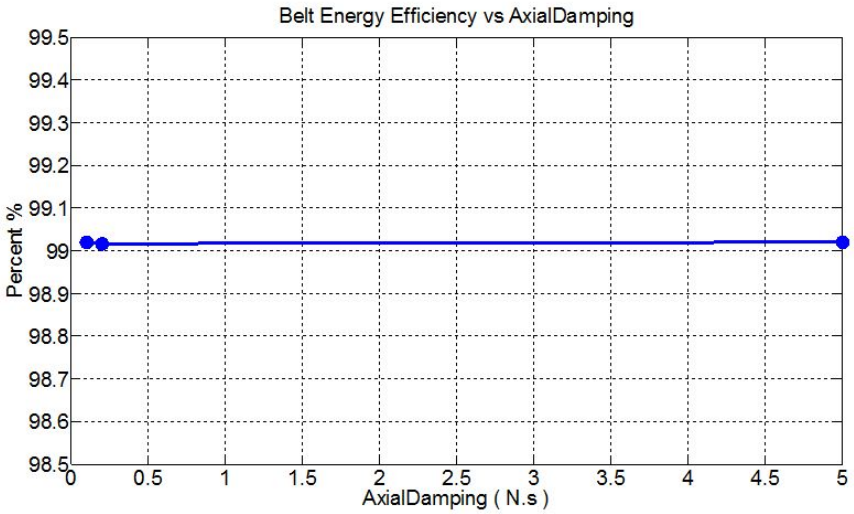

Fig. 5.28. Belt drive energy efficiency as a function of the belt reinforcements axial damping.

5.4 Belt Reinforcement Bending Stiffness

Figures 5.29 to 5.40 show the effect of the bending stiffness on the steady-state response of the belt-drive. Figures 5.29 and 5.30 show that the bending stiffness changes the wrap angle of the belt on the pulley. As the belt bending stiffness increases, the contact angle on the pulley decreases. The increased bending stiffness results in a larger tangential contact and rubber shear stresses at the entrance and exit of both driver and driven pulleys. Figure 5.32 shows the effect on driver pulley for the normal contact stress and belt rubber normal stress. The maximum normal stress increases in both slip zones as the bending stiffness increases. The same phenomenon of increased normal stress at the belt rubber as well as at the contact right before exiting the driver pulley can be seen as it was seen in tangential stress. Figure 5.33 shows that the same phenomenon occurs for the driven pulley as well. Figure 5.34 and 5.35 show that the tension increases along the belt length as the bending stiffness increases. Figure 5.37 shows the variation in driven pulley angular velocity ratio with change in belt reinforcements. As the stiffness is increased, the driven pulley angular velocity slightly increases. Figure 5.38 shows the torque on the driver pulley against time. Smaller spikes are observed as the bending stiffness increases. Figures 5.39 and 5.40 show that although increased bending stiffness results in higher angular velocity ratios, overall belt energy efficiency drops due to reduced torque transfer.

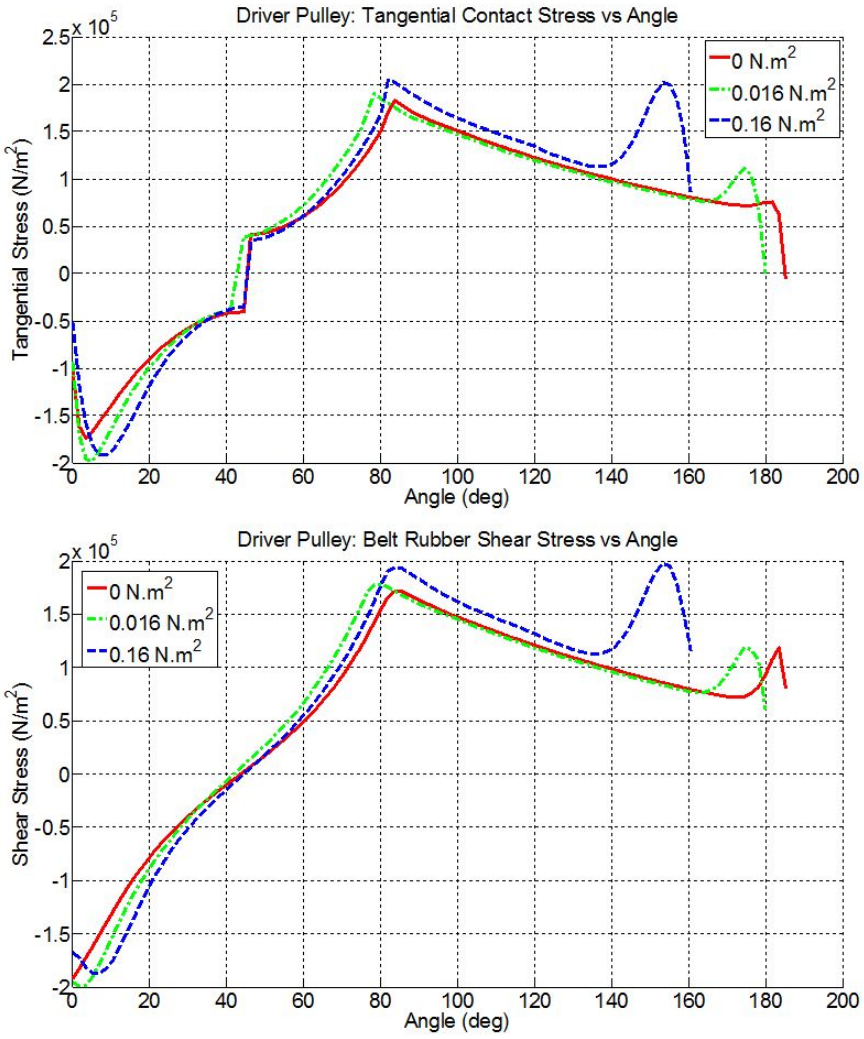

Fig. 5.29. Driver pulley tangential contact stress and rubber shear stress as a function of the belt reinforcements bending stiffness.

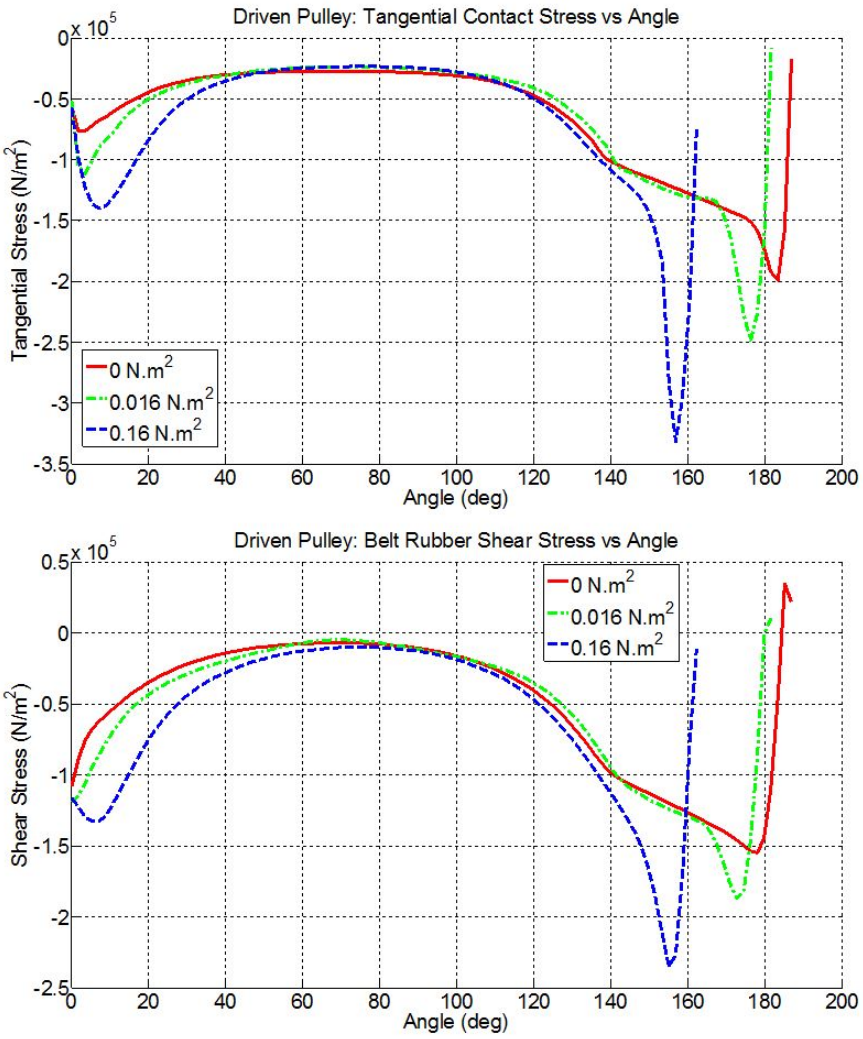

Fig. 5.30. Driven pulley tangential contact stress and rubber shear stress as a function of the belt reinforcements bending stiffness.

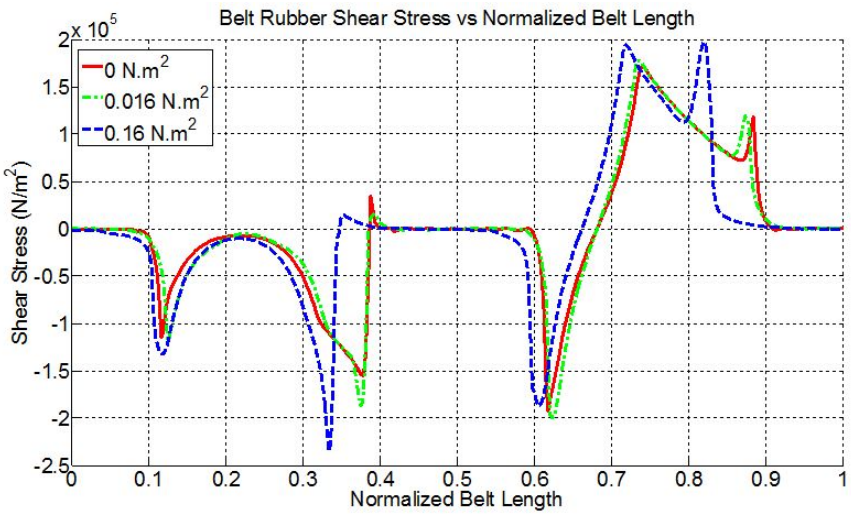

Fig. 5.31. Belt rubber shear stress over the normalized belt length as a function of the belt reinforcements bending stiffness.

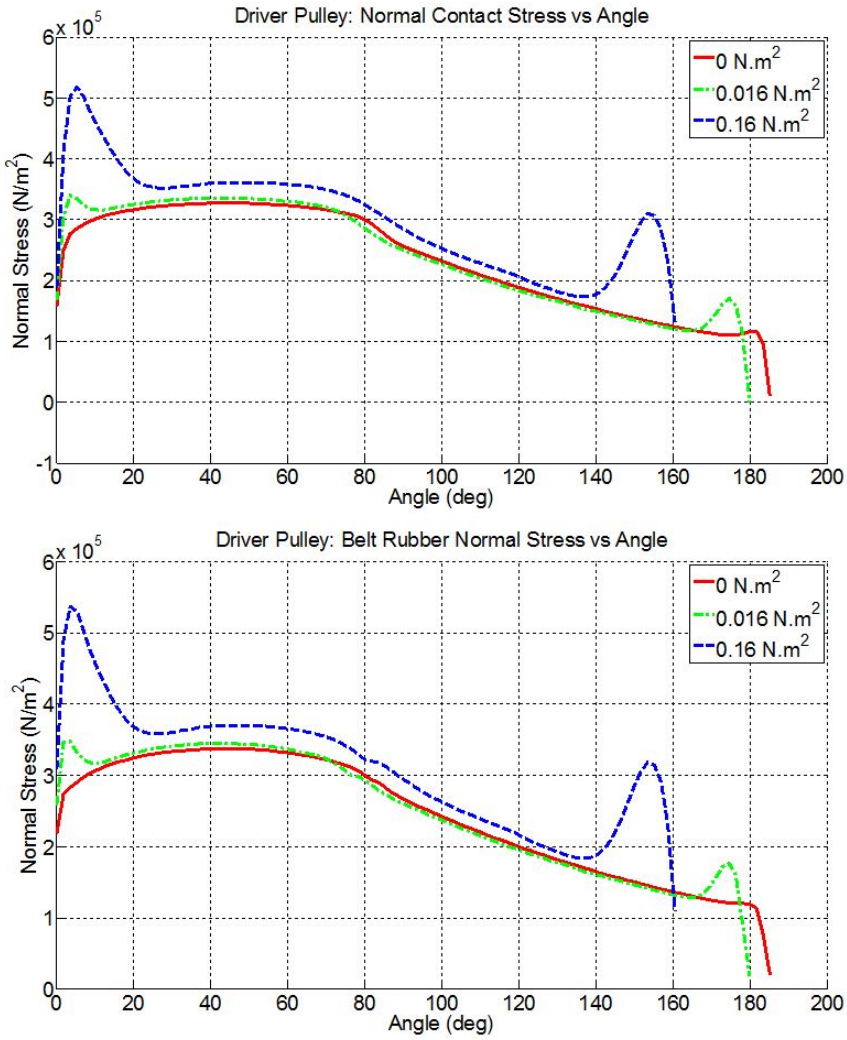

Fig. 5.32. Driver pulley normal contact stress and rubber normal stress as a function of the belt reinforcements bending stiffness.

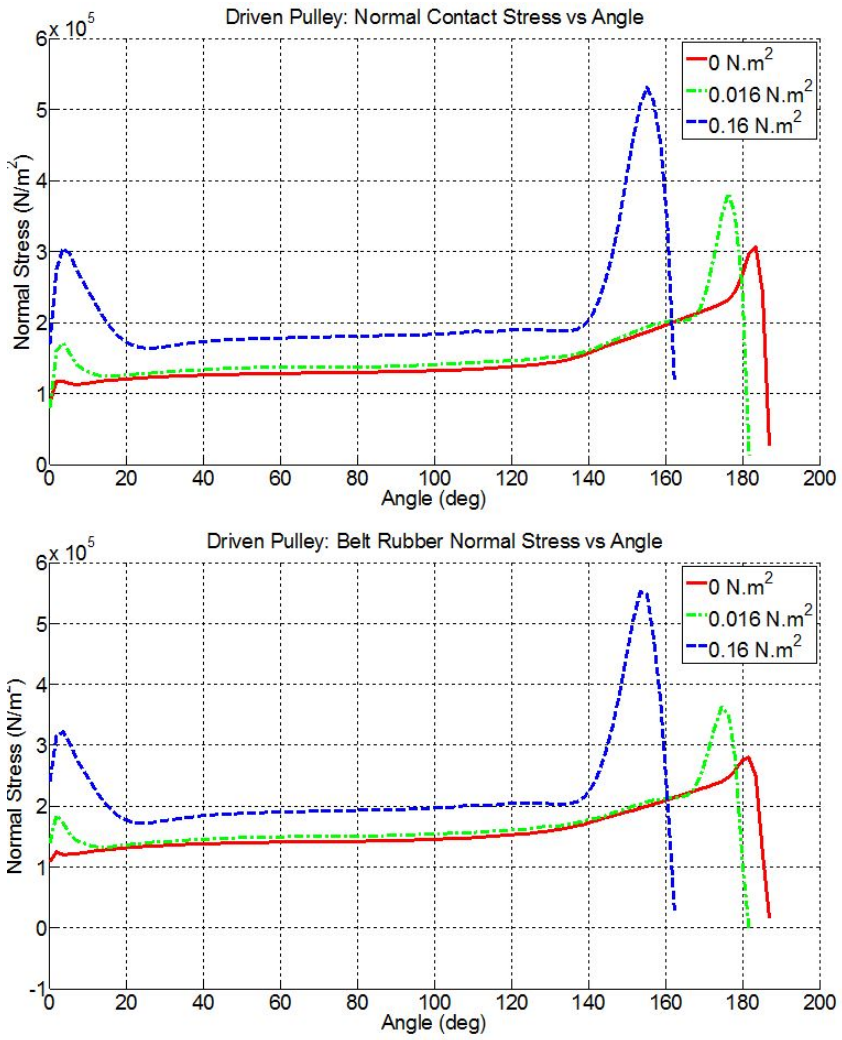

Fig. 5.33. Driven pulley normal contact stress and rubber normal stress as a function of the belt reinforcements bending stiffness.

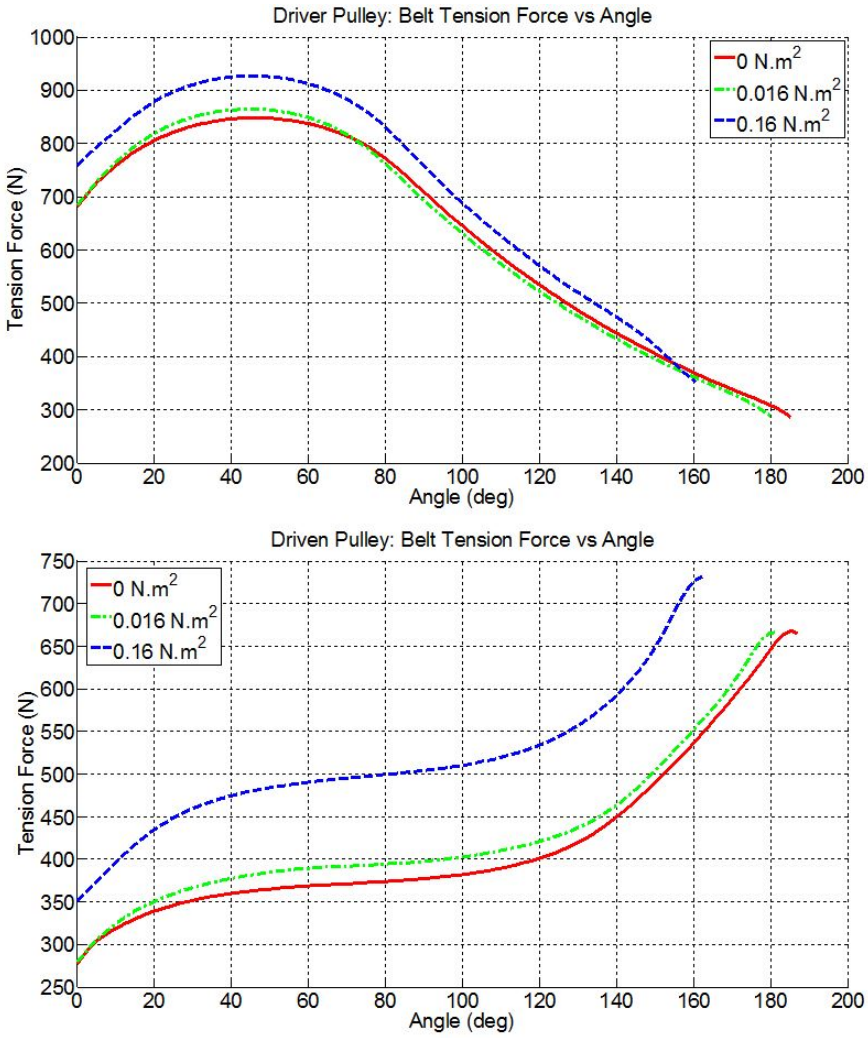

Fig. 5.34. Driver and driven pulleys reinforcements tension force over the pulleys as a function of the belt reinforcements bending stiffness.

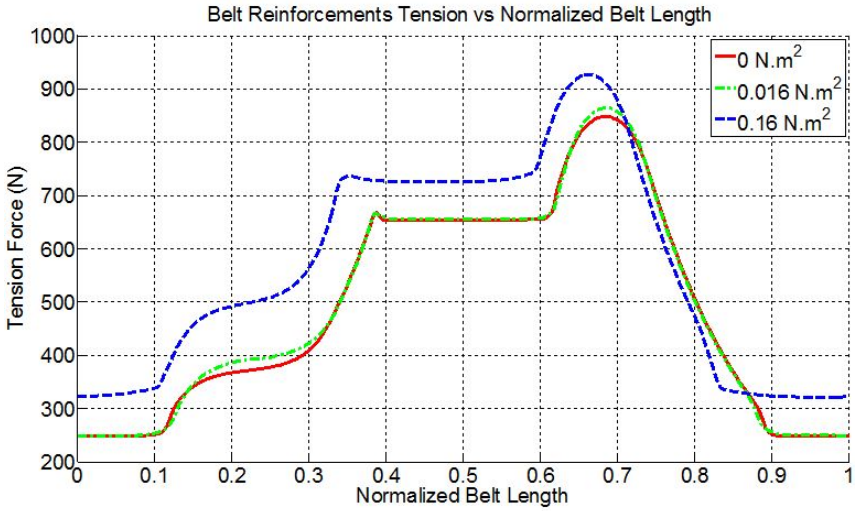

Fig. 5.35. Reinforcements tension force over the belt length as a function of the coefficient of friction.

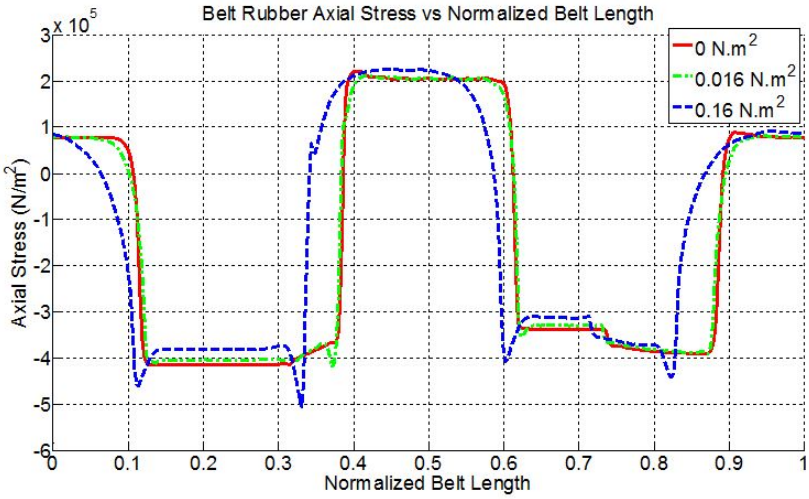

Fig. 5.36. Belt rubber axial stress over the belt length as a function of the belt reinforcements bending stiffness.

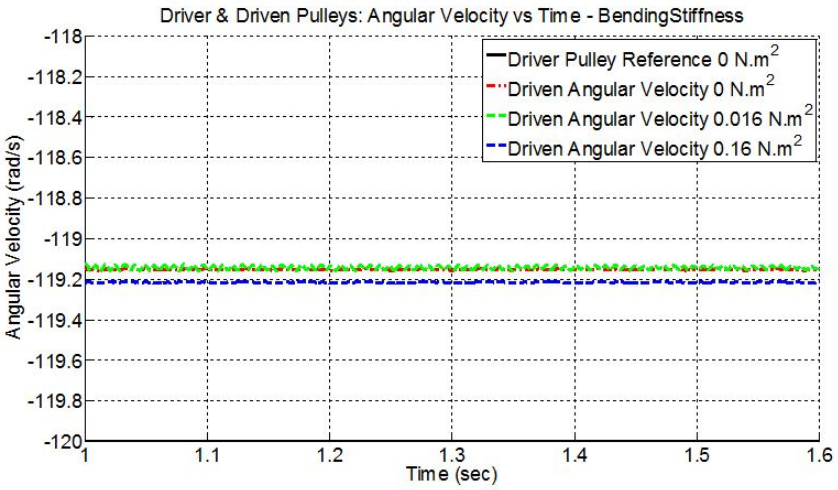

Fig. 5.37. Time-history of the driver and driven pulleys angular velocities as a function of the belt reinforcements bending stiffness.

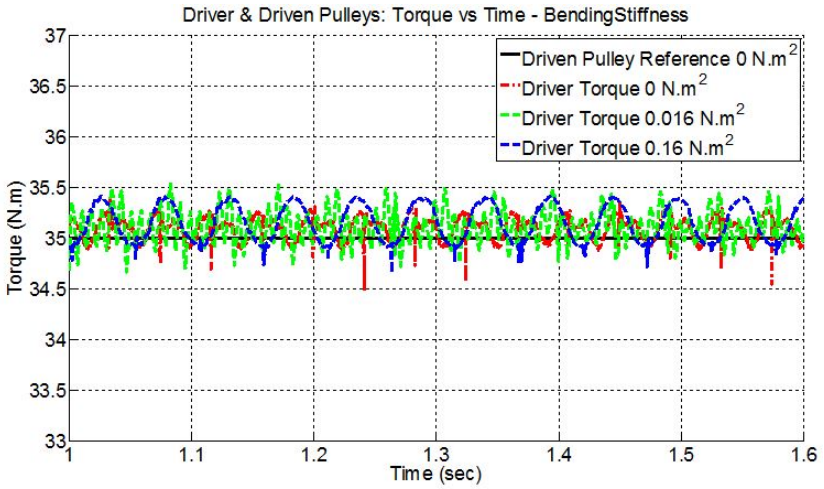

Fig. 5.38. Time-history of the driver applied torque and driven pulley opposing torque as a function of the belt reinforcements bending stiffness.

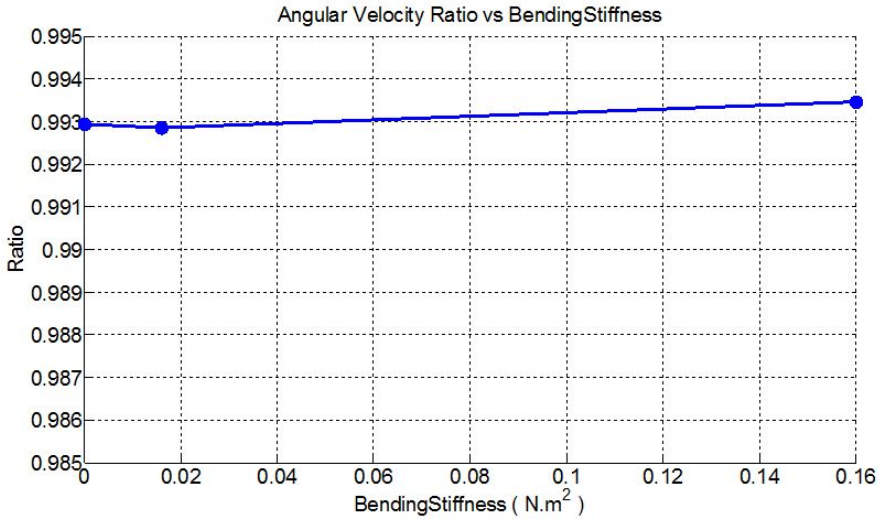

Fig. 5.39. Angular velocity ratio (driven/driver) as a function of the belt reinforcements bending stiffness.

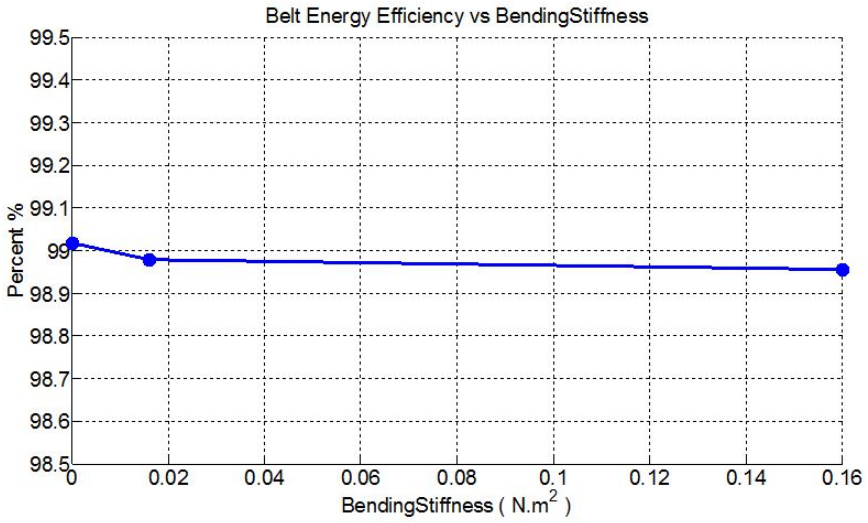

Fig. 5.40. Belt drive energy efficiency as a function of the belt reinforcements bending stiffness.

5.5 Belt Reinforcement Bending Damping

Figures 5.41 to 5.52 show the effect of the bending damping on the steady-state response of the flat belt-drive. Figures 5.41 and 5.42 show bending damping only affects the pulley entrance zone of the tangential stresses. As bending damping increases, the initial negative tangential contact stress and the belt rubber shear stress increases. This results in increase negative work while the belt is entering to the pulley. After the belt-entrance, the effect of bending damping on the tangential contact stress and belt rubber shear stress is insignificant. Figures 5.44 and 5.45 show that the same phenomenon at the pulley entrances is also observed for normal contact stress and the belt rubber normal stress. The entrance oscillations in the normal contact stress of the driver and driven pulleys get larger as the belt reinforcements bending damping is larger. Figures 5.46 and 5.47 show that belt reinforcement bending damping has an insignificant effect on the belt tension force distribution. Figure 5.48 shows that it also plays an insignificant role in belt rubber axial stress. Figure 5.49 shows the driven pulley angular velocity versus time compared to driver pulley for different bending damping values. Despite significant change in the values, the driven pulley angular velocity doesn't significantly change. Figure 5.50 shows the driver pulley torque versus time at different bending damping values. The average torque of the driver pulley is reduced by increasing the belt reinforcements bending damping. Figure 5.51 shows that the angular velocity ratio slightly decreases as the bending damping increases. Figure 5.52 shows that belt energy efficiency significantly drops as the bending damping increases, mainly due to reduction in torque transfer.

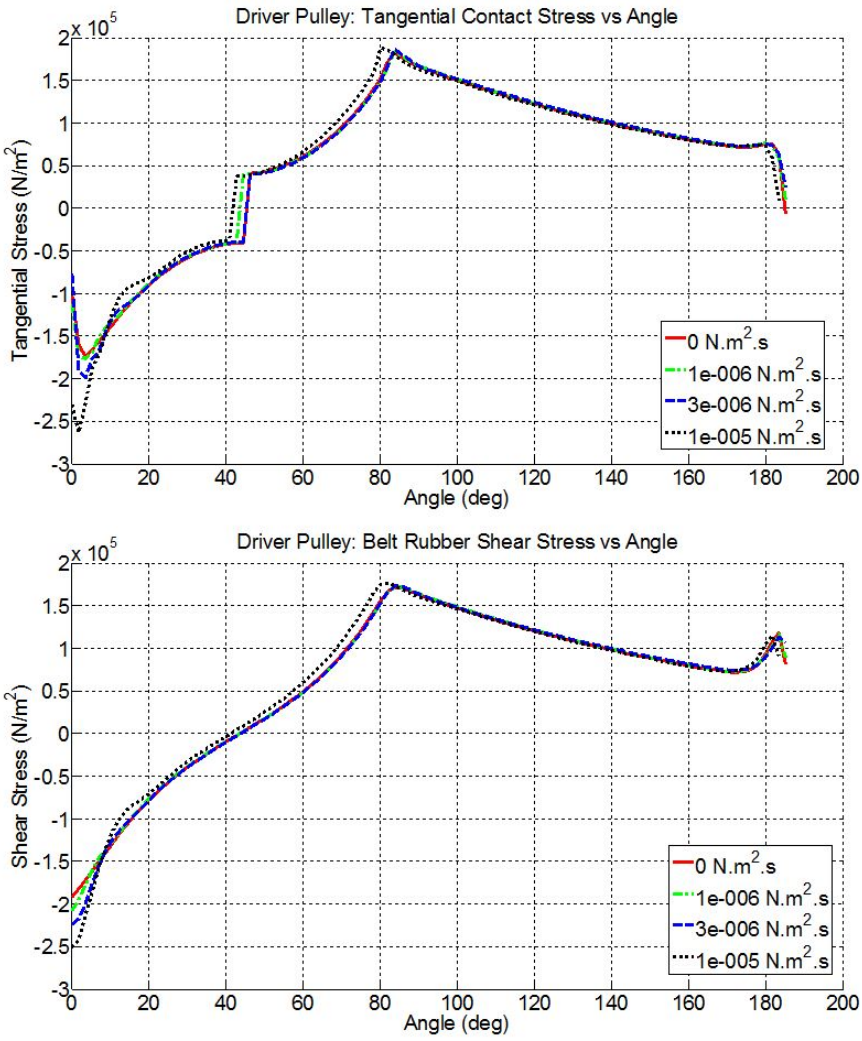

Fig. 5.41. Driver pulley tangential contact stress and rubber shear stress as a function of the belt reinforcements bending damping.

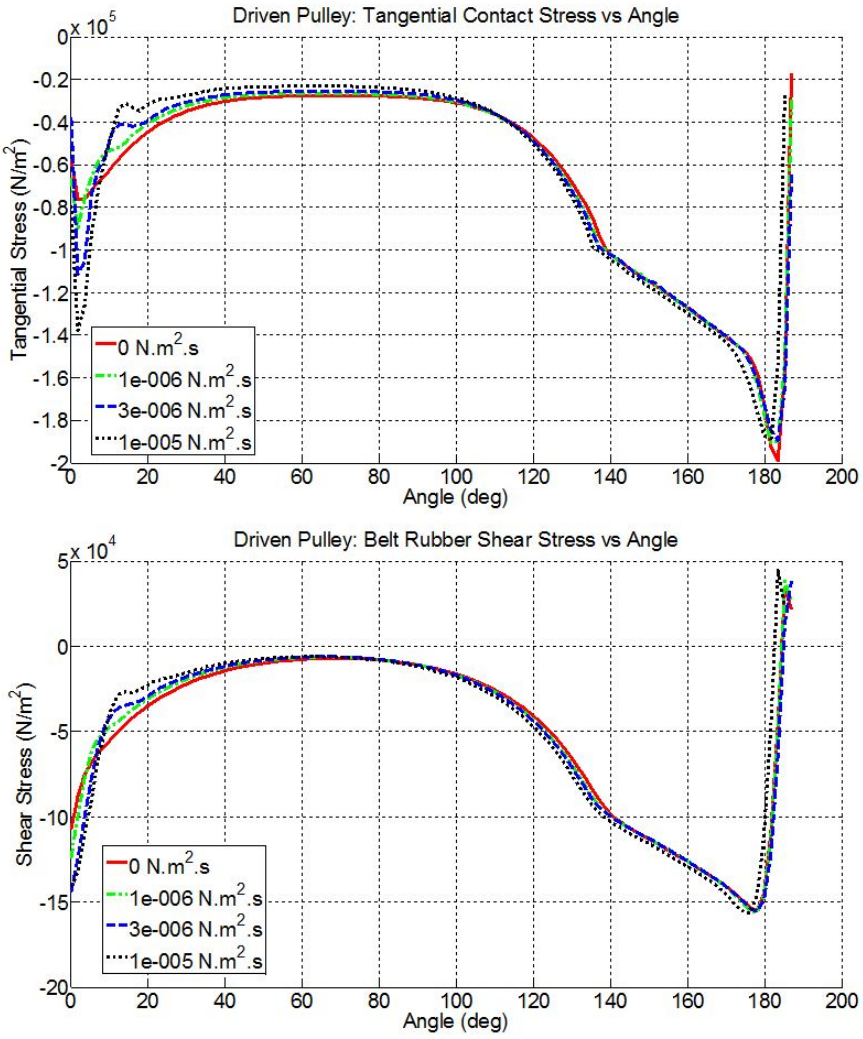

Fig. 5.42. Driven pulley tangential contact stress and rubber shear stress as a function of the belt reinforcements bending damping.

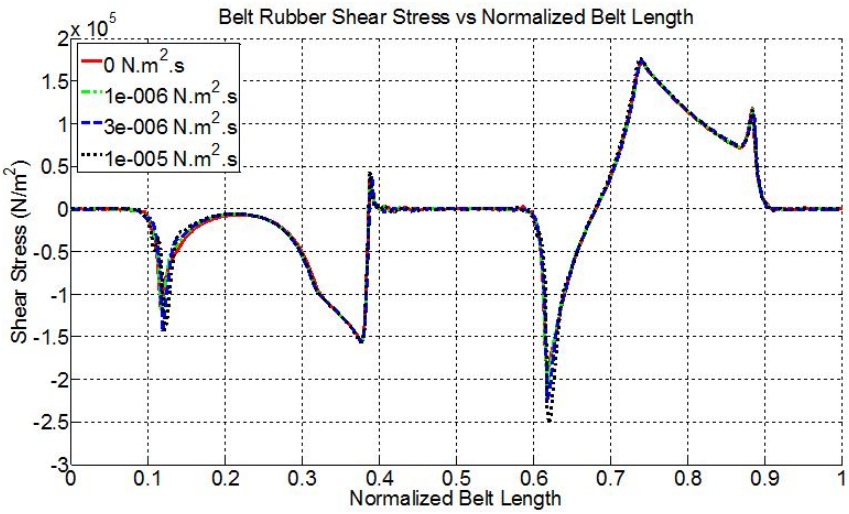

Fig. 5.43. Belt rubber shear stress over the normalized belt length as a function of the belt reinforcements bending damping.

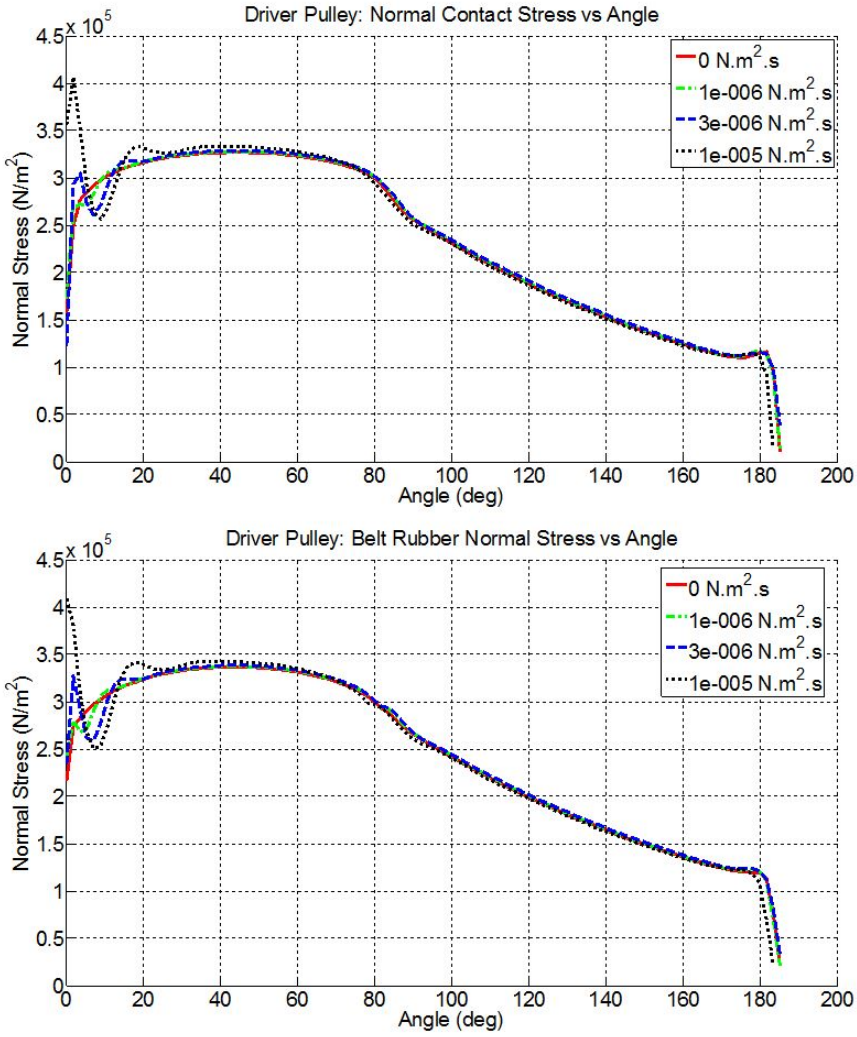

Fig. 5.44. Driver pulley normal contact stress and rubber normal stress as a function of the belt reinforcements bending damping.

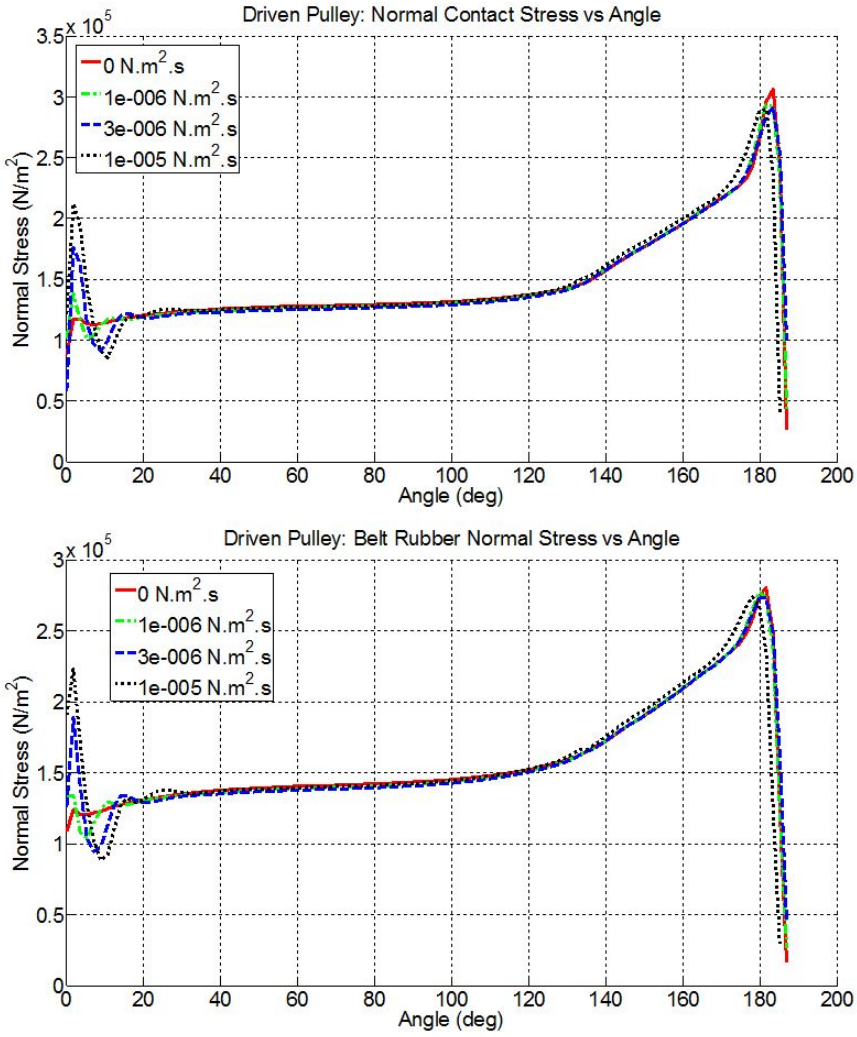

Fig. 5.45. Driven pulley normal contact stress and rubber normal stress as a function of the belt reinforcements bending damping.

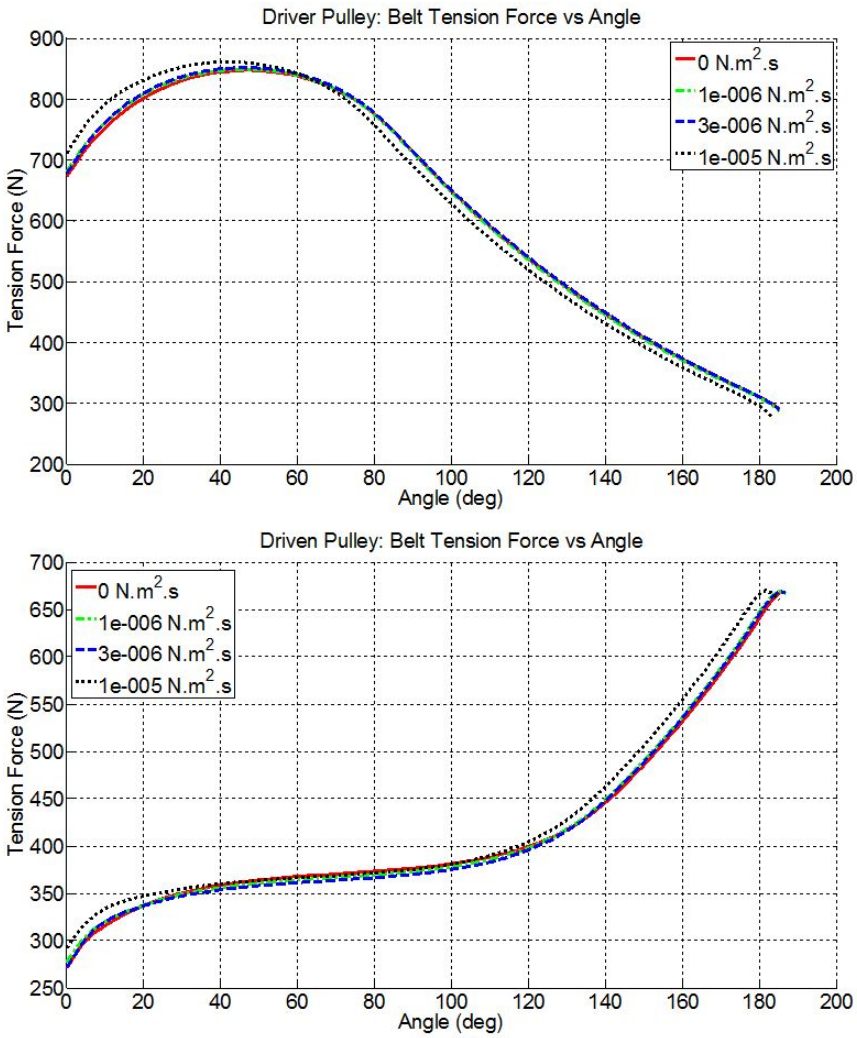

Fig. 5.46. Driver and driven pulleys reinforcements tension force over the pulleys as a function of the belt reinforcements bending damping.

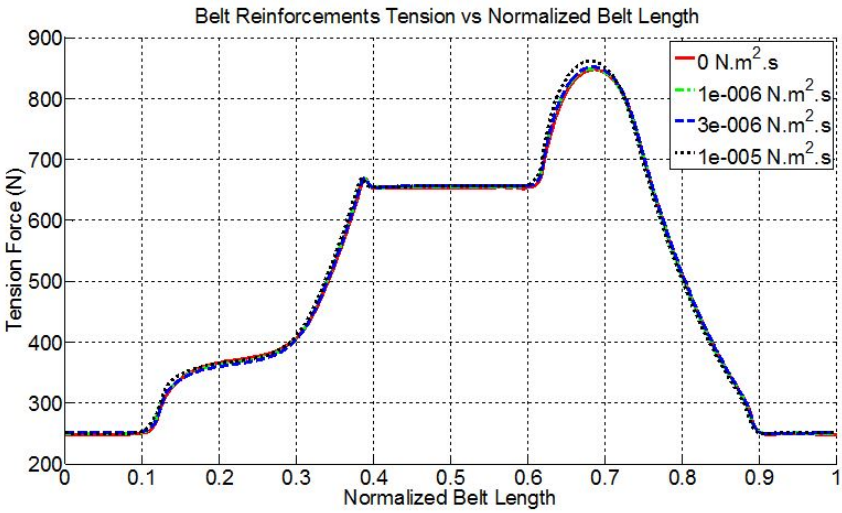

Fig. 5.47. Reinforcements tension force over the belt length as a function of the belt reinforcements bending damping.

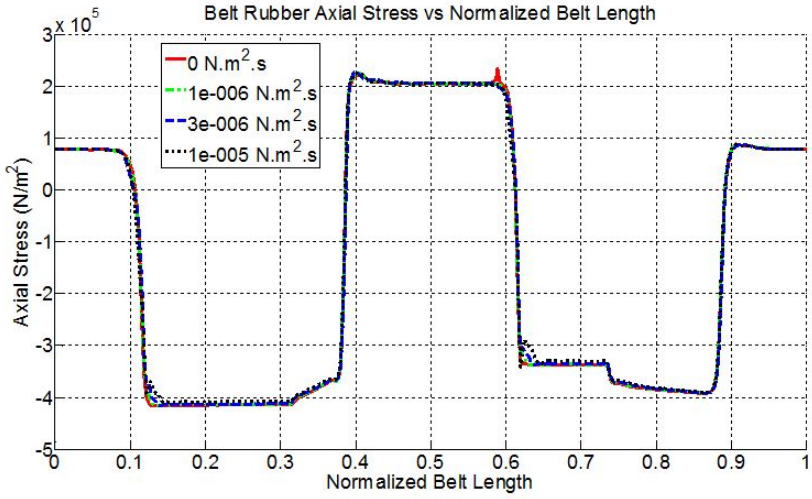

Fig. 5.48. Belt rubber axial stress over the belt length as a function of the belt reinforcements bending damping.

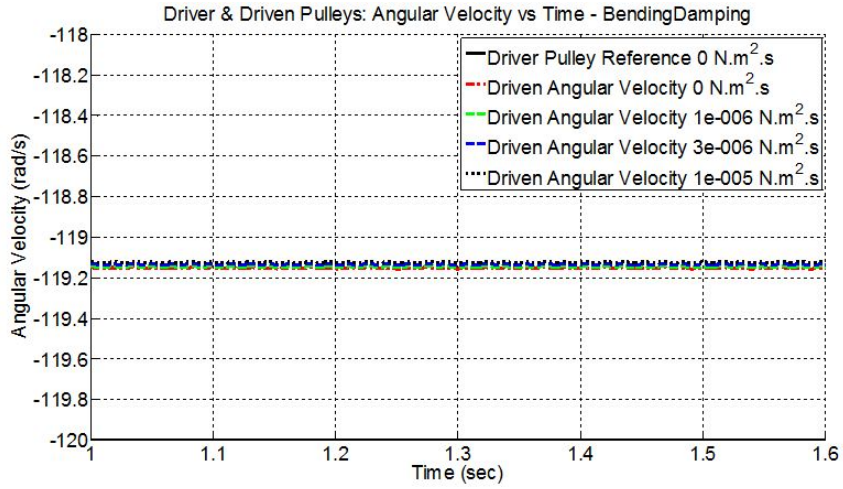

Fig. 5.49. Time-history of the driver and driven pulleys angular velocities as a function of the belt reinforcements bending damping.

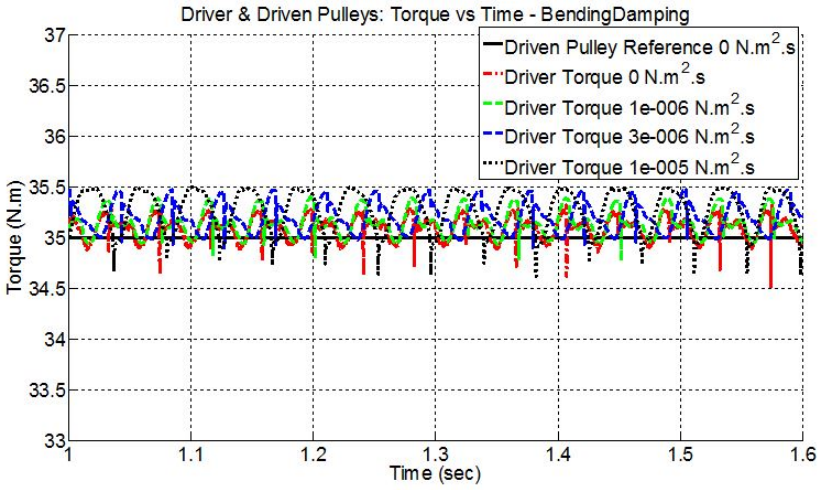

Fig. 5.50. Time-history of the driver applied torque and driven pulley opposing torque as a function of the belt reinforcements bending damping.

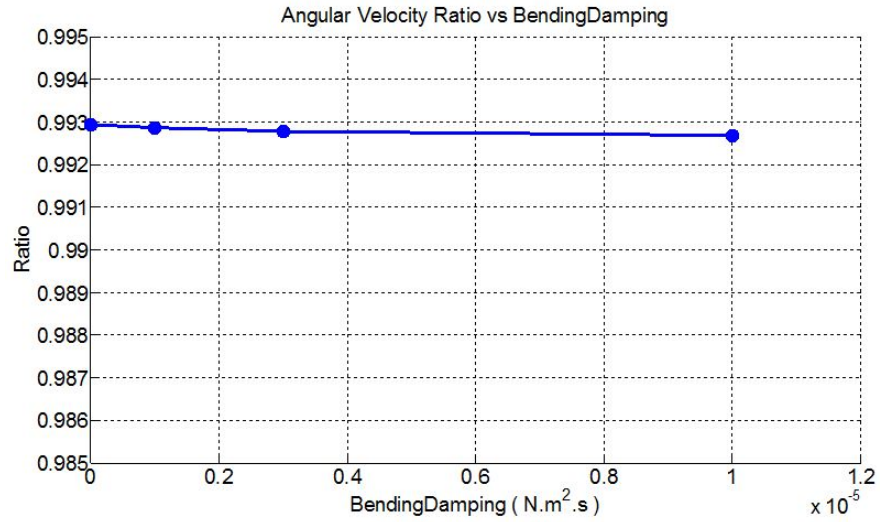

Fig. 5.51. Angular velocity ratio (driven/driver) as a function of the belt reinforcements bending damping.

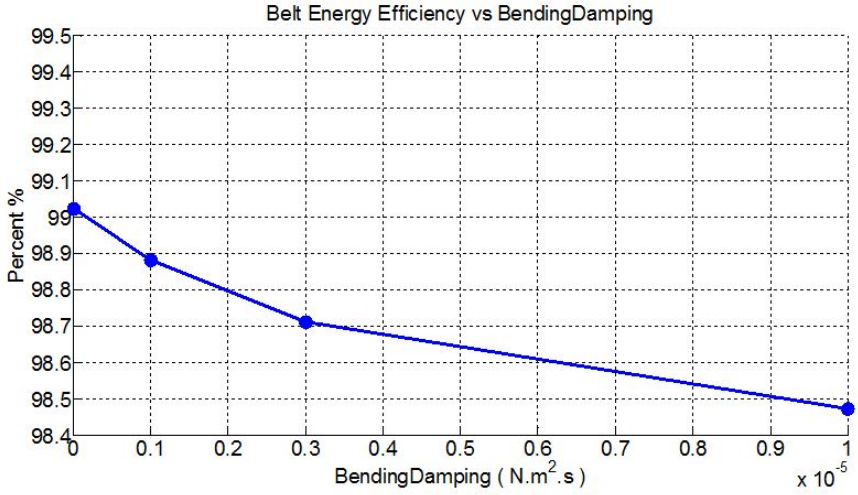

Fig. 5.52. Belt drive energy efficiency as a function of the belt reinforcements bending damping.

6. EFFECT OF OPERATING PARAMETERS

6.1 Driver Pulley Angular Velocity

Figures 6.1 to 6.11 show the effect of angular velocity on the steady-state response of the belt-drive. Figure 6.1 shows that as the angular velocity increases the maximum tangential and rubber shear stress decreases. Also, as the angular velocity increases the positive slip zone width increases and the negative slip zone width decreases. Figures 6.4 and 6.5 show that the normal contact stress at the driven and driver pulley decreases as the angular velocity increases. This is mainly due to the centrifugal force on the belt. Decreased normal contact stress reduces the cap of available friction force. Thus, with higher angular velocity, the torque transfer ability decreases. Figure 6.6 show that as velocity increases the tension over the driver pulley decreases and the tension over the driven pulley increases. Looking at the Figure 6.7 it can be seen that higher angular velocity increases the low belt reinforcement tension between pulleys and reduces the belt reinforcement tension at the driver pulley slip zone. However, on average the average belt tension increases with the driver pulley angular velocity. Figure 6.9 shows the driver torque against time. As the driver angular velocity increases, the stick-slip pulse torque spikes gets bigger. Figure 6.9 also shows the driven pulley torque spikes in a smaller time frame and shows that as the angular velocity decreases the torque fluctuation and spikes decrease and ability to transfer torque increases. Figure 6.10 shows that the operating speed, driver angular velocity, is not a very significant factor in driven to driver angular velocity ratio, ability to transfer velocity. However, Figure 6.11 shows that as the operating speed increases, the belt energy efficiency will slowly decrease.

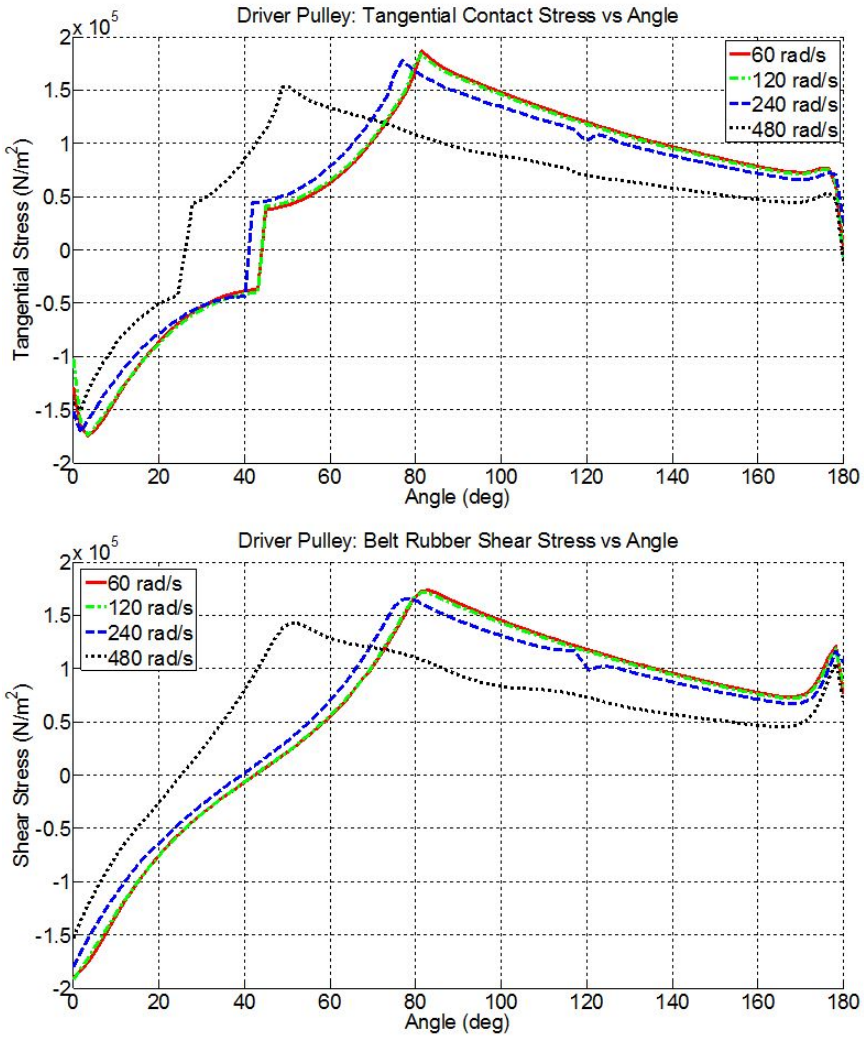

Fig. 6.1. Driver pulley tangential contact stress and rubber shear stress as a function of the driver pulley angular velocity.

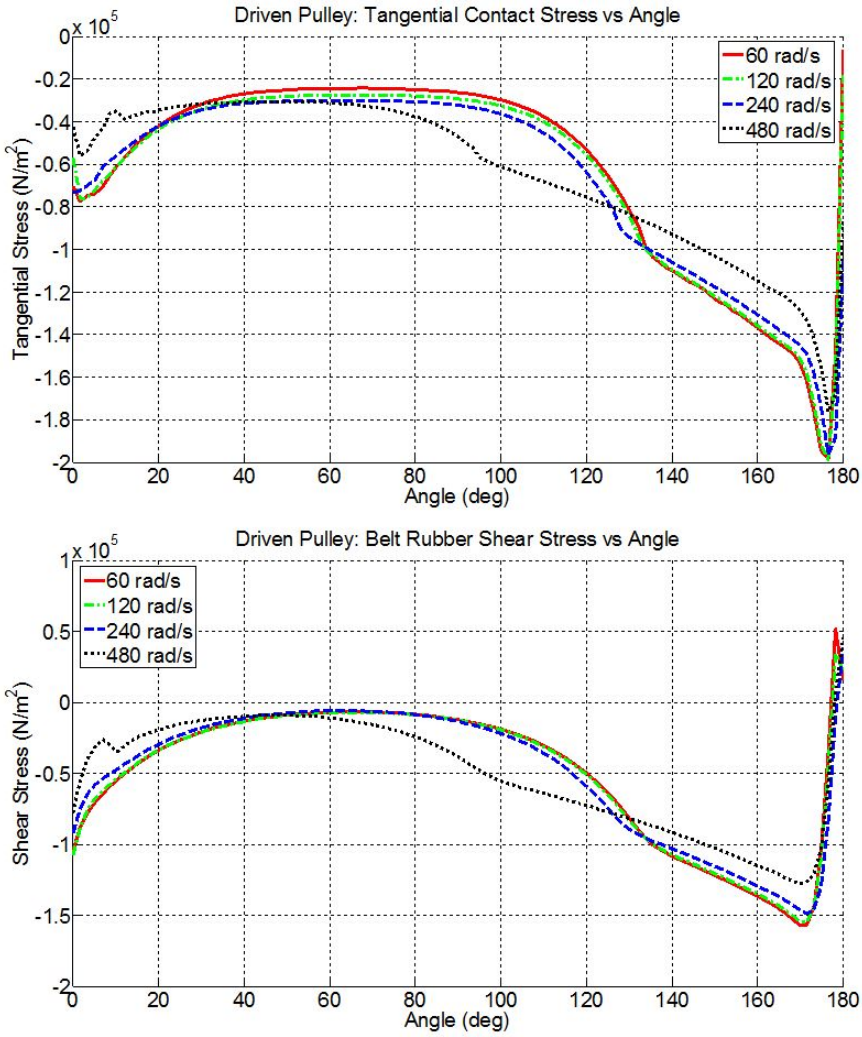

Fig. 6.2. Driven pulley tangential contact stress and rubber shear stress as a function of the driver pulley angular velocity.

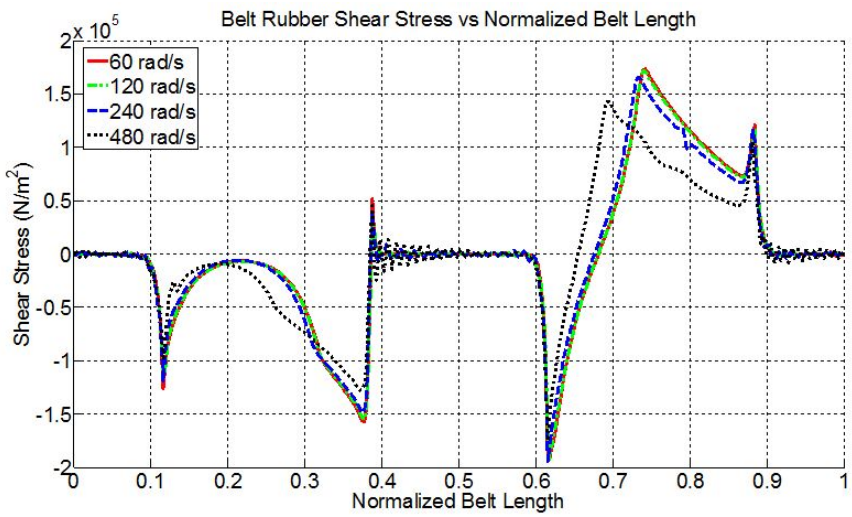

Fig. 6.3. Belt rubber shear stress over the normalized belt length as a function of the driver pulley angular velocity.

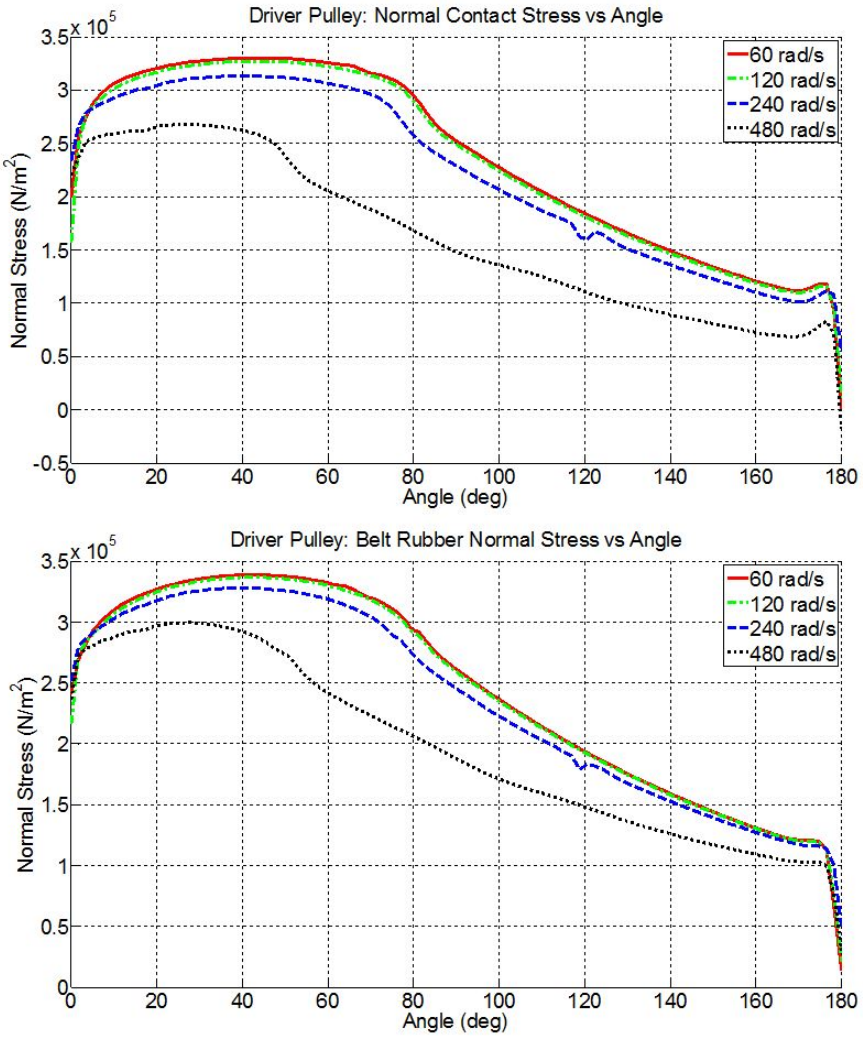

Fig. 6.4. Driver pulley normal contact stress and rubber normal stress as a function of the driver pulley angular velocity.

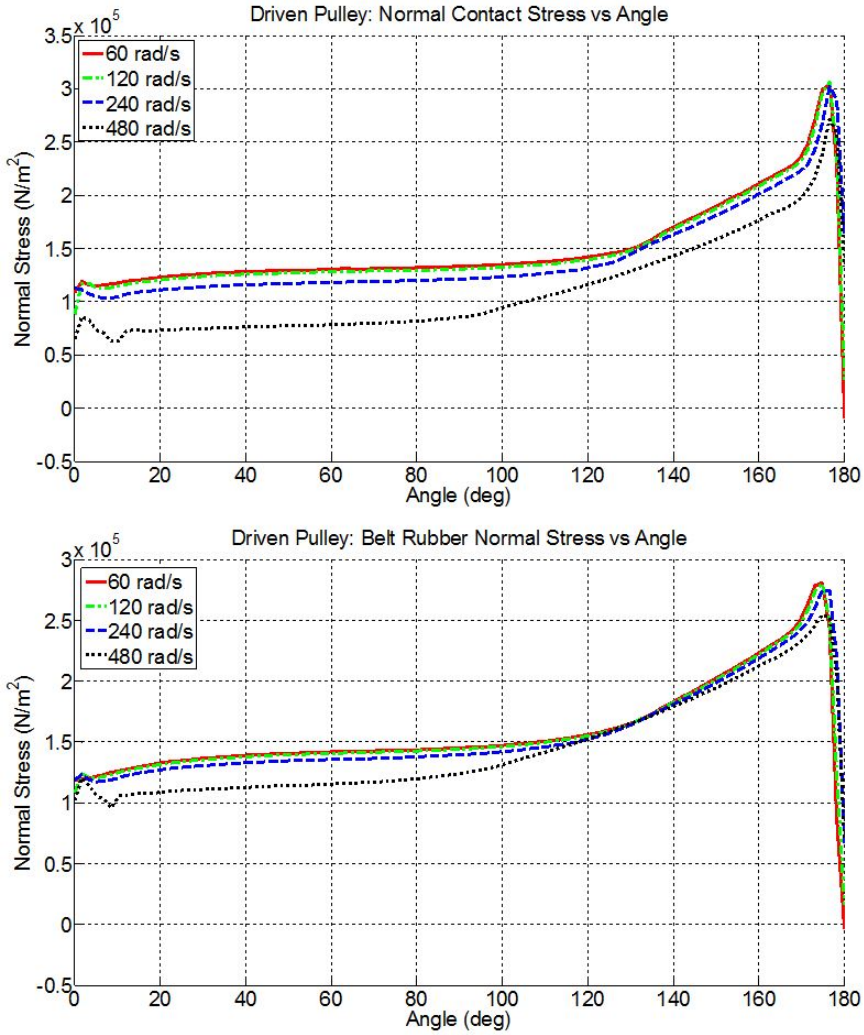

Fig. 6.5. Driven pulley normal contact stress and rubber normal stress as a function of the driver pulley angular velocity.

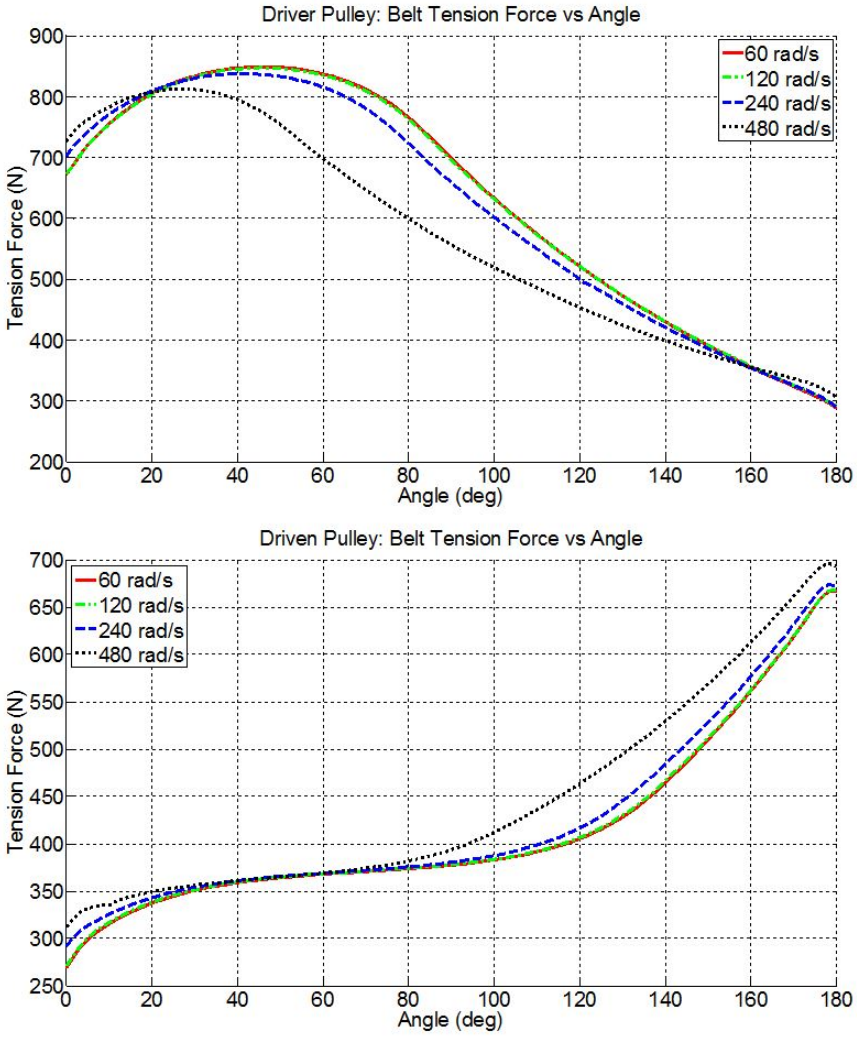

Fig. 6.6. Driver and driven pulleys reinforcements tension force over the pulleys as a function of the driver pulley angular velocity.

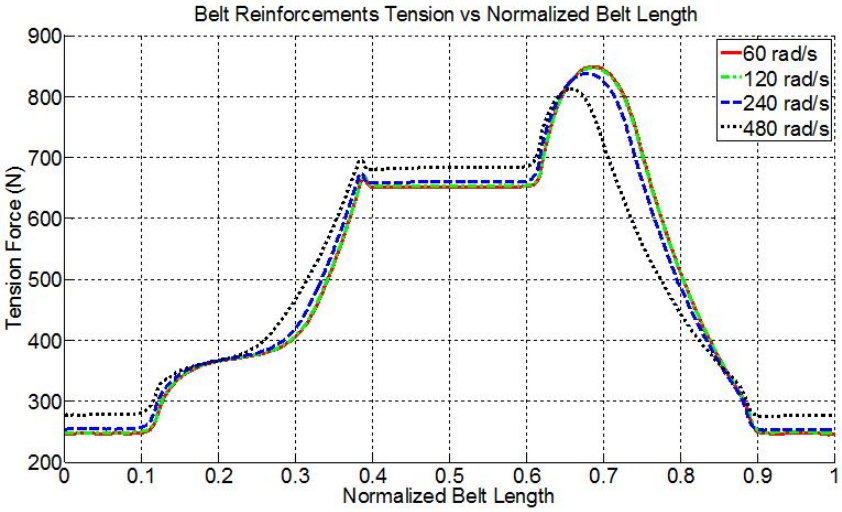

Fig. 6.7. Reinforcements tension force over the belt length as a function of the driver pulley angular velocity.

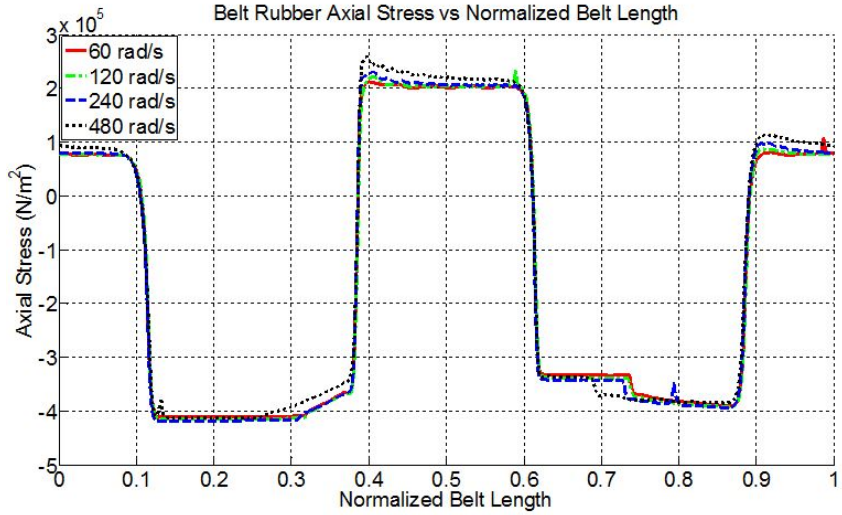

Fig. 6.8. Belt rubber axial stress over the belt length as a function of the driver pulley angular velocity.

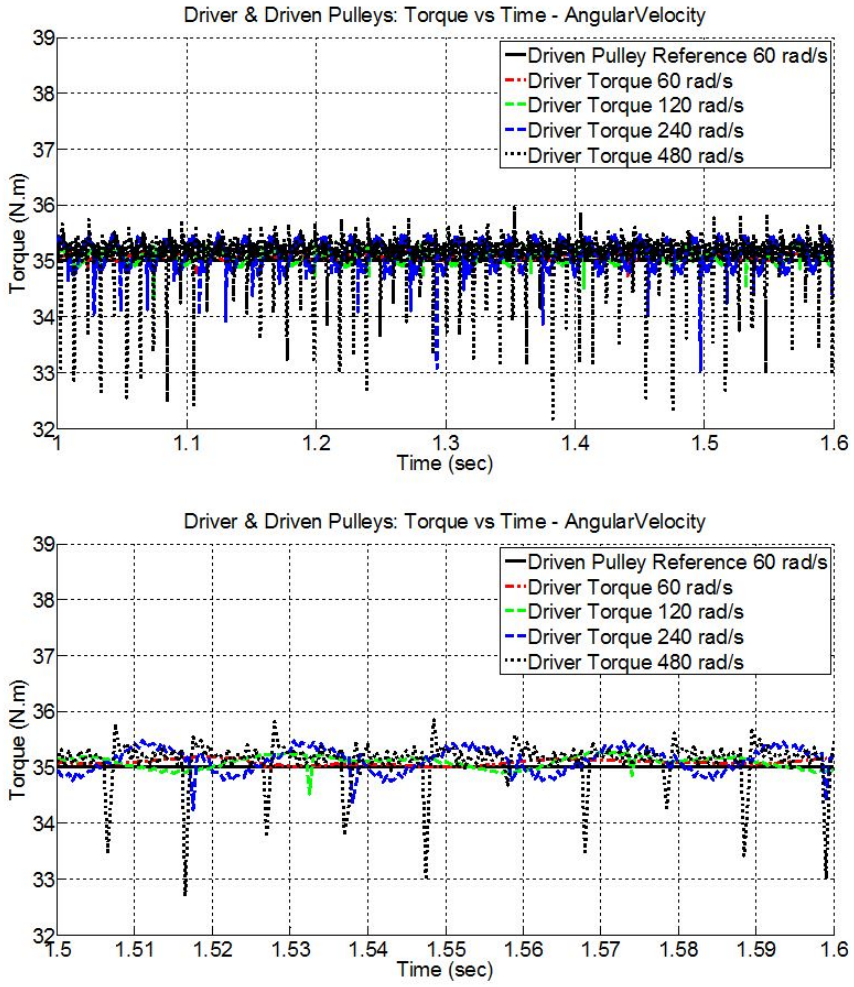

Fig. 6.9. Time-history of the driver applied torque and driven pulley opposing torque as a function of the driver pulley angular velocity.

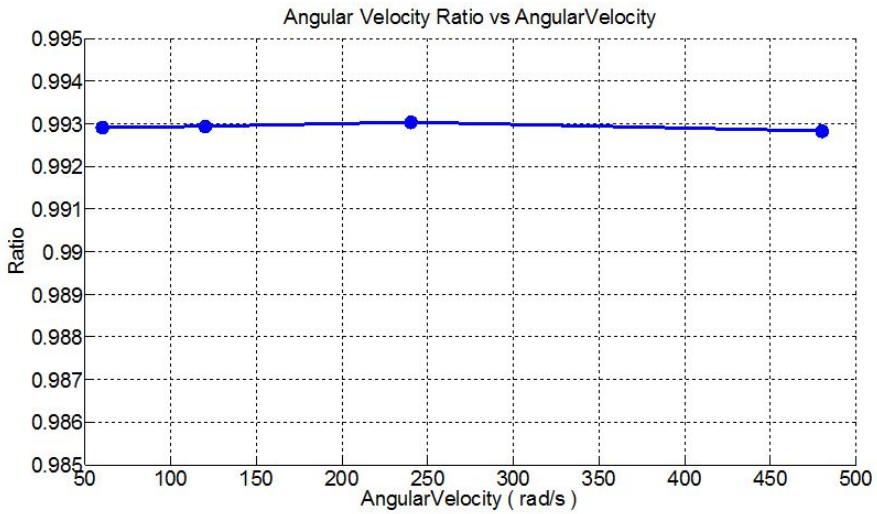

Fig. 6.10. Angular velocity ratio (driven/driver) as a function of the driver pulley angular velocity.

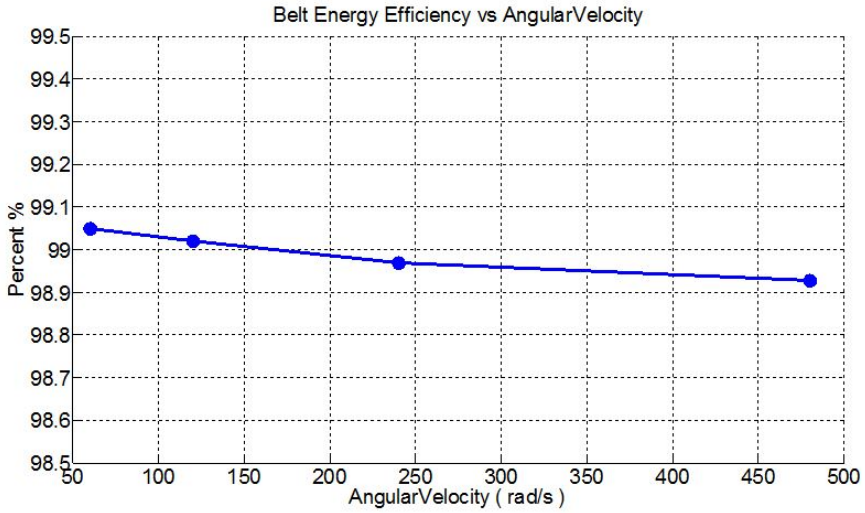

Fig. 6.11. Belt drive energy efficiency as a function of the driver pulley angular velocity.

6.2 Driven Pulley Torque Load Below Gross Slip

Figures 6.12 to 6.24 show the effect of driven torque (the operating load) on the steady-state response of the belt drive. In this section the loads are varied below the gross slip zone torque margins. Figure 6.12 shows the effect of load variation on tangential contact stress and belt rubber shear stress. As the operating load increases on the driven pulley, the maximum tangential stress at the slip zone of driver pulley increases as well as the size of the slip zone. The reduction in the negative slip zone width reduces the available capacity to transfer torque. Figure 6.13 shows that tangential contact stress magnitude over the driven pulley increases at the slip zone as the operating load increases. At the low load condition the driven pulley slip zone tangential stress is close to zero, and the traction occurs at the pulley entrance. Figure 6.14 shows the changes of belt rubber shear stress stick-slip zones as the opposing torque varies from 10N.m to 60N.m. Figure 6.15 shows that the highest normal stress at the stick zone of the driver pulley occurs at the pulley entrance and increases as the torque load increases. At low loads the driver pulley normal stress is almost constant. As the load increases the normal stress becomes steeper and the available normal contact stress, needed to provide friction. Thus, with increasing opposing torque, the ability to grip at the driver pulley reduces. Figure 6.16 shows the driven pulley normal contact stress and belt rubber normal stress versus the angle of the driven pulley. Again the normal force is almost constant for the low torque cases. As the operating torque increases at the driven pulley, the normal stress at the exit of the belt increases. Figures 6.17 and 6.18 show the effect of the operating torque on the belt tension. As the operating torque increases the maximum belt tension increases and the minimum tension decreases. The highest torque applied experiences the highest and lowest tensions. Figure 6.19 shows the belt rubber axial stress over the belt length. Figure 6.22 and 6.23 show the effect of the operating torque on the driven pulley angular velocity. As the operating torque increases the angular velocity significantly reduces. Figure 6.24 shows that driven pulley operating torque

is a significant factor to belt energy efficiency: as the load increases the efficiency decreases.

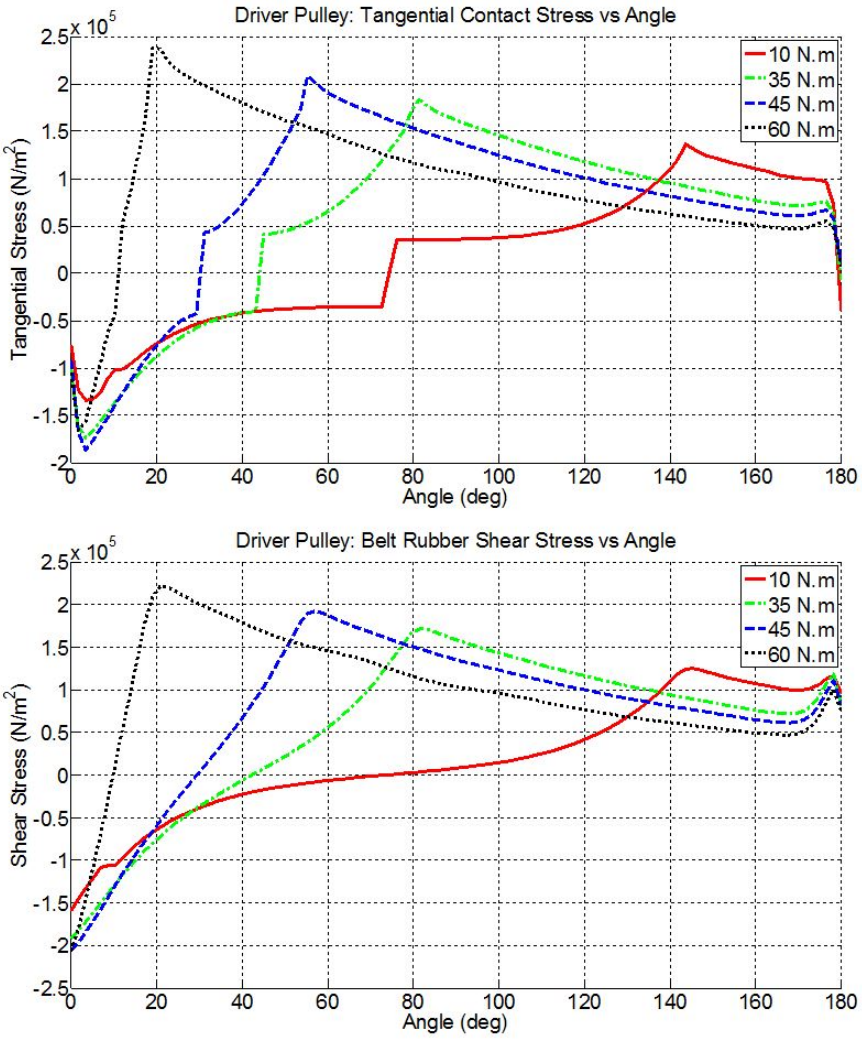

Fig. 6.12. Driver pulley tangential contact stress and rubber shear stress as a function of the driven pulley torque (for opposing torque below gross slip).

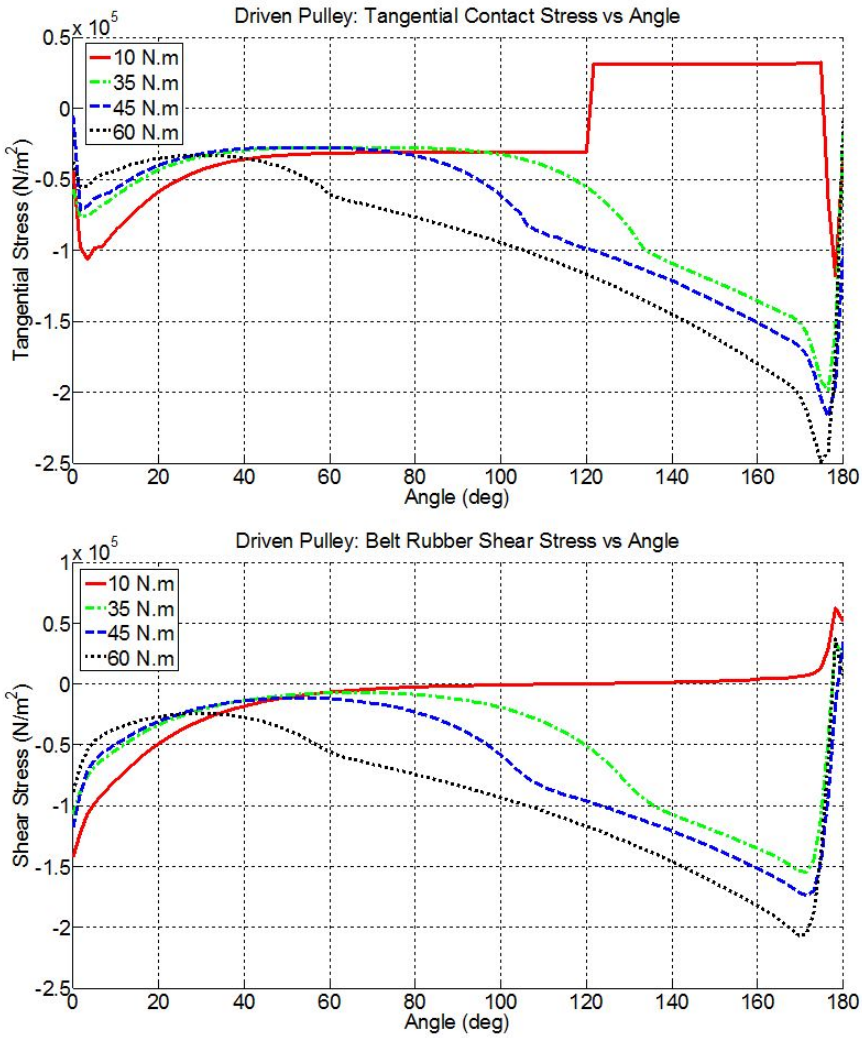

Fig. 6.13. Driven pulley tangential contact stress and rubber shear stress as a function of the driven pulley torque (for opposing torque below gross slip).

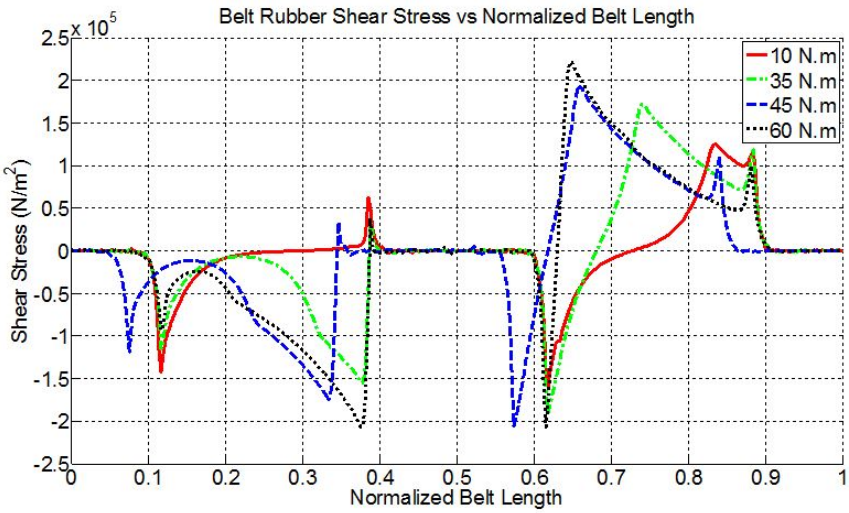

Fig. 6.14. Belt rubber shear stress over the normalized belt length as a function of the driven pulley torque (for opposing torque below gross slip).

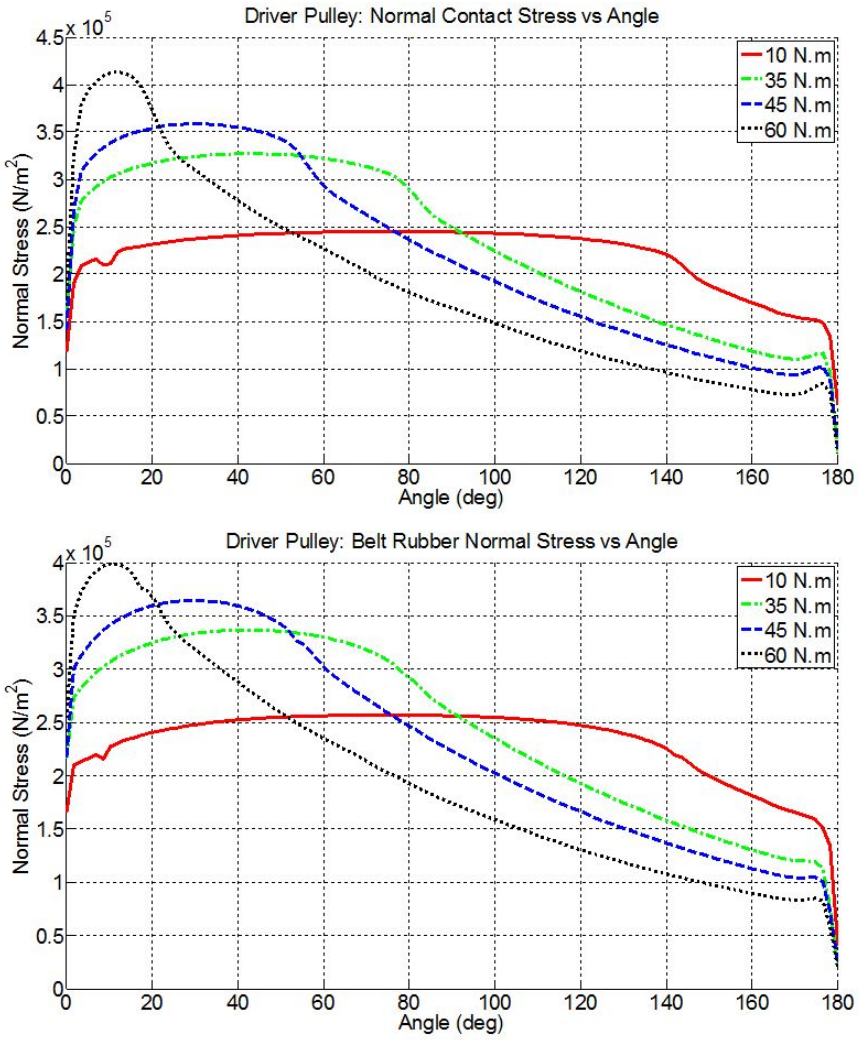

Fig. 6.15. Driver pulley normal contact stress and rubber normal stress as a function of the driven pulley torque (for opposing torque below gross slip).

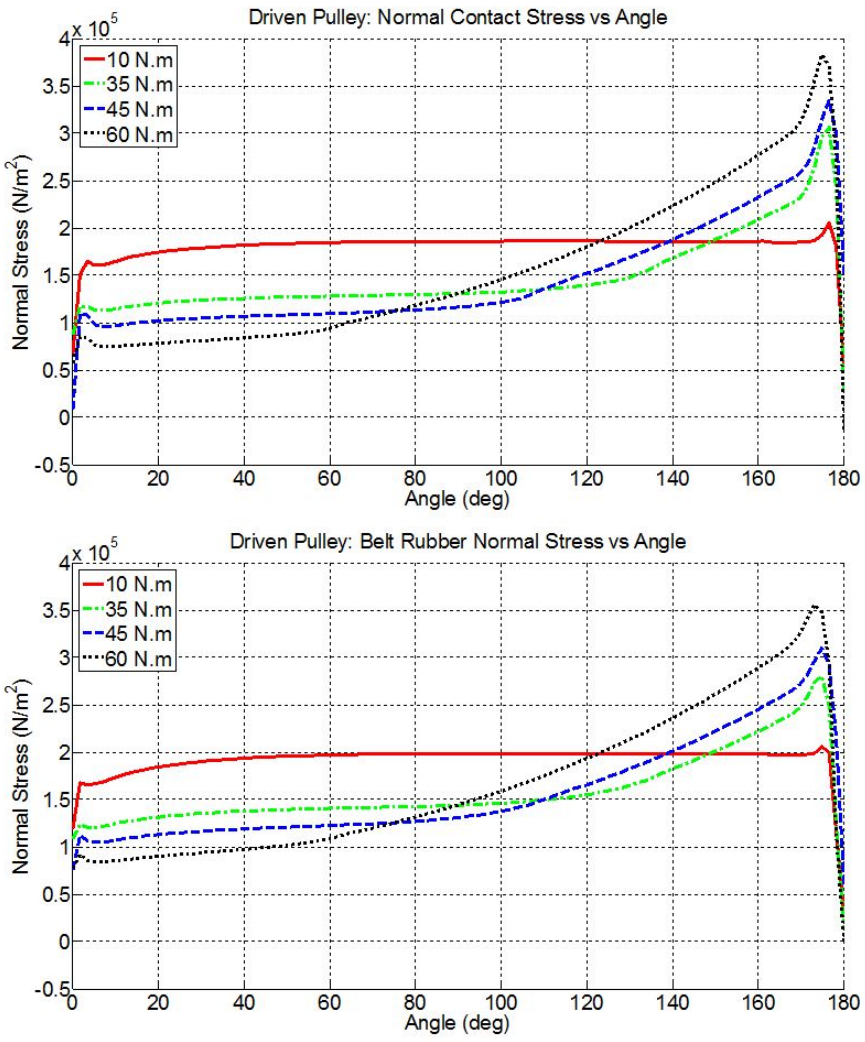

Fig. 6.16. Driven pulley normal contact stress and rubber normal stress as a function of the driven pulley torque (for opposing torque below gross slip).

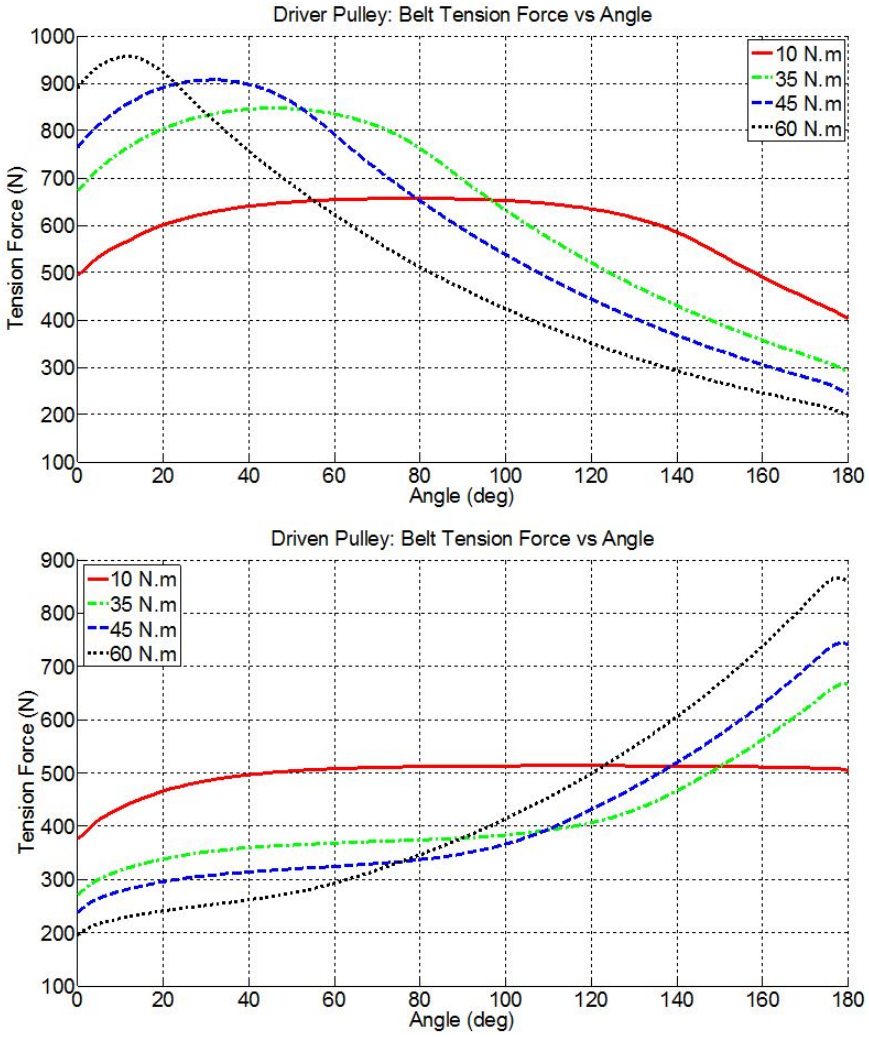

Fig. 6.17. Driver and driven pulleys reinforcements tension force over the pulleys as a function of the driven pulley torque (for opposing torque below gross slip).

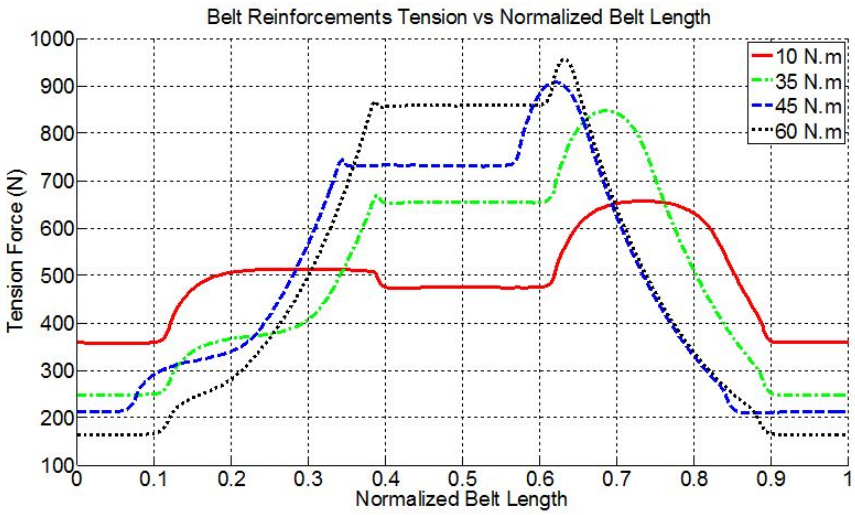

Fig. 6.18. Reinforcements tension force over the belt length as a function of the driven pulley torque (for opposing torque below gross slip).

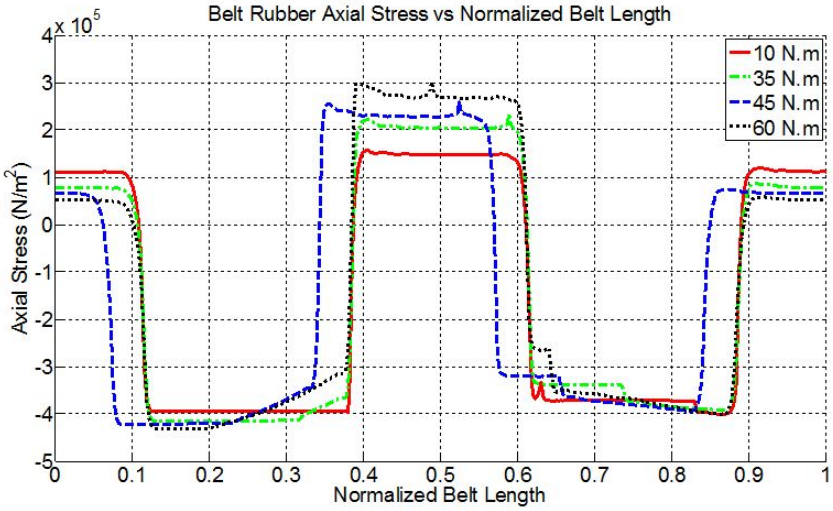

Fig. 6.19. Belt rubber axial stress over the belt length as a function of the driven pulley torque (for opposing torque below gross slip).

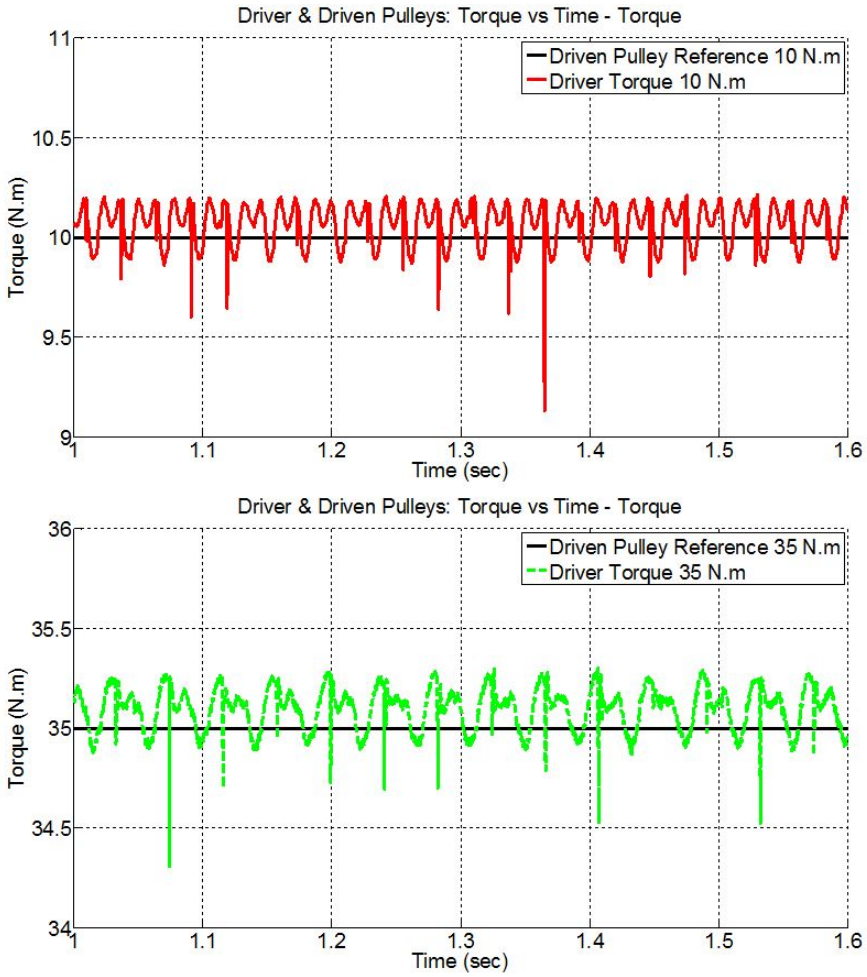

Fig. 6.20. Time-history of the driver applied torque and driven pulley opposing torque as a function of the driven pulley torque for 10 and 35 N.m opposing torque.

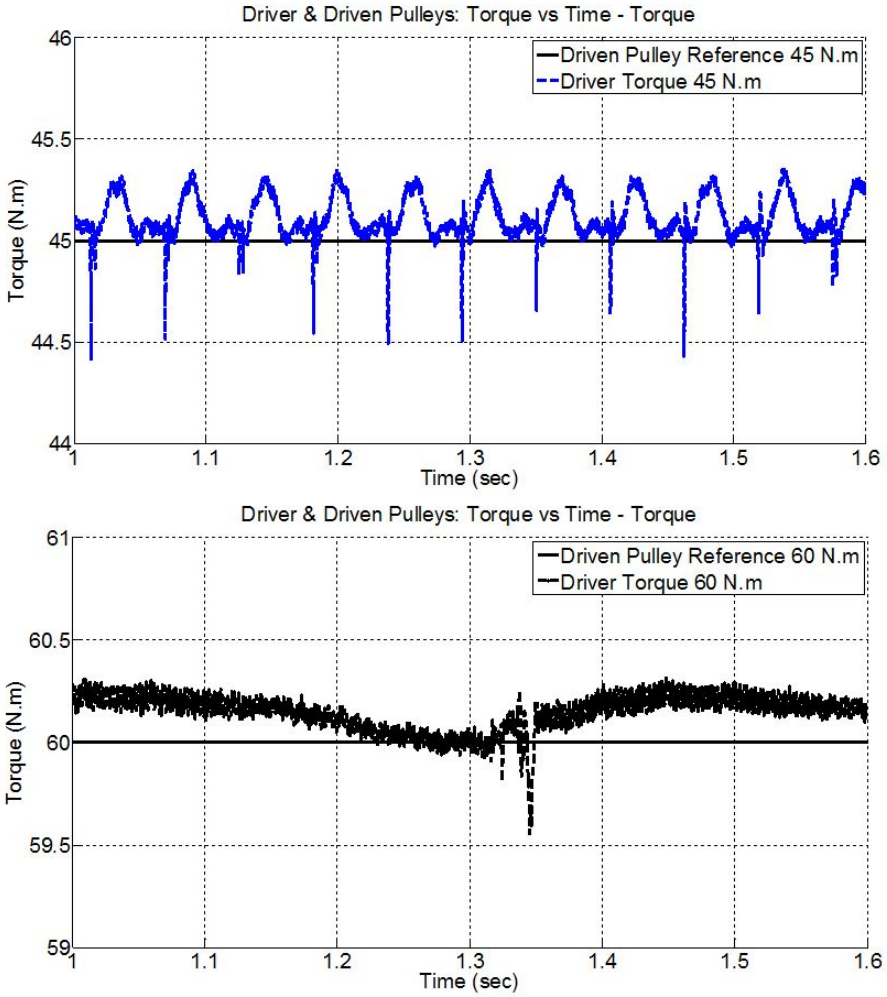

Fig. 6.21. Time-history of the driver applied torque and driven pulley opposing torque as a function of the driven pulley torque for 45 and 60 N.m opposing torque.

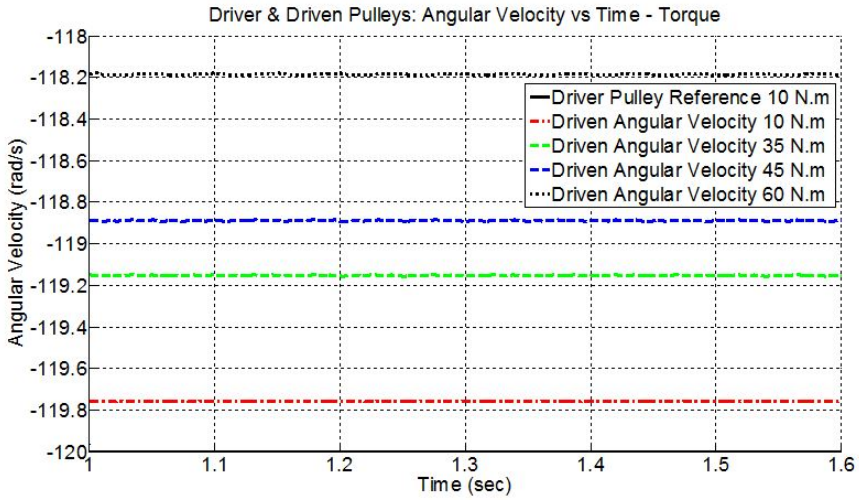

Fig. 6.22. Time-history of the driver and driven pulleys angular velocities as a function of the driven pulley opposing torque (for opposing torque below gross slip).

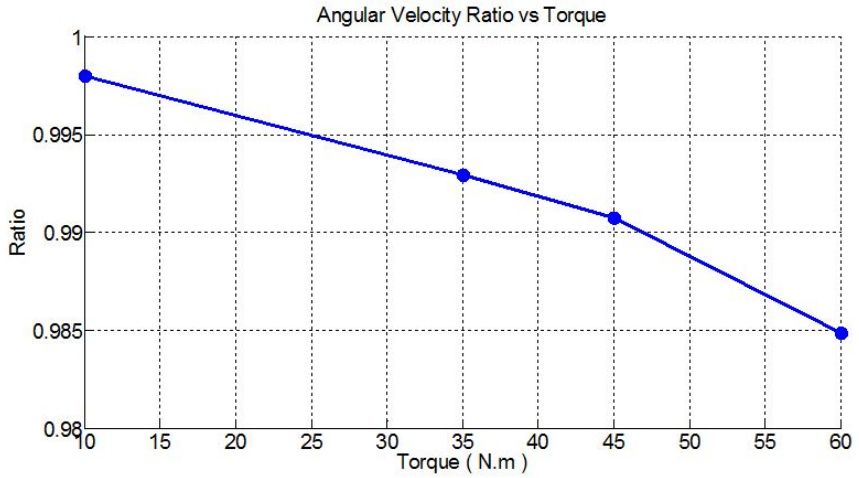

Fig. 6.23. Angular velocity ratio (driven/driver) as a function of the driven pulley opposing torque (for opposing torque below gross slip).

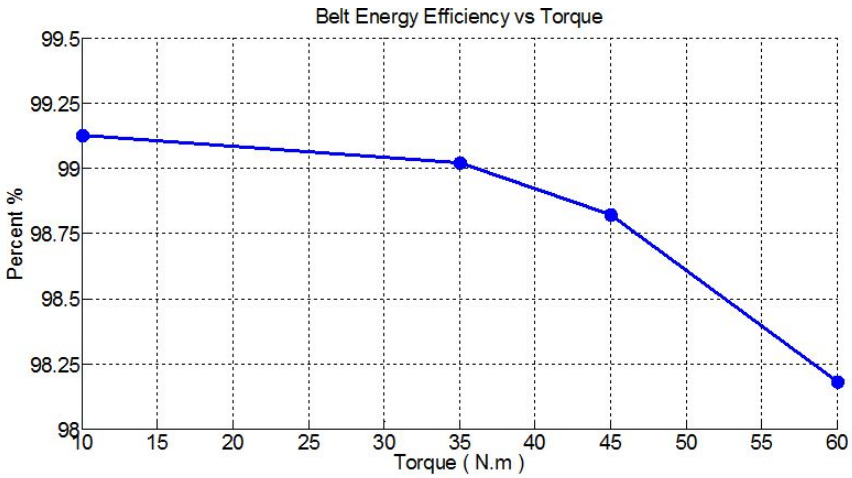

Fig. 6.24. Belt drive energy efficiency as a function of the driven pulley torque (for opposing torque below gross slip).

6.3 Driven Pulley Torque Load At Gross Slip

Figures 6.25 to 6.37 show the effect of driven operating torque load on the steady-state response of the belt drive near gross slip. Figure 6.25 shows the effect of operating torque variation on tangential contact stress and belt rubber shear stress for the driver pulley. The figure shows that negative traction zone on the driver pulley is not present at the gross slip loads. The belt rubber shear stress is maximum at the pulley entrance and reduces as the belt moves to the exit point. For the driven pulley Figure 6.26 shows that at gross slip loads the belt rubber shear stress is minimum at the pulley entrance and increases as the belt moves to the exit point. Figure 6.28 and 6.30 show that the belt normal stress and tension are also maximum at the entrance and minimum at the exit of the driver pulley. Figure 6.29 to 6.30 show that the belt normal stress and tension are also minimum at the entrance of and maximum at the exit of the driven pulley. Figure 6.33 and 6.34 show that large high frequency oscillations in the driver torque are present until full gross slip occurs at which point the torque oscillations die out at about 69.5 N.m. Figure 6.35 and 6.36 show that after 65N.m operating load, the angular velocity of the driven pulley significantly drops.

Looking at the figure 6.36 we see that in very a very short margin of 65 to 70N.m the angular velocity ratio hits 0. Figure 6.37 shows the belt energy efficiency as a function of operating load. From 10N.m to 65N.m the belt drive has linear degradation in energy efficiency. After that point, the decline takes an exponential form until it reaches 0 at 70 N.m.

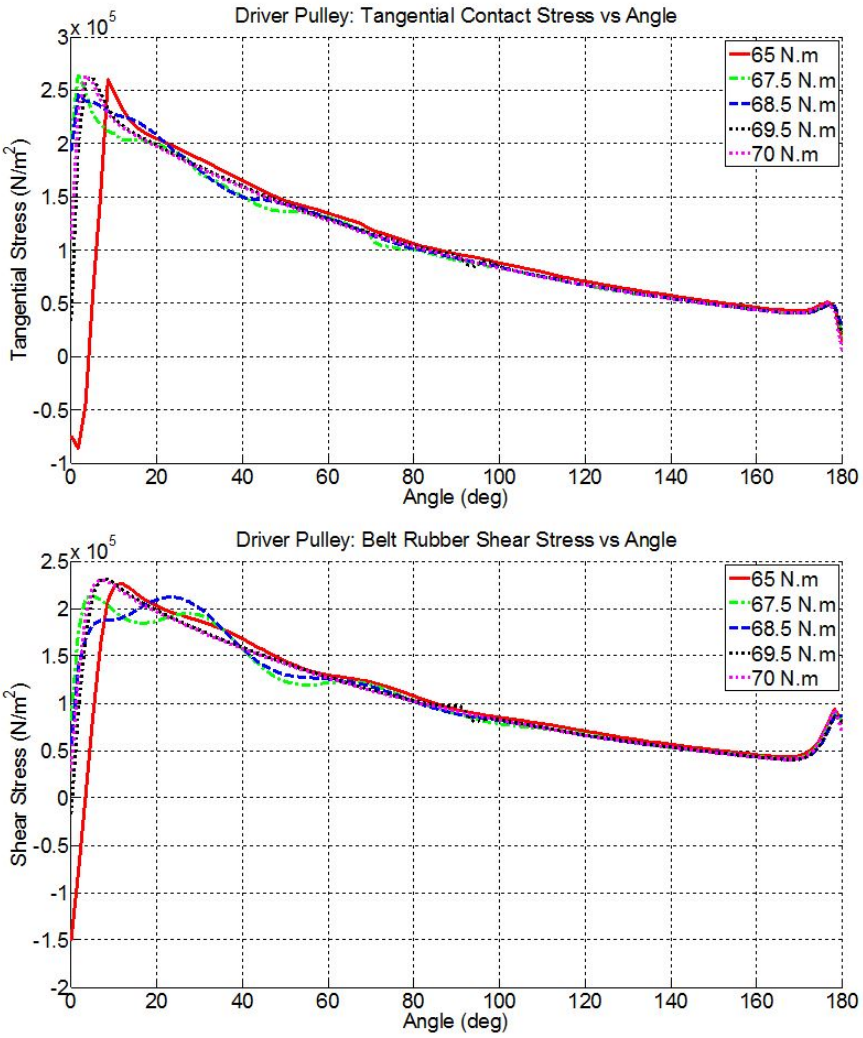

Fig. 6.25. Driver pulley tangential contact stress and rubber shear stress as a function of the driven pulley torque (for opposing torque values near gross slip).

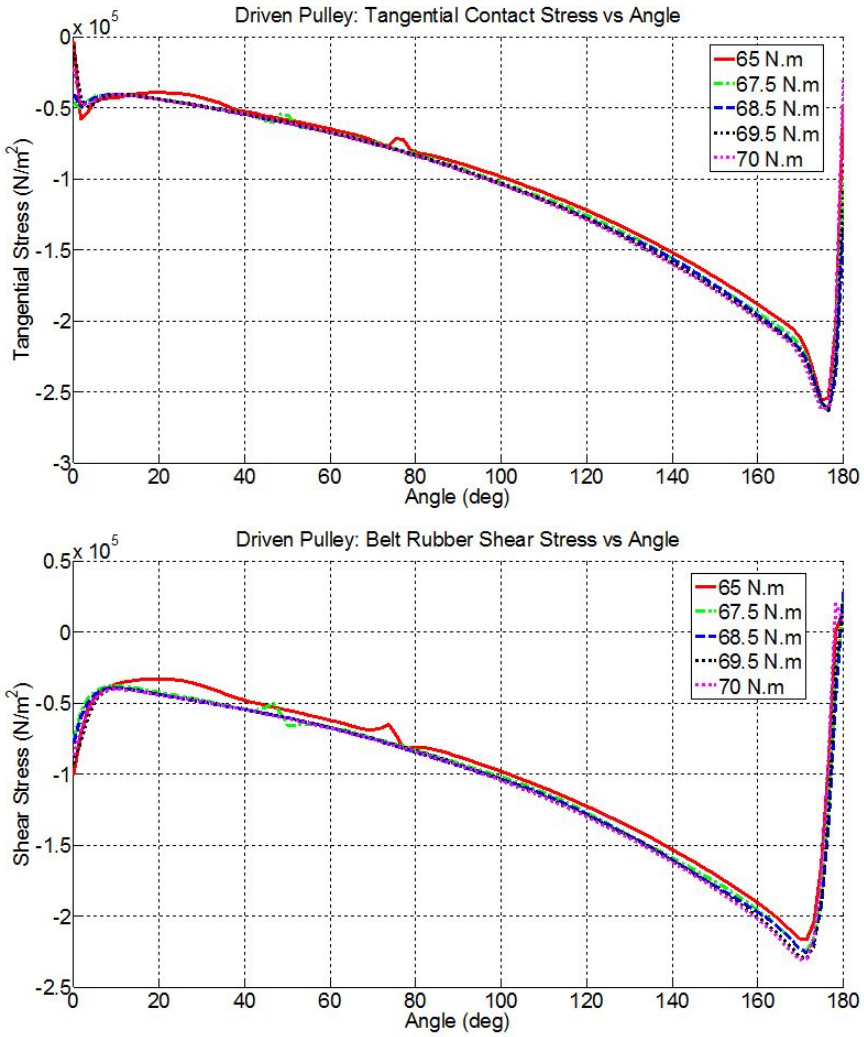

Fig. 6.26. Driven pulley tangential contact stress and rubber shear stress as a function of the driven pulley torque (for opposing torque values near gross slip).

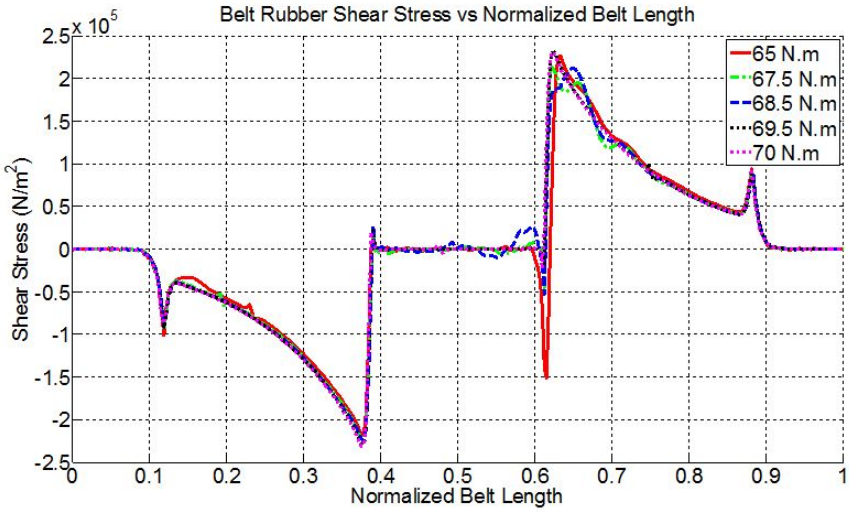

Fig. 6.27. Belt rubber shear stress over the normalized belt length as a function of the driven pulley torque (for opposing torque values near gross slip).

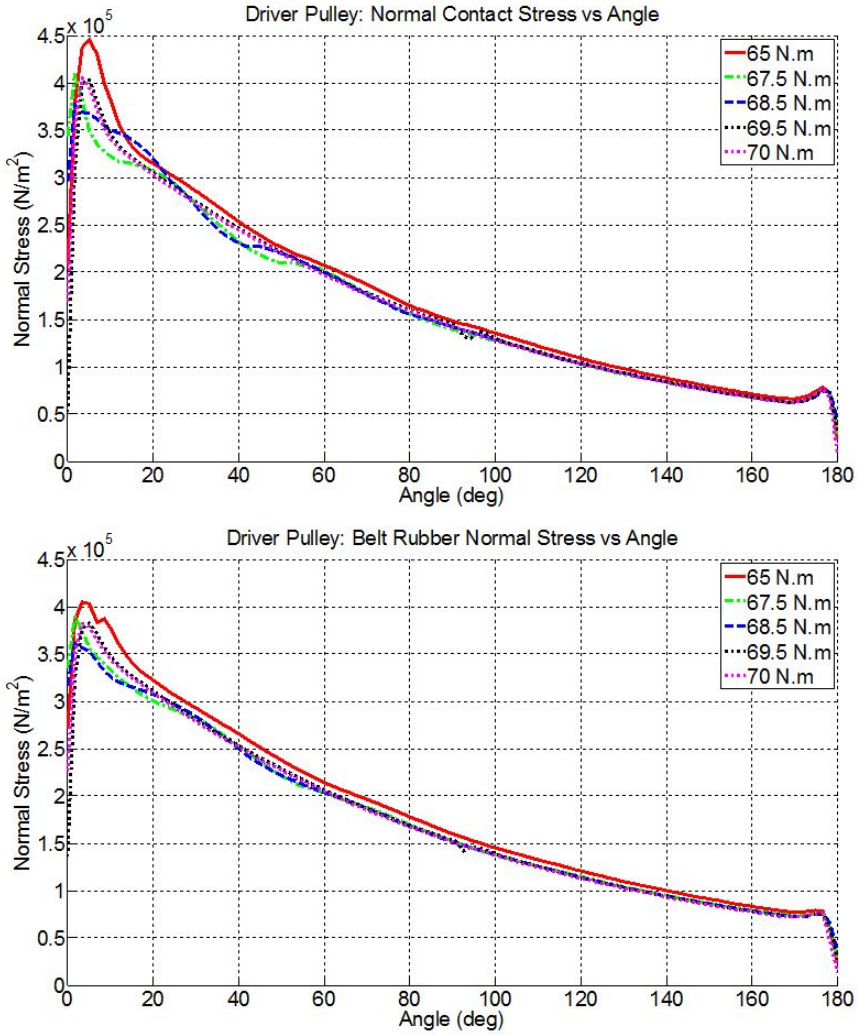

Fig. 6.28. Driver pulley normal contact stress and rubber normal stress as a function of the driven pulley torque (for opposing torque values near gross slip).

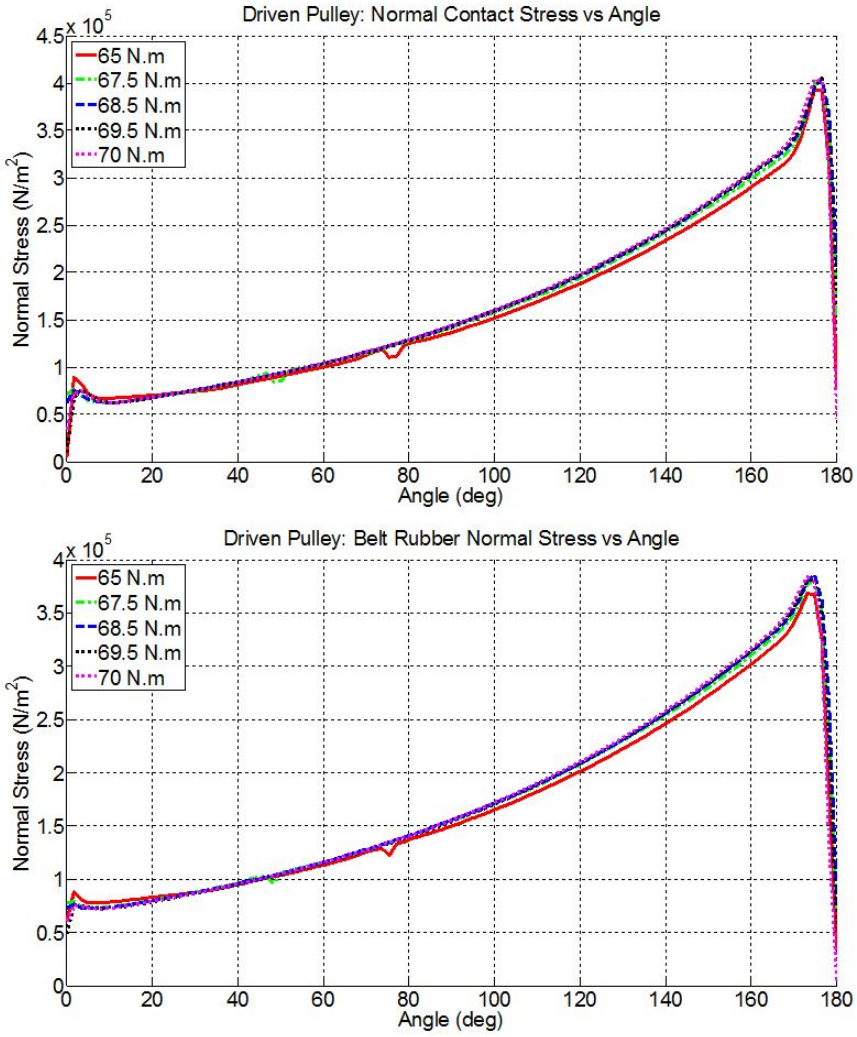

Fig. 6.29. Driven pulley normal contact stress and rubber normal stress as a function of the driven pulley torque (for opposing torque values near gross slip).

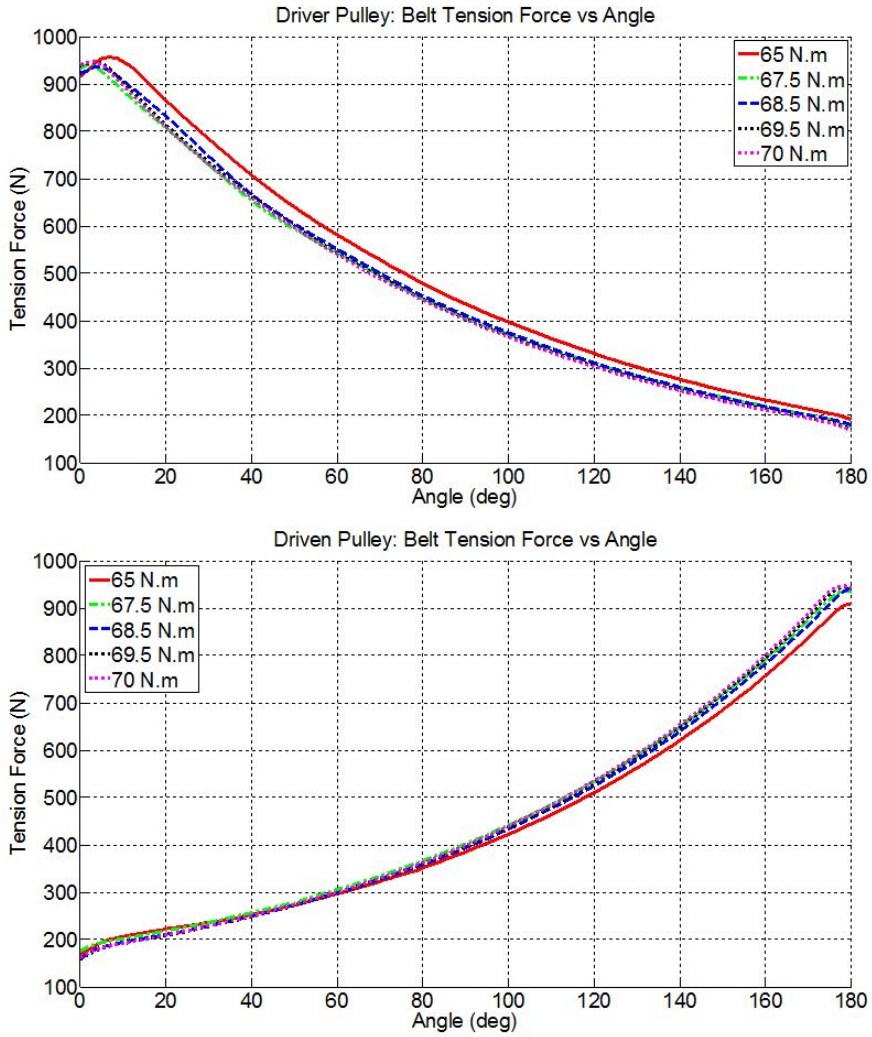

Fig. 6.30. Driver and driven pulleys reinforcements tension force over the pulleys as a function of the driven pulley torque (for opposing torque values near gross slip).

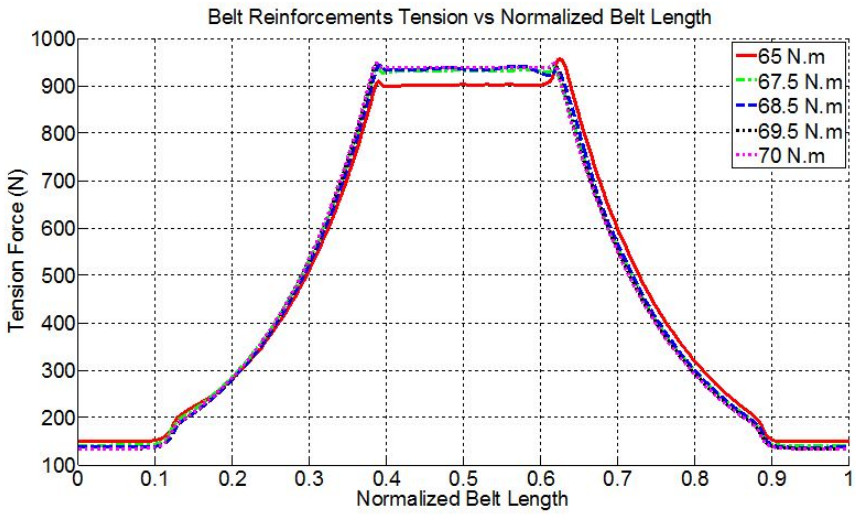

Fig. 6.31. Reinforcements tension force over the belt length as a function of the driven pulley torque (for opposing torque values near gross slip).

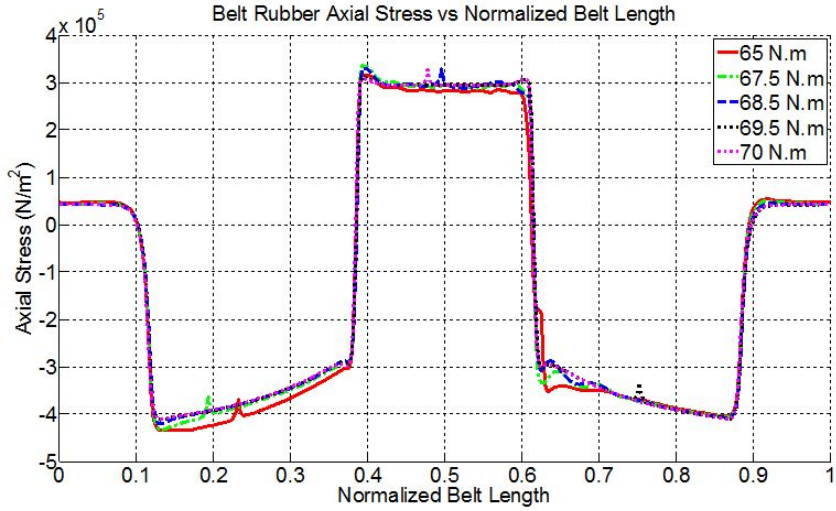

Fig. 6.32. Belt rubber axial stress over the belt length as a function of the driven pulley torque (for opposing torque values near gross slip).

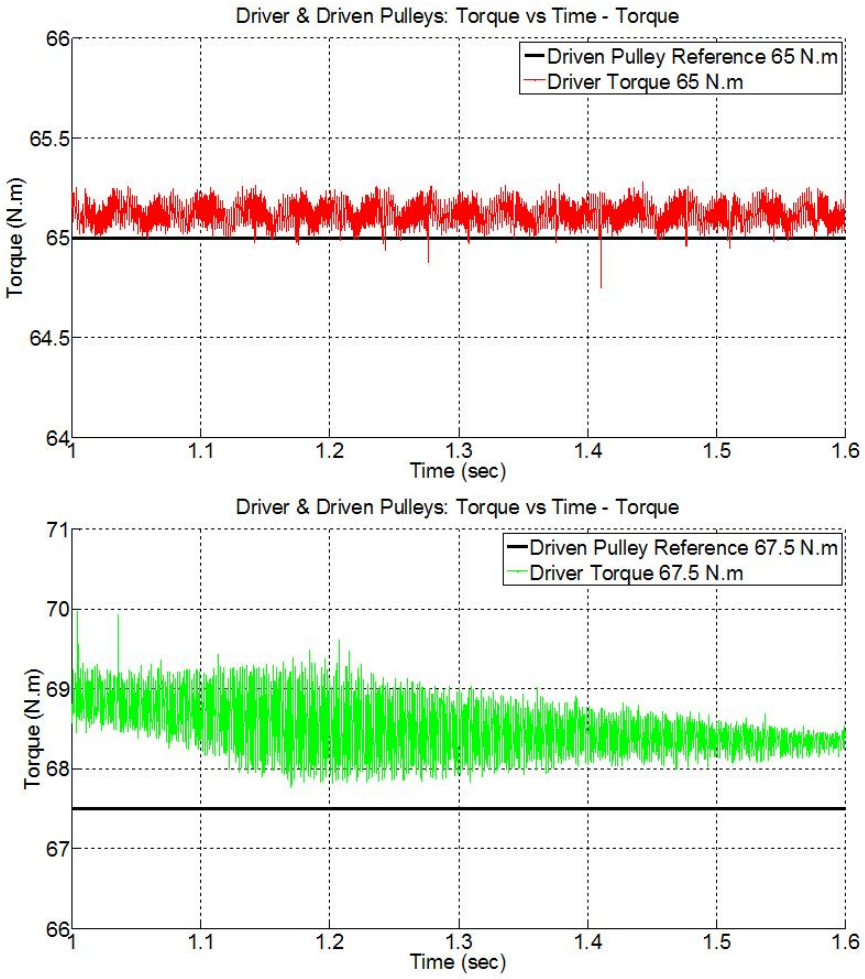

Fig. 6.33. Time-history of the driver applied torque and driven pulley opposing torque as a function of the driven pulley torque for 65 and 67.5 N.m opposing torque.

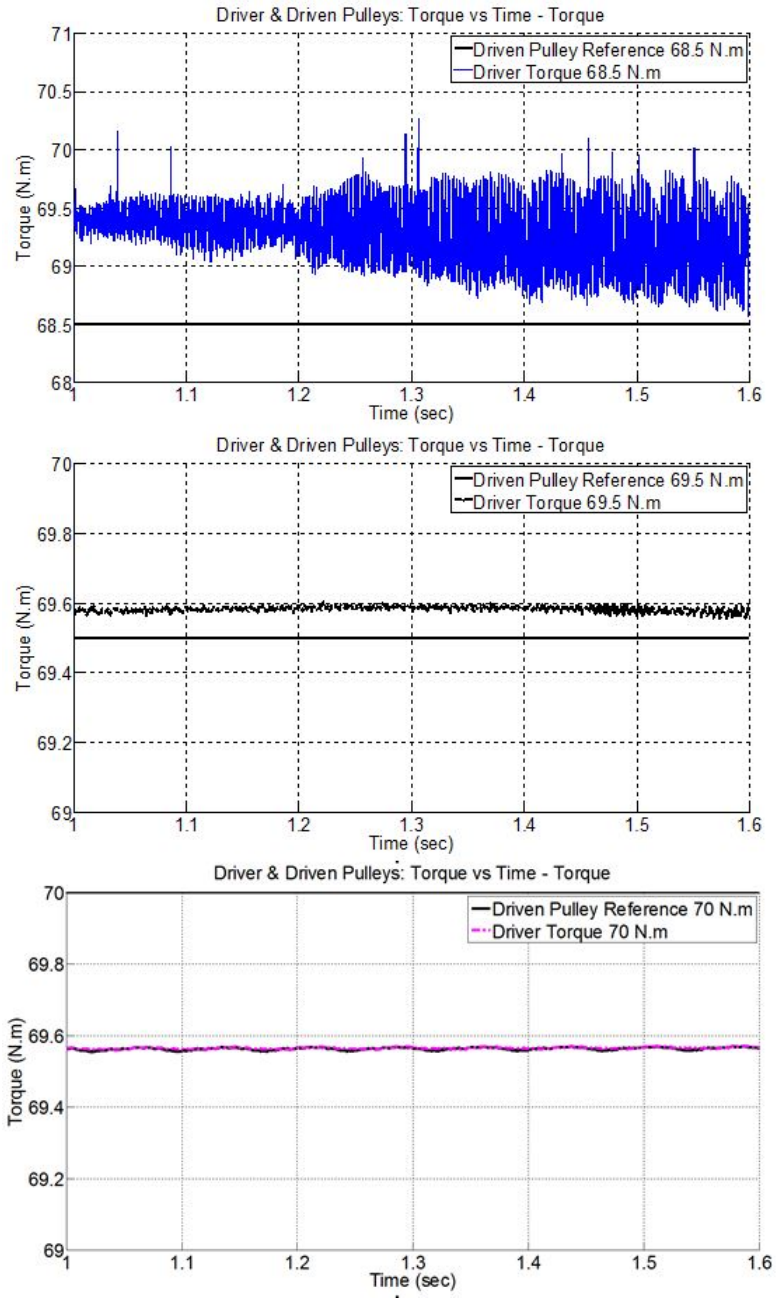

Fig. 6.34. Time-history of the driver applied torque and driven pulley opposing torque as a function of the driven pulley torque for 68.5, 69.5 and 70 N.m opposing torque.

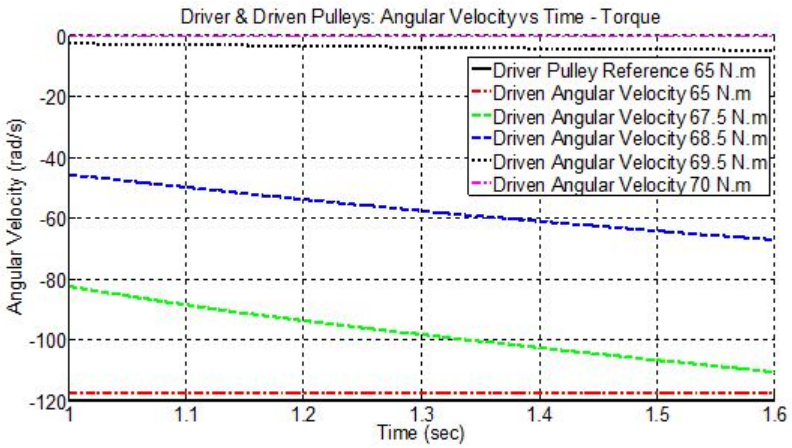

Fig. 6.35. Time-history of the driver and driven pulleys angular velocities as a function of the driven pulley opposing torque (for opposing torque values near gross slip).

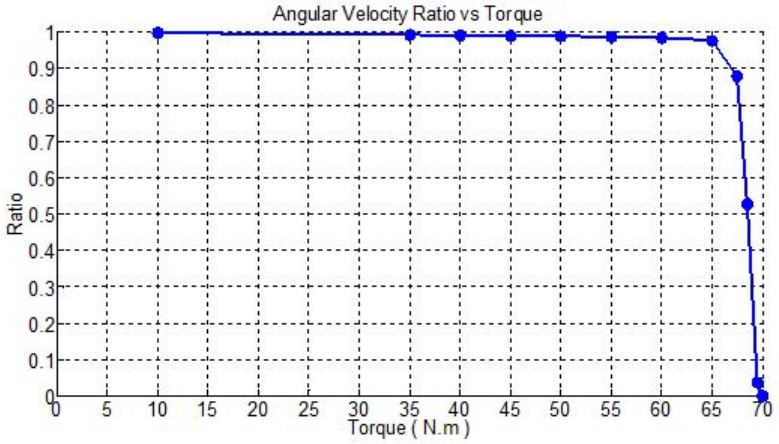

Fig. 6.36. Angular velocity ratio (driven/driver) as a function of the driven pulley opposing torque.

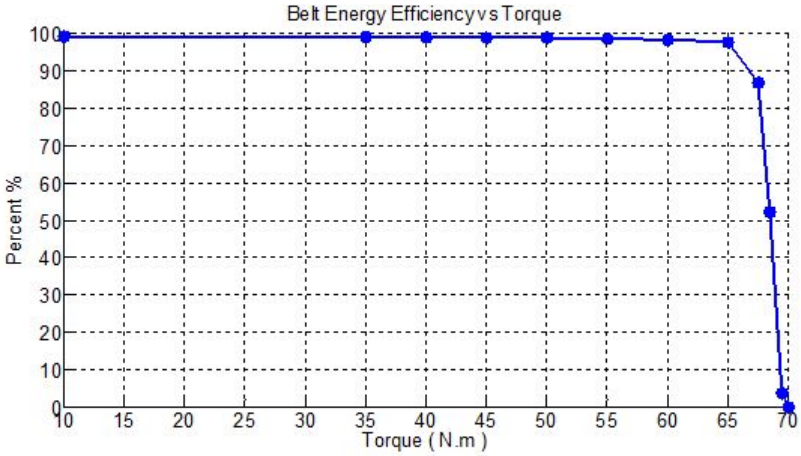

Fig. 6.37. Belt drive energy efficiency as a function of the driven pulley torque.

7. CONCLUSIONS AND FUTURE WORK

7.1 Conclusions

The effect of belt thickness, pulleys' center distance, coefficient of friction, belt axial stiffness, and belt axial damping on the steady-state belt stresses, belt slip, and belt energy efficiency is studied using a three-dimensional transient finite element model. The model uses brick elements for modeling the belt's rubber and truss elements for modeling the belt's cords. An explicit time-integration code is used to solve the equations of motion along with the contact and joint constraint equations. The model includes the effects of Coulomb friction between the belt's rubber and the pulleys, and the shear compliance of the belt. Below conclusions are drawn based on the range that the parameters are varied in. The conclusions are:

- For a thick belt with a compliant rubber matrix, there are two distinct contact zones on the driver pulley: a negative traction zone and a positive traction zone, while only one traction zone is present over the driven pulley. The negative traction zone and the initial part of the positive slip zone approximately corresponds to the stick zone for a zero thickness belt.

- Increasing belt thickness reduces both the low and high tension span tension forces while it is increasing the tension forces on both driver and driven pulleys. Increasing belt thickness increases the cyclic range of the tension forces and negatively affects the fatigue life.

- The size of the negative traction zone on the driver pulley does not depend on the belt thickness.

- Increasing belt thickness increases the torque drop spikes in the driver pulley and causes noise.

- Increasing the belt thickness reduces the energy efficiency of the belt-drive and increases the belt slip.
- Increasing the pulleys' center distance increases the overall belt length and inertia of the belt. This slightly increases the belt's normal stress and belt tension.
- The effects of diameter ratio variation can be explained by 'Torque', 'Angular Velocity', 'Belt Thickness' and 'Pulley Center Distance' variation. Variation of diameters directly changes the torque and the angular velocity. Although changing diameter does not change the belt thickness, it changes the 'relative belt thickness' which can be defined as the ratio of thickness to pulley diameter. Increasing the pulley diameter with constant thickness may replicate the results of reduced belt thickness. Although changing diameter does not change the pulleys' center distance, it changes the overall belt length and belt inertia which results in similar effect.
- Due to strong correlation of torque and belt thickness to diameter ratio, the major effects of diameter variation can be explained via change in torque and 'relative belt thickness'.
- When relative belt thickness becomes small enough, similar stick-slip effects of the 0 mm can also be observed on 3 mm belt thickness belt.
- At a ratio of 1.0, the driven pulley is not able to transfer power of 8400W with 120rad/sec and 70N.m torque and results in gross slip. However, varying the diameter ratio reduces the torque and increases the speed and allows the belt-drive to transfer targeted power with high efficiency. Diameter varying could be used to reduce torque and increase speed to deliver same power, while avoiding high torque which can cause reduced energy efficiency or gross slip.
- The width of the negative traction zone on the driver pulley increases with the belt-pulley coefficient of friction.

- The average normal force and the belt tension over the driver pulley increase with the coefficient of friction, while the average normal force and belt tension over the driven pulley increase with the decrease of the coefficient of friction.
- The belt-drive energy efficiency is unaffected by the coefficient of friction (within the range tested) as long as gross slip is not occurring.
- The width of the negative traction zone on the driver pulley increases as the belt axial stiffness decreases.
- The average normal force and the belt tension over the driver pulley increase with the belt axial stiffness, while the average normal force and belt tension over the driven pulley decrease slightly as the belt axial stiffness increases.
- The belt-drive energy efficiency and driven over driver angular velocity ratio increase with the belt axial stiffness.
- The belt's axial damping has a negligible effect on the steady-state response of the belt-drive.
- As the belt bending stiffness increases larger tangential and normal contact belt stresses develop at the entrance and exit of both driver and driven pulleys.
- Both the maximum and minimum belt tension increase as the belt bending stiffness increases.
- Belt bending stiffness does not affect the belt-drive energy efficiency (as long as belt bending damping is unchanged by the bending stiffness).
- As belt bending damping increases, the initial negative tangential belt stress at the stick zone increases.
- Belt energy efficiency significantly drops as the bending damping increases.

- As the operating angular velocity increases the maximum tangential belt stress decreases and the positive slip zone width increases and the negative slip zone width decreases.

- As the operating angular velocity increases the maximum belt tension decreases but the average belt tension increases due to the increase centrifugal inertia forces. Increased centrifugal forces result in very similar effect of reduced coefficient of friction. The effects of increased angular velocity can be explained by reduced effective coefficient of friction.

- As the operating load increases on the driven pulley, the maximum tangential stress at the stick zone of driver pulley increases as well as the size of the slip zone increases.

- At the low load condition the driven pulley slip zone tangential stress is close to zero and the traction occurs at the pulley entrance rather than the exit. Also, at the low load condition the belt normal stress and tension are nearly constant over the driven pulley.

- Increasing torque load increases the cyclic range of the tension forces and negatively affects the fatigue life.

- Belt energy efficiency linearly decreases as a function of torque load until gross slip starts to occur, at which point the fall in energy efficiency is quick and exponential until the energy efficiency is zero.

The results of this thesis can be used optimize belt-drives by showing how the selected parameters affect the belt-drive response, specifically, the steady-state maximum belt stresses, belt slip, and belt-drive energy efficiency.

7.2 Future Work

Some of the future work that can use the modeling and analysis techniques presented in this thesis include:

- Predicting the steady-state harmonic response of the two pulley belt-drive. The effects of the magnitude and frequency of the angular velocity and the applied torque can be studied.
- Predicting the transient response of the two pulley belt-drive. Transient loads can be a step or pulse excitation to the angular velocity or the torque load.
- Predicting the steady-state response of complex multi-pulley belt-drives involving tensioners, clutches, etc.
- Predicting the steady-state harmonic response of complex multi-pulley belt-drives.
- Predicting the transient response of complex multi-pulley belt-drives.

REFERENCES

REFERENCES

[1] M. L. Euler, "Remarques sur l'effect du frottement dans l'equilibre," *Me'm Acad. Sci. Berlin*, pp. 265–278, 1762.

[2] B. G. Grashof, *Theoretische Maschinenlehre*. Hamburg: Leopold Voss, 1883.

[3] J. N. Fawcett, "Chain and belt drives—a review," *Shock Vib. Dig*, vol. 13, no. 5, pp. 5–12, 1981.

[4] K. L. Johnson, *Contact Mechanics*. Cambridge University Press, 1985, ch. 8.

[5] S. Bechtel, S. Vohra, K. Jacob, and C. Carlson, "The stretching and slipping of belts and fibers on pulleys," *Journal of Applied mechanics*, vol. 67, no. 1, pp. 197–206, 2000.

[6] W. T. Townsend and J. Salisbury, "The efficiency limit of belt and cable drives," *Journal of Mechanical Design*, vol. 110, no. 3, pp. 303–307, 1988.

[7] M. Leamy and T. Wasfy, "Analysis of belt-driven mechanics using a creep-rate-dependent friction law," *ASME Journal of Applied Mechanics*, vol. 69, no. 6, pp. 763–771, 2002.

[8] J. Oden and J. Martins, "Models and computational methods for dynamic friction phenomena," *Computer methods in applied mechanics and engineering*, vol. 52, no. 1, pp. 527–634, 1985.

[9] N. Makris and M. Constantinou, "Analysis of motion resisted by friction. ii. velocity-dependent friction," *Journal of Structural Mechanics*, vol. 19, no. 4, pp. 501–526, 1991.

[10] T. Firbank, "Mechanics of the belt drive," *International Journal of Mechanical Sciences*, vol. 12, no. 12, pp. 1053–1063, 1970.

[11] G. G. Gerbert, "Paper xii (i) on flat belt slip," *Tribology Series*, vol. 18, pp. 333–340, 1991.

[12] G. Gerbert, "Belt slip–a unified approach," *ASME Journal of Mechanical Design*, vol. 118, no. 3, pp. 432–438, 1996.

[13] D. Alciatore and A. Traver, "Multipulley belt drive mechanics: creep theory vs shear theory," *Journal of Mechanical Design*, vol. 117, no. 4, pp. 506–511, 1995.

[14] L. Kong and R. Parker, "Microslip friction in flat belt drives," *Proceedings of the Institution of Mechanical Engineers, Part C: Journal of Mechanical Engineering Science*, vol. 219, no. 10, pp. 1097–1106, 2005.

[15] C. R. Barker, L. R. Oliver, and W. F. Breig, "Dynamic analysis of belt drive tension forces during rapid engine acceleration," SAE Technical Paper, Tech. Rep., 1991.

[16] S.-J. Hwang, N. Perkins, A. Ulsoy, and R. Meckstroth, "Rotational response and slip prediction of serpentine belt drive systems," *ASME Journal of Vibration and Acoustics*, vol. 116, no. 1, pp. 71–78, 1994.

[17] R. Beikmann, N. Perkins, and A. Ulsoy, "Free vibration of serpentine belt drive systems," *ASME Journal of Vibration and Acoustics*, vol. 118, no. 3, pp. 406–413, 1996.

[18] N. Perkins and A. Ulsoy, "Nonlinear coupled vibration response of serpentine belt drive systems," *ASME Journal of Vibration and Acoustics*, vol. 118, pp. 567–574, 1996.

[19] R. Beikmann, N. Perkins, and A. Ulsoy, "Design and analysis of automotive serpentine belt drive systems for steady state performance," *ASME Journal of mechanical design*, vol. 119, no. 2, pp. 162–168, 1997.

[20] M. Leamy, N. Perkins, J. Barber, and R. Meckstroth, "Influence of tensioner friction on accessory drive dynamics," SAE Technical Paper, Tech. Rep., 1997.

[21] M. Leamy and N. Perkins, "Nonlinear periodic response of engine accessory drives with dry friction tensioners," *ASME Journal of Vibration and Acoustics*, vol. 120, no. 4, pp. 909–916, 1998.

[22] T. Kraver, G. Fan, and J. Shah, "Complex modal analysis of a flat belt pulley system with belt damping and coulomb-damped tensioner," *ASME Journal of Mechanical Design*, vol. 118, no. 2, pp. 306–311, 1996.

[23] M. Leamy, J. Barber, and N. Perkins, "Distortion of a harmonic elastic wave reflected from a dry friction support," *ASME Journal of applied mechanics*, vol. 65, no. 4, pp. 851–857, 1998.

[24] M. J. Leamy, J. Barber, and N. Perkins, "Dynamics of belt/pulley frictional contact," in *IUTAM Symposium on Unilateral Multibody Contacts*. Springer, 1999, pp. 277–286.

[25] M. Leamy, "The influence of dry friction in the dynamic response of accessory belt drive systems," Ph.D. dissertation, 1998.

[26] M. Leamy and T. Wasfy, "Dynamic finite element modeling of belt-drives," in *18th Biennial Conference on Mechanical Vibration and Noise, ASME International*, 2001.

[27] M. J. Leamy and T. M. Wasfy, "Transient and steady-state dynamic finite element modeling of belt-drives," *ASME Journal of dynamic systems, measurement, and control*, vol. 124, no. 4, pp. 575–581, 2002.

[28] L. Della Pietra and F. Timpone, "Tension in a flat belt transmission: experimental investigation," *Mechanism and Machine Theory*, vol. 70, pp. 129–156, 2013.

[29] M. J. Leamy and T. M. Wasfy, "Dynamic finite element modeling of belt-drives including one-way clutches," in *ASME 2001 Int Mech Eng Congress and Exposition*, 2001.

[30] R. J. Meckstroth, T. M. Wasfy, and M. J. Leamy, "Finite element study of dynamic response of serpentine belt-drives with isolator clutches," SAE Technical Paper, Tech. Rep., 2004.

[31] T. Wasfy and M. Leamy, "Effect of bending on the dynamic and steady-state responses of belt-drives," in *27th Biennial Mechanisms and Robotics Conference*, 2002.

[32] T. M. Wasfy, "Asperity spring friction model with application to belt-drives," in *ASME 2003 International Design Engineering Technical Conferences and Computers and Information in Engineering Conference*, no. DETC2003-48343. American Society of Mechanical Engineers, 2003, pp. 371–378.

[33] M. J. Leamy, R. J. Meckstroth, and T. M. Wasfy, "Finite element study of belt-drive frictional contact under harmonic excitation," SAE Technical Paper, Tech. Rep., 2004.

[34] M. J. Leamy, R. J. Meckstroth, and T. Wasfy, "Finite element study of belt-drive frictional contact under harmonic excitation," SAE Technical Paper, Tech. Rep., 2004.

[35] M. J. Leamy and T. M. Wasfy, "Time-accurate finite element modelling of the transient, steady-state, and frequency responses of serpentine and timing belt-drives," *International journal of vehicle design*, vol. 39, no. 3, pp. 272–297, 2005.

[36] D. Kim, M. Leamy, and A. Ferri, "Dynamic modeling of flat belt drives using the elastic-perfectly-plastic friction law," in *ASME 2009 International Design Engineering Technical Conferences and Computers and Information in Engineering Conference*. American Society of Mechanical Engineers, 2009, pp. 483–491.

[37] G. Čepon, L. Manin, and M. Boltežar, "Validation of a flexible multibody belt-drive model," *Strojniški vestnik-Journal of Mechanical Engineering*, vol. 57, no. 7-8, pp. 539–546, 2011.

[38] W.-H. Chen and C.-J. Shieh, "On angular speed loss analysis of flat belt transmission system by finite element method," *International Journal of Computational Engineering Science*, vol. 4, no. 01, pp. 1–18, 2003.

[39] T. M. Wasfy, H. M. Wasfy, and J. M. Peters, "Prediction of the normal and tangential friction forces for thick flat belts using an explicit finite element code," in *ASME 2013 International Design Engineering Technical Conferences and Computers and Information in Engineering Conference*, no. DETC2013-13714. American Society of Mechanical Engineers, 2013.

[40] T. Firbank, "On the forces between the belt and driving pulley of a flat belt drive," in *Proceedings of the ASME Design Engineering Technical Conference*, 1977, pp. 1–5.

[41] R. Palmer and J. Jarvis, "Steady state strains in power transmitting flat belts made of composite material," *Strain*, vol. 16, no. 4, pp. 156–161, 1980.

[42] T. Childs, "The contact and friction between flat belts and pulleys," *International Journal of Mechanical Sciences*, vol. 22, no. 2, pp. 117–126, 1980.

[43] H. Kim, K. Marshek, and M. Naji, "Forces between an abrasive belt and pulley," *Mechanism and machine theory*, vol. 22, no. 1, pp. 97–103, 1987.

[44] K. Marshek, "Belt forces and surface model for a cloth-backed and a rubber-backed flat belt," *ASME Journal of Mechanisms, Transmissions and Automation in Design*, vol. 110, pp. 93–99, 1988.

[45] D. P. Smith, "Tribology of the belt-driven data tape cartridge," *Tribology international*, vol. 31, no. 8, pp. 465–477, 1998.

[46] T. Wasfy, "Lumped-parameters brick element for modeling shell flexible multibody systems," in *18th Biennial Conference on Mechanical Vibration and Noise, ASME International 2001 DETC*, 2001.

[47] T. M. Wasfy, "Edge projected planar rectangular element for modeling flexible multibody systems," in *ASME 2003 International Design Engineering Technical Conferences and Computers and Information in Engineering Conference*. American Society of Mechanical Engineers, 2003, pp. 439–447.

[48] T. Wasfy, "A torsional spring-like beam element for the dynamic analysis of flexible multibody systems," *International Journal for Numerical Methods in Engineering*, vol. 39, no. 7, pp. 1079–1096, 1996.

[49] T. M. Wasfy, "Modeling spatial rigid multibody systems using an explicit-time integration finite element solver and a penalty formulation," in *ASME 2004 International Design Engineering Technical Conferences and Computers and Information in Engineering Conference*. American Society of Mechanical Engineers, 2004, pp. 901–908.

[50] T. M. Wasfy, H. M. Wasfy, and J. M. Peters, "Real-time explicit flexible multibody dynamics solver with application to virtual-reality based e-learning," in *ASME 2011 International Design Engineering Technical Conferences and Computers and Information in Engineering Conference*. American Society of Mechanical Engineers, 2011, pp. 675–687.

[51] T. M. Wasfy and J. O'Kins, "Finite element modeling of the dynamic response of tracked vehicles," in *ASME 2009 International Design Engineering Technical Conferences and Computers and Information in Engineering Conference*. American Society of Mechanical Engineers, 2009, pp. 1999–2009.

[52] A. Science and A. Corp., "Dis (dynamic interactions simulator)," (Last accessed April 2015). [Online]. Available: http://www.ascience.com/ScProducts.htm

[53] O. A. Elmaraghi, "Integrated multibody dynamics and fatigue models for predicting the fatigue life of poly–v ribbed belts," Master's thesis, Purdue University Indianapolis, 2013.